Ab initio study of work function modification at organic/metal interfaces

Dissertation zur Erlangung des akademischen Grades
Doctor rerum naturalium (Dr. rer. nat.)

im Fach: Physik
Spezialisierung: Theoretische Physik

eingereicht an der

Mathematisch-Naturwissenschaftlichen Fakultät
der Humboldt-Universität zu Berlin

von

M. Sc. Jongmin Kim

Präsidentin der Humboldt-Universität zu Berlin
Prof. Dr. Julia von Blumenthal

Dekanin der Mathematisch-Naturwissenschaftlichen Fakultät
Prof. Dr. Caren Tischendorf

Gutachter/innen:

1. Prof. Dr. Dr. h.c. Claudia Draxl
2. Prof. Dipl.-Ing. Dr. Peter Puschnig
3. Dr. Denis Usvyat

Tag der mündlichen Prüfung: 19.04.2024

Ich erkläre, dass ich die Dissertation selbständig und nur unter Verwendung der von mir gemäß § 7 Abs. 3 der Promotionsordnung der Mathematisch-Naturwissenschaftlichen Fakultät, veröffentlicht im Amtlichen Mitteilungsblatt der Humboldt-Universität zu Berlin Nr. 42/2018 am 11.07.2018 angegebenen Hilfsmittel angefertigt habe.

Berlin, 24.10.2023

Abstract

Charge injection (extraction) at an interface plays a crucial role to organic electronics because this injection (extraction) heavily affects the device performance. One of the most efficient way to optimize energy barriers of the injection (extraction) is modifying the work function of electrodes. In this dissertation, we investigate the modification of work function of Au(111) and Ag(111) induced by the dithiol-terminated polyethylene glycol (PEG(thiol)) as well as a dependence of the work function change on different numbers of PEG repeat units.

We find that the work function of the Au(111) is reduced by a monolayer of PEG(thiol) molecules. Overall, our calculations indicate that the work function change is mainly induced by (i) the charge rearrangement due to chemisorption and (ii) the intrinsic dipole moment of the PEG(thiol) monolayer. The magnitude of the latter contribution noticeably depends on the number of repeat units and, thus, causes a variation in the reduction of the work function. The oscillatory behavior reflects a pronounced odd-even effect. As a result, the work function of the metal electrode would be controlled by considering the odd-even effect.

Unfortunately, the convergence of the self-consistent field iteration is not guaranteed for our investigated systems. To make the smooth convergence, a mixing algorithm, which is applicable to FP-LAPW method, is devised. We add the Kerker preconditioner as well as further improvements to Pulay's direct inversion in the iterative subspace. Using this method, one can avoid charge sloshing and noise in the exchange-correlation potential. This method is also implemented in the **exciting** code. We observe that the implementation works reliably, and is robust.

In a system used the Ag(111) surface, a structure including two vacancies in the substrate layer is the most stable. We find the decrease of the work function of the Ag(111) surface is always presented. Similar to the Au(111) case, the odd-even effect is revealed, arising from the dipole moment of the molecular layer. On the contrary, contributions to the work function modification between both metal surfaces are significantly different due to a reconstruction of the Ag surface as well as a different adsorption geometry.

Zusammenfassung

Die Ladungsinjektion (-extraktion) an einer Schnittstelle spielt in der organischen Elektronik eine entscheidende Rolle, da sie die Leistung des Bauelements stark beeinflusst. Eine der effizientesten Methoden zur Optimierung der Energiebarrieren für die Injektion ist die Modifikation der Austrittsarbeit der Elektroden. In dieser Dissertation untersuchen wir die Modifikation der Austrittsarbeit von Au(111) durch dithiol-terminiertes Polyethylenglykol (PEG(thiol)) sowie deren Abhängigkeit von der Anzahl der PEG-Wiederholungseinheiten.

In beiden Fällen beobachten wir, dass die Austrittsarbeit des Au(111) durch eine Monoschicht PEG(thiol)-Moleküle reduziert wird. Unsere Berechnungen zeigen, dass diese Änderung der Austrittsarbeit hauptsächlich durch (i) die Ladungsumlagerung aufgrund der Chemisorption und (ii) das intrinsische Dipolmoment der PEG(thiol)-Monoschicht verursacht wird. Die Größe des letzteren Beitrags hängt spürbar von der Anzahl der Wiederholungseinheiten ab und bewirkt somit eine Variation in der Reduktion der Austrittsarbeit. Das oszillatorische Verhalten spiegelt einen ausgeprägten Odd-Even-Effekt wider. Dadurch kann die Austrittsarbeit der Metallelektrode unter Berücksichtigung des Odd-Even-Effekts gesteuert werden.

Die Konvergenz der selbstkonsistenten Felditeration für unsere Systeme ist nicht garantiert. Um die Konvergenz zu verbessern, schlagen wir die Verwendung eines speziell auf die FP-LAPW-Methode zugeschnittenen Mischalgorithmus vor. Diese Implementierung hat sich als zuverlässig und robust erwiesen.

In einem auf Ag(111) basierenden System zeigt sich, dass eine Struktur mit drei Leerstellen in der Substratschicht besonders stabil ist. Dabei ist eine kontinuierliche Abnahme der Austrittsarbeit des Ag(111) feststellbar. Ähnlich wie beim Au(111) manifestiert sich der Odd-Even-Effekt, der auf das Dipolmoment der Molekularschicht zurückzuführen ist. Im Gegensatz dazu zeigen die Beiträge zur Veränderung der Arbeitsfunktion zwischen den beiden Metalloberflächen aufgrund einer Rekonstruktion der Ag-Oberfläche und unterschiedlicher Adsorptionsgeometrie signifikante Unterschiede.

Dissertation

Ab initio study of work function modification at organic/metal interfaces

Jongmin Kim

under supervision of
Univ. Prof. Dr. Dr. h.c. Claudia Draxl

이 학위논문을 나의 가족에게 바칩니다.

Contents

1. Introduction

The interface between an organic material and an electrode plays a crucial role in the properties of organic devices such as organic light-emitting diodes (OLEDs), organic photovoltaics (OPVs), and organic field-effect transistors (OFETs) [1, 2]. Sometimes, such devices suffer from poor charge-injection (extraction) which leads to limited performance [3–6]. In order to improve device performance noticeably, the corresponding energy barrier should be optimized. To do it, various treatments have been proposed: typical ways [7] are to dope the organic semiconductor, or to tune the substrate work function [8].

For the latter approach, the highest occupied molecular orbital (HOMO) of the organic semiconductor is required to match with the work function of the anode. Similarly, the difference between the lowest unoccupied molecular orbital (LUMO) energy level and the cathode needs to be small. For this purpose, it is desirable to use high- and low-work function materials for anode and cathode, respectively [9]. For instance, one widely uses low work-function metals like Ca, Mg, and Al as the cathode [10–12]. Unfortunately, these metals cause an unstable performance of devices due to intense chemical reactions or oxidation by oxygen or water [12, 13]. Other metals like Ag and Au are chemically stable, but one cannot use them directly as the cathode due to the large energy barriers for charge-injection (extraction) induced by their high work function. One can overcome this shortcoming by tuning the electrode work function via an interlayer at the organic/electrode interface [14–17]. Polymers, metal oxides, inorganic salts, and self-assembled monolayers (SAMs) are commonly used as the interlayers that lead to modification of the electrode's work function by inducing a dipole at the interface [3, 5, 12, 18–20].

Recently, experimental works have provided a promising way to improve the performance of OPVs, OLEDs, and OFETs using polyethylene glycol (PEG) employed as the interlayer [21–26]. According to experimental studies [21–24, 26, 27], a self-generated interlayer is formed by the interaction between PEG-based additives and electrodes. The additives are blended with the organic semiconductor, and they can migrate to the interface. This self-generating approach is useful to fabri-

cate devices. However, since the spontaneously generated interlayer is created at a buried organic/metal interface, measuring precisely the energy level alignment or its structure is an experimentally difficult task [27]. A SAM made by PEG molecules can be an alternative interlayer. One can directly capture electronic and structural properties at the interface between such a SAM and an electrode. Indeed, SAMs are able to chemically control the physical properties of the interface. A number of studies have showed that SAMs consisting of alkanethiols and phenylthiols can adjust the properties of the electrodes [9, 20, 28–33]. In this context, the questions arise if the SAM formed by PEG affects the properties of the electrode, and how mechanism of the interface modification by this SAM works. In this dissertation, we model dithiol-terminated PEG (PEG(thiol)) adsorbed on an electrode surface, such as Au(111) and Ag(111), by performing first-principles calculations using all-electron full-potential code **exciting** [34]. We investigate the impact of the PEG molecule as well as its length on the modulation of the electrode's work function.

In the investigated systems, a self-consistent solution is often hard to achieve within the DFT simulations because the charge density in the systems strongly fluctuates during a self-consistent field (SCF) iteration due to numerical problems, such as charge-sloshing [35–42] and noisy potentials in the low-density region [43, 44]. These density oscillations lead to a slow convergence or even a divergence. To suppress the charge-sloshing instability that stems mainly from the Hartree potential, one uses a Kerker preconditioner [37] in the mixing schemes, e.g., the Pulay method [45, 46]. This preconditioner leads to a stable SCF cycle. Unfortunately, the mixing methods that utilize the preconditioner are mainly developed for planewave/pseudopotential methods. Thus, preconditioners for all-electron methods are still needed. To tackle the numerical problems, we propose a mixing algorithm for full-potential (FP) all-electron calculations in the linearized augmented planewave (LAPW) method. We reformulate the Kerker preconditioner in a such way that it is applicable in FP-LAPW calculations. Furthermore, we implement the modified Pulay mixing with this preconditioner in the **exciting** code and investigate its performance.

Molecular crystals and organic/inorganic systems are often van der Waals (vdW) bound [48]. For example, the interactions between the adsorbed molecule and the substrate are mostly governed by the vdW force in the physisorption case. In case of chemisorption, especially SAMs adsorbed on a substrate system, the vdW force can play a crucial role for the interface geometry by affecting the molecular tilting angle as well as the molecular distortion [49, 50]. Thus, one cannot neglect vdW interactions for obtaining reliable structural features and energies [47, 51, 52]. How-

ever, semi-local density-functional theory cannot describe correctly the long-range electron correlations [53]. Methods therefore are required to reliably capture the vdW interactions within the DFT framework. For this purpose, various methods have been proposed [54–63]. A common approach for computing the long-range dispersion energy is DFT-D2 proposed by Grimme [54, 55]. It corrects the total energy obtained in a DFT calculation by adding a semi-empirical correction term consisting of a sum over pairwise atomic interactions. The DFT-D2 method sometimes fails due to the fact that it neglects the effects of different chemical or geometrical environments surrounding each individual atom. In addition, the method is a semi-empirical correction and neglects many-body effects. To overcome this problem, Ambrosetti *et al*. devised a method beyond the pairwise interactions for a microscopic description of the frequency-dependent polarizability which is termed many-body dispersion (MBD@rsSCS). [59, 61]. This method includes both a non-additive many-body vdW energy and long-range screening contributions. We implement this scheme in the **exciting** code. Afterwards, we employ the MBD@rsSCS and the semi-empirical method DFT-D2 [55] to our investigated systems.

The outline of this dissertation is given as follows: Chapter 2 starts with a general description of organic electronics devices, particularly organic light-emitting diodes (OLEDs). The discussion of the charge injection OLEDs is also presented. Subsequently, theoretical aspects of the interface energetics at metal/organic interfaces for physisorption and chemisorption cases are presented.

Chapter 3 provides a theoretical background of density-functional theory. At first, we present the many-body problem. Afterwards, a concept of the density-functional theory is discussed including the Kohn-Sham equation and approximations. We discuss mixing methods for quickly converging SCF calculations. In this chapter, three common mixing approaches are described: linear mixing, Pulay mixing, and multisecant Broyden mixing. Further, we introduce three methods for including the vdW interactions in the DFT framework: DFT-D2, Tkatchenko-Scheffler (TS) [57], and MBD@rsSCS methods.

In Chapter 4, we introduce the full-potential linearized augmented planewave (FP-LAPW) method in detail. First, this chapter explains APW and LAPW basis sets, and introduces the concept of local orbitals. We then provide the treatment of the potential and the charge density in the FP-LAPW, followed by the evaluation of the Hartree potential that can be calculated using the pseudo-charge method. This method can be also exploited for a new mixing method discussed in Chapter 5.

In Chapter 5, we explain how the proposed mixing algorithms and the MBD@rsSCS method are adapted to the FP-LAPW and implemented in the **exciting** code. We

further give a mathematical perspective used for aforementioned implementations, and show their performance of with benchmark studies. Firstly, the newly implemented mixing approach and existing methods are tested for the 2×2 Au(111) surface with a vacancy, and for the Pd(111) surface with 15 atomic layers. Next, we apply various vdW corrections including the implemented MBD@rsSCS on layered materials, particularly, graphite and hexagonal boron nitride. We also compare our results with experimental values as well as benchmarks from other papers.

In Chapter 6, the structural and electronic properties of a layer of PEG(thiol) molecules adsorbed on Au(111) and Ag(111) are discussed. First, we briefly describe polyethylene glycol derivatives. An investigation of the work-function change depending on different numbers of PEG repeat units is given. We analyse the nature of the work-function change in terms of its contributions: bond dipole, molecular dipole, and surface-relaxation contributions. For PEG(thiol) on Au(111), we show how the adsorption structure and work-function modification vary depending on the choice of the vdW correction. Two different coverage patterns are further compared to analyze these properties.

Part I

Background

2. Metal/organic interfaces

2.1 Organic electronics: OLEDs

Organic electronics have attracted considerable research interest due to its great potential for applications, such as organic light emitting diodes (OLEDs), organic photovoltaics (OPVs), and organic field effect transistors (OFETs). OLEDs are the most representative organic electronics device. We therefore focus in this section on OLEDs as an example.

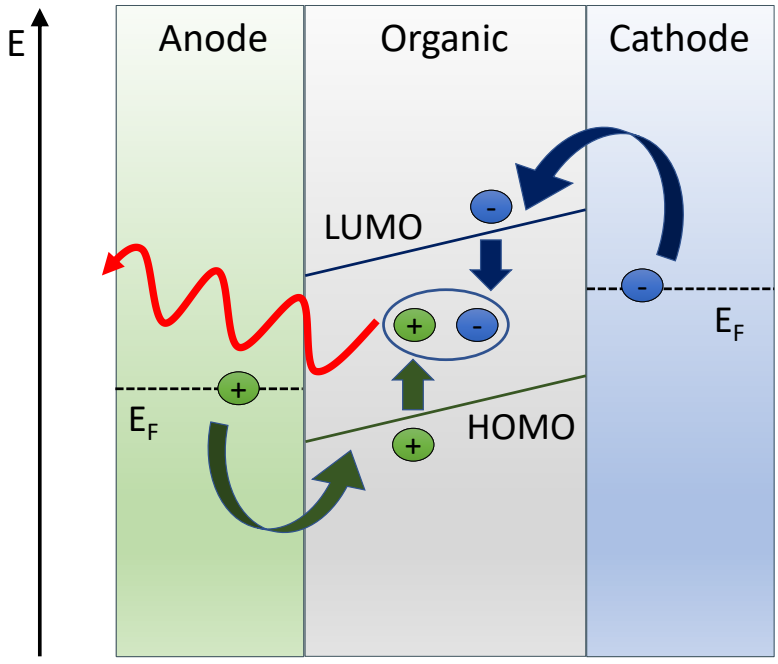

Figure **2-1**: Illustration of an OLED.

Figure **2-1** shows a schematic illustration of an OLED structure. OLEDs comprise electrodes and organic semiconducting layers between the electrodes. In this device, electrons from the cathode are injected into the organic material. Similarly, hole injection is provided from the anode, where a transparent electrode such as transparent conducting oxides (TCOs) is commonly used [64]. The injected elec-

trons and holes create electron-hole pairs, followed by generating a photon after the recombination process. The photon is emitted through the transparent electrode, and its energy depends on the difference between the highest occupied molecular orbital (HOMO) and the lowest unoccupied molecular orbital (LUMO) of the organic material. These energy levels can be controlled by doping of the organic material or using a multilayer device structure [65–67].

OLEDs consisting of only one organic layer commonly lead to an inefficient performance due to an unbalanced charge transport [68, 69], namely, holes in an organic material typically exhibit a higher mobility than electrons. Therefore, the holes can be either moved easily toward the opposite electrode without forming electron-hole pairs, or such pairs are formed near the electrode, causing a carrier quenching effect. To address this drawback, a multilayered heterojunction structure including electron- and hole-injection (transport) layers has been considered for OLEDs [70,71]. Those layers prevent the charge from directly reaching the opposite electrode.

As mentioned in the introduction, energy levels of the organic material, i.e., HOMO and LUMO, should be matched with the work function of adjacent electrode to enhance the device performance. For this purpose, the anode requires high work function material. Indeed, indium tin oxide (ITO) is widely used as the anode due to high conductivity and transparency properties [72]. Surface treatment with UV-ozone and oxygen plasma increase the corresponding work function by the modification of the interfacial composition [72,73]. For the cathode, low work function materials are desired. Li, Ca, Mg, and Al have a low work function, but they are chemically very reactive and easily oxidized [12, 13], leading to limited device performance. An alternative is to introduce a layer between the cathode and the organic semiconductor, e.g., LiF, NaF, and MgF_2 [74–77], to enhance the stability of the OLEDs by modifying the electrode's work function.

2.1.1 Charge-injection

A charge-injection barrier Δ_b is defined as the energy difference between the Fermi level of the electrodes and the energy level of the organic material such as HOMO. A large charge-injection barrier at the interface results in poor efficiency of the device. The charges can overcome the barrier through thermally assisted tunneling or electric-field induced tunneling [78]. The injection current density J at the interface is given without applied field [78, 79] by

$$J \approx N\mu \exp\left[-\frac{q\Delta_b}{k_B T}\right], \tag{2-1}$$

and with a field [78, 79] by

$$J \approx N\mu \exp\left[-\frac{q\Delta_b}{k_B T}\right]\left\{\exp\left[\frac{qV}{k_B T}\right] - 1\right\}. \tag{2-2}$$

Here, q, μ, N, and T are the charges, their mobility, density of states, and the temperature, respectively. k_B is the Boltzmann constant. V indicates the applied voltage. Eqs. 2-1 and 2-2 demonstrate that a small injection-barrier leads to a large injection current because J depends on Δ_b. The charge injection at the interface can be optimized by increasing the temperature or the electric field. A high energy consumption, however, is required to produce high temperature or a strong electric field. Thus, this approach is difficult to apply to the device. Other approaches to improve the injection are to control the charge-transport properties μ, N, and Δ_b. Unfortunately, the possibilities to tune μ and N are limited because they depend on the material. Minimizing Δ_b, therefore, is the simplest and most efficient way to improve the charge injection.

2.2 Interface energetics

We can estimate the charge-injection barrier by the difference between the electrode work function and the energy levels of the organic semiconductor as described in Sec. 2.1.1. The barrier can be modified by changing the interface properties, e.g., a metal work-function shift, caused by interface dipole formation [3, 5, 12, 19, 80].

In Fig. **2-2**, the energy levels of a simple metal/organic interface are displayed. Here, we assume vacuum level alignment for the interface energetics. E_{vac} is the energy of the vacuum level. One defines the work function of the metal as the energy difference between E_{vac} and the Fermi level E_f, i.e., $\Phi = E_{vac} - E_f$. The energy difference between the HOMO and E_{vac} defines the ionization potential (IP), whereas the difference between the LUMO and E_{vac} corresponds to the electron affinity (EA). Experimentally, one can measure Φ and IP using ultraviolet photoemission spectroscopy (UPS) [81]. When E_f is located between the HOMO and LUMO of an organic semiconductor, the electron- and hole-injection barriers (Δ_e and Δ_h) can be expressed as

$$\Delta_e = \Phi - EA, \tag{2-3}$$

and

$$\Delta_h = IP - \Phi, \tag{2-4}$$

respectively. In the case of the interface without an interface dipole, the energy of the vacuum level is not shifted. This indicates that the modification of the work function

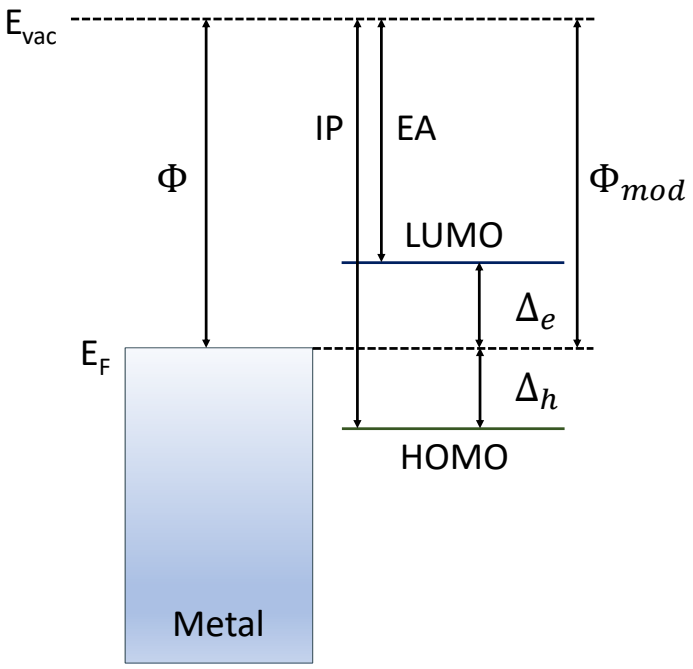

Figure **2-2**: Schematic energy levels of a metal/organic semiconductor interface, representing the work function Φ, the vacuum level E_{vac}, Fermi level E_F, the ionization potential IP, and the electron affinity EA. Δ_e and Δ_h are electron- and hole-injection barriers.

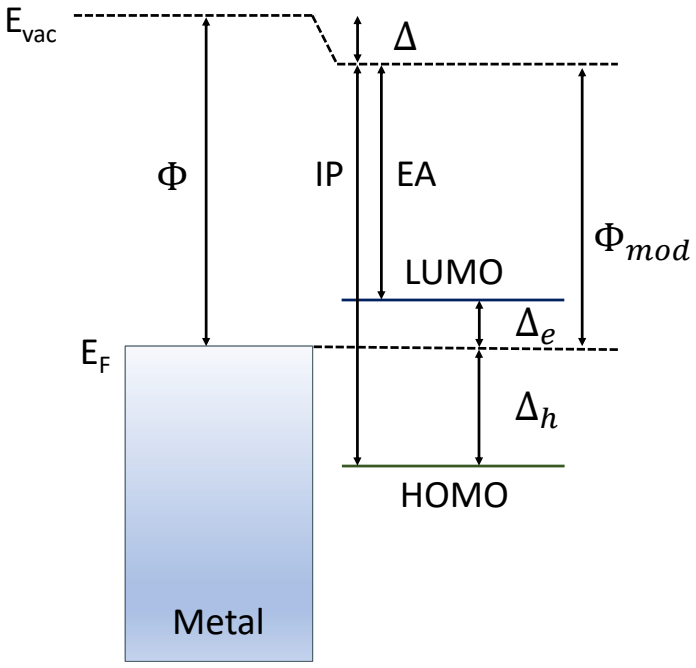

Figure **2-3**: Schematic energy levels of a metal/organic semiconductor interface with an interface dipole.

Φ_{mod} is equivalent to Φ. In fact, vacuum-level alignment in metal/organic interfaces is not realistic because interface dipoles may be formed by charge rearrangement or charge transfer or chemical reaction in actual devices [2, 82]. Due to the interface dipole Δ, the vacuum level and the energy levels of the organic material are shifted. When a dipole is formed at a metal/organic interface, as shown in Fig. **2-3**, Δ_e and Δ_h become

$$\Delta_e = \Phi - EA - \Delta, \tag{2-5}$$

$$\Delta_h = IP - \Phi + \Delta. \tag{2-6}$$

In this case, the magnitude of Δ corresponds to that of the work function change $\Delta\Phi = \Phi - \Phi_{mod}$. This reflects that the interface dipole modifies the work function of the metal surface. One can obtain the minimized Δ_e (Δ_h) by reducing (raising) the work function of the metal surface. In other words, the modulation of the metal work function due to the interface dipole may result in a small charge-injection barrier.

An interface dipole can be induced by several factors, including charge transfer, chemical interaction, and a permanent dipole [2]. Charge transfer between the metal surface and organic molecules leads to the formation of positive and negative charges at the interface. Sometimes, a new chemical bond between the organic and the metal is formed, and the bond causes a charge redistribution. Due to such a charge redistribution, a dipole is induced.

2.2.1 Weakly interacting interfaces

Physisorbed organic molecules interact with a metal surface by weak van der Waals forces, as they do not form covalent bonds with the surface. The charge density of a metal surface before physisorption is schematically shown in Fig. **2-4** (a). The charge density of the nuclei (p(z)) drops abruptly to zero at the metal surface, behaving like a step function. On the other hand, the charge density of the electrons (n(z)) leaks out from the metal surface into the vacuum region [83]. This leakage results in a lack of charge density inside the metal.

This charge inhomogeneity leads to a dipole at the surface, termed surface dipole. As shown in Fig. **2-4** (b), the surface dipole can be defined as the difference in electrostatic potential upon going from the bulk across the metal surface: $\Delta\phi = \phi_{out} - \phi_{in}$. The bulk chemical potential μ_{bulk} is expressed as the difference of E_f and ϕ_{in} [84]. Accordingly, one can calculate the work function Φ of the metal surface as

$$\Phi = \Delta\phi - \mu_{bulk}. \tag{2-7}$$

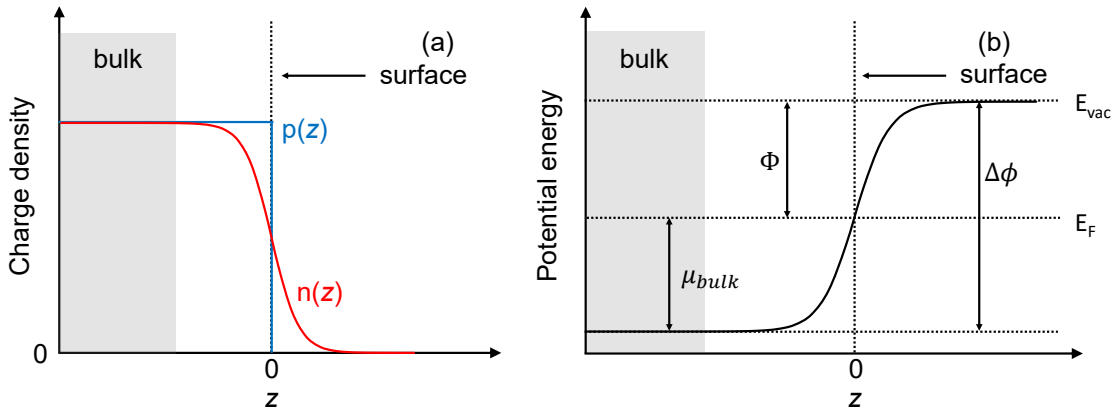

Figure **2-4**: A schematic illustration of (a) charge density of the nuclei (blue) and electrons (red) and (b) electrostatic potential of a metal surface as a function of the distance from the surface z. This figure is adapted based on an illustration in Ref. [14].

μ_{bulk} does not change as a consequence of physisorption. A physisorbed organic molecule induces a change in $\Delta\phi$ and Φ due to the charge rearrangement of the electrons. This behavior is known as *push-back effect* or *cushion effect* [85, 86]. According to the push-back effect, the charge density of the electrons is pushed back into the metal surface due to physisorption. The effect originates from Pauli repulsion that occurs when the wave functions of adsorbed molecules and a metal overlap [87]. To avoid this overlap, the electrons of the metal between the molecules and the surface are pushed into the surface. Consequently, the surface dipole is lowered, and this causes a decreased work function.

The adsorption-induced potential shift can be obtained by a model using a continuous density of states (DOS) of an organic material [88]. To describe this DOS, Oehzelt *et al.* approximated it by a Gaussian peak. For instance, the energy distributions of the HOMO and LUMO are specified with peaks centered at E_H and E_L, and their standard deviations σ_H and σ_L. One can quantify the transferred charge by integrating the charge density ρ. Following Ref. [88], the charge density can be written as

$$\begin{aligned}\rho(z) =& e \cdot n \cdot \Bigg\{ \int dE \cdot f_H(E) \cdot D_H(E)[E + eV(z)] \\ &- \int dE \cdot f_L(E) \cdot D_L(E)[E + eV(z)] \Bigg\},\end{aligned} \tag{2-8}$$

where n is the number of molecules per unit area. f is the Fermi distribution

function defined as follows

$$f_H(E) = \frac{1}{\frac{1}{g_H} e^{-\frac{E-E_F}{k_B T}} + 1}, \qquad f_L(E) = \frac{1}{\frac{1}{g_L} e^{\frac{E-E_F}{k_B T}} + 1}. \tag{2-9}$$

D is the energy distribution based on a Gaussian shape. L and H indicate the LUMO and HOMO, respectively. The electrostatic potential V can be computed by solving the Poisson equation as follows:

$$\nabla[\varepsilon(z)\nabla V(z)] = -\frac{\rho(z)}{\varepsilon_0}, \tag{2-10}$$

where ε and ε_0 denote the permittivity of the organic materials and the vacuum, respectively.

2.2.2 Strongly interacting interfaces

In chemisorbed systems, an organic molecule strongly interacts with the metal surface by forming chemical bonds at the interface. The electronic structure of this strongly interacting case is different to that of the case described in Sec. 2.2.1. In general, a dipole at the interface is induced by the charge rearrangement due to the chemical bond, resulting in an up or down shift of the vacuum level [2, 14, 89].

Due to the charge rearrangement, a partial charge is transferred between metal surface and adsorbed molecules. Note that the charge transfer occurs from the material with higher chemical potential to the one with lower chemical potential. The chemical potentials of the metal and the organic molecule are given as [14, 89]:

$$\mu_{metal} = -\Phi, \tag{2-11}$$

$$\mu_{mol} = -\frac{IP + EA}{2}. \tag{2-12}$$

One is able to compute Eqs. 2-11 and 2-12 using values of Φ, IP, and EA obtained from a DFT calculation. To estimate the magnitude of the dipole, one considers the amount of charge transfer, ΔN: [14]

$$\Delta N = \frac{1}{2}\frac{\mu_{metal} - \mu_{mol}}{\eta_{metal} + \eta_{mol}}, \tag{2-13}$$

with η being the absolute hardness which can be calculated by differentiating the chemical potential with respect to N [90]:

$$\eta = \frac{1}{2}\frac{\partial \mu}{\partial N}. \tag{2-14}$$

η in Eqs. 2-13 and 2-14 varies depending on the material. ΔN causes a vacuum level shift, which in turn results in a change in the work function. Unfortunately,

this model does not include the contribution of the intrinsic dipole of the adsorbed organic molecule. The potential change caused by the intrinsic molecular dipole can be obtained through the Helmholtz equation in the following manner [28, 91]:

$$\Delta V_{mol} = \frac{e\mu_{\perp}}{\varepsilon_0 A}, \tag{2-15}$$

Here, $\mu_{\perp}$ is the dipole of the molecular layer relative to the surface normal. ε_0, A, and e represent the vacuum permittivity, a unit area, and the charge, respectively. ΔV_{mol} is proportional to $\mu_{\perp}$, and ΔV_{mol} is one of the contributions for the modification of the work function.

Another contribution leading to a change in the work function is the dipole due to the chemisorption-induced charge rearrangement as discussed above. This dipole is referred as *bond dipole* (BD) [9, 28, 91, 92]. The charge rearrangement stems from the push-back effect as explained in Sec. 2.2.1 and the formation of the chemical bond at the interface, and this rearrangement can be calculated using DFT as

$$\Delta\rho = \rho_{tot} - (\rho_{mol} + \rho_{metal}), \tag{2-16}$$

where ρ_{tot}, ρ_{mol}, and ρ_{metal} are charge densities of the total combined system, the molecular layer, and the metal surface, respectively. One can compute the bond dipole contribution ΔV_{BD} by employing Eq. 2-10.

The last contribution to the work function modification is the work function change of the isolated metal surface due to the surface relaxation caused by chemisorption $\Delta V_{relax-metal}$. The relaxed surface causes a change in the charge distribution, thus, modifying the work function. As a result, the modification of the work function $\Delta\Phi$ due to chemisorption of the organic molecules can be described as the sum of these contributions [92–94]:

$$\Delta\Phi = \Delta V_{BD} + \Delta V_{mol} + \Delta V_{relax-metal}. \tag{2-17}$$

3. Density-functional theory

In this chapter, we first introduce the many-body problem to describe a system that has interactions of atomic nuclei and electrons. However, due to the complexity of this many-body problem, it is difficult to obtain a solution numerically. To address this issue, we turn to density-functional theory (DFT), which recasts the problem in terms of the electron density instead of the wave function. The concept of using density functionals for a many-body system was proposed by Thomas and Fermi [95,96]. In 1964, Hohenberg and Kohn [97] established a mathematical foundation required for the DFT. A year later, Kohn and Sham [98] provided a practical procedure to make the DFT broadly applicable. Nowadays, the DFT has become the most widely used approach for calculating electronic structure in materials science.

3.1 Many-body problem

The stationary electronic ground state of a system with interacting electrons and nuclei is described by the time-independent Schrödinger equation:

$$\mathcal{H}\Psi(\mathbf{R},\mathbf{r}) = \mathcal{E}\Psi(\mathbf{R},\mathbf{r}), \tag{3-1}$$

where Ψ is the wave function of this system, and $\mathcal{E}$ is the energy. Here, $\mathbf{R} = \{\mathbf{R}_I, I = 1,\ldots,N_{nuc}\}$, and $\mathbf{r} = \{\mathbf{r}_i, i = 1,\ldots,N_{el}\}$ are the positions of atomic nuclei and electrons, respectively. The many-body Hamiltonian of the system, $\mathcal{H}$, contains the kinetic energy operator as well as the Coulomb interaction. It is given by

$$\mathcal{H} = -\sum_i \frac{\nabla_i^2}{2} - \sum_I \frac{\nabla_I^2}{2M_I} + \frac{1}{2}\sum_{i\neq j}\frac{1}{|\mathbf{r}_i-\mathbf{r}_j|} - \sum_{i,I}\frac{Z_I}{|\mathbf{r}_i-\mathbf{R}_I|} + \frac{1}{2}\sum_{I\neq J}\frac{Z_I Z_J}{|\mathbf{R}_I-\mathbf{R}_J|}, \tag{3-2}$$

where M_I is the nucleus mass and Z_I is the charge of the nucleus I. The first and second terms of Eq. 3-2 denote the kinetic energy operator for the electrons and nuclei, respectively. The third and fourth terms, in turn, describe the Coulomb interaction between electrons, and between electrons and nuclei, respectively. The last term describes the Coulomb repulsion between nuclei. The nuclei are much heavier and move much slower than the electrons. Thus, the electrons follow adiabatically

the motion of the nuclei, that is, they move in the potential created by fixed nuclei. The decoupling of those two motions is known as the *Born-Oppenheimer approximation* [99]. Following the approximation, we can split the full problem into two parts: the electronic and nuclei ones. In particular, one is able to decouple their degrees of freedom by factorizing the total wave function: $\Psi(\mathbf{r},\mathbf{R}) = \Psi_e(\mathbf{r};\mathbf{R})\Psi_N(\mathbf{R})$. Here, the electronic wave function $\Psi_e(\mathbf{r};\mathbf{R})$ depends on electronic coordinates as well as parametrically on nuclear coordinates. In the same manner, the Hamiltonian in Eq 3-2 can be separated: $\mathcal{H} = \mathcal{H}_e + \mathcal{H}_N$. The solution of the electron problem has a dependence on nuclear coordinates. For any given nuclear configuration, the Coulomb repulsion between the nuclei becomes a constant in $\mathcal{H}_e$ and has no effect on $\Psi_e(\mathbf{r};\mathbf{R})$. Despite the simplification introduced by the Born-Oppenheimer approximation, further approximations are required to solve the electronic problem.

3.2 Kohn-Sham theory

Following the Hohenberg-Kohn theorems [97], the exact ground state energy is determined in terms of a functional of the ground state density:

$$E[\rho] = F_{HK}[\rho] + \int \rho(\mathbf{r})V(\mathbf{r})d\mathbf{r}, \tag{3-3}$$

where $F_{HK}[\rho]$ is a universal functional, which consists of the kinetic energy and the energy of the electron-electron interaction. $V(\mathbf{r})$ is the external potential due to nuclei which uniquely determines the ground state density. According to the Hohenberg-Kohn theorems, all electronic properties of a system can be obtained from the ground state density, but the theorems did not provide any way to determine the ground state density. Kohn and Sham proposed a practical method to address this issue [98]. The method presents an auxiliary system of non-interacting electrons wherein the electron density is equivalent to that of a real system of interacting electrons. The energy functional for fictitious non-interacting particles can be rewritten as

$$E[\rho] = T_s[\rho] + \int \rho(\mathbf{r})V(\mathbf{r})d\mathbf{r} + J[\rho] + E_{xc}[\rho]. \tag{3-4}$$

Here, T_s denotes the kinetic energy of the non-interacting electron system, and it is given as

$$T_s[\rho] = -\frac{1}{2}\sum_i^N \left\langle \psi_i \left| \nabla^2 \right| \psi_i \right\rangle. \tag{3-5}$$

J is the Hartree energy:

$$J[\rho] = \frac{1}{2}\int \frac{\rho(\mathbf{r})\rho(\mathbf{r}')}{|\mathbf{r}-\mathbf{r}'|} d\mathbf{r}d\mathbf{r}', \tag{3-6}$$

and E_{xc} is the exchange–correlation energy that can be obtained by the energy differences between the interacting and non-interacting cases:

$$E_{xc} = T - T_s + U - J. \tag{3-7}$$

The electron density of N_{el} non-interacting electrons is defined as

$$\rho(\mathbf{r}) = \sum_{i=1}^{N_{el}} |\psi_i(\mathbf{r})|^2 , \tag{3-8}$$

where ψ_i is a single-particle wave function, which is a solution of the Kohn-Sham Hamiltonian. Following the Hohenberg-Kohn theorems [97], the energy functional should be minimized as follows:

$$-\frac{1}{2}\nabla^2\psi_i(\mathbf{r}) + \left\{\hat{v}(\mathbf{r}) + \frac{\delta J[\rho]}{\delta\rho} + \frac{\delta E_{xc}[\rho]}{\delta\rho} - \epsilon_i\right\}\psi_i(\mathbf{r}) = 0, \tag{3-9}$$

where ϵ_i is the Lagrange multiplier. We define the effective Kohn-Sham potential $\hat{v}_{eff}$:

$$\begin{aligned}\hat{v}_{eff}(\mathbf{r}) &= \hat{v}(\mathbf{r}) + \frac{\delta J[\rho]}{\delta\rho} + \frac{\delta E_{xc}[\rho]}{\delta\rho} \\ &= \hat{v}(\mathbf{r}) + \int \frac{\rho(\mathbf{r}')}{|\mathbf{r}-\mathbf{r}'|} d\mathbf{r}' + \hat{v}_{xc}(\mathbf{r}).\end{aligned} \tag{3-10}$$

Equation 3-9 leads to the single-particle Schrödinger equation referred to as *Kohn-Sham equation*:

$$\left(-\frac{1}{2}\nabla^2 + \hat{v}_{eff}(\mathbf{r})\right)\psi_i^{KS}(\mathbf{r}) = \epsilon_i^{KS}\psi_i^{KS}(\mathbf{r}). \tag{3-11}$$

One can obtain the ground state density by solving this equation. Since the exact exchange-correlation functional $E_{xc}[\rho]$ is formally still unknown, we need to consider approximations for $E_{xc}[\rho]$.

3.3 The exchange-correlation functional

Various approximations of the exchange-correlation functional have been proposed, and they are categorized in *Jacob's ladder* proposed by Perdew [100]. This ladder consists of five rungs: (1) local-density approximation (LDA), (2) generalized-gradient approximations (GGA), (3) meta-GGAs, (4) hybrid functionals that contain contributions from the Fock or range-separated exchange and depend on occupied orbitals, (5) functionals that depend on all orbitals, occupied as well as unoccupied. The higher is the step of the ladder, the higher is the accuracy of the functional. However, the higher steps are also more computationally demanding than the steps below.

3.3.1 Local-density approximation

The local-density approximation (LDA) is derived from a homogeneous electron gas (HEG) model. The LDA was initially developed by Kohn and Sham [98]. In the LDA, the exchange-correlation energy density per electron at a position is equivalent to the exchange-correlation energy density per electron of the HEG. The exchange-correlation functional is a sum of the exchange functional $E_x^{LDA}[\rho]$ and correlation functional $E_c^{LDA}[\rho]$, and it reads

$$\begin{aligned} E_{xc}^{LDA}[\rho] &= \int \rho(\mathbf{r})\epsilon_{xc}[\rho(\mathbf{r})]\, d\mathbf{r} \\ &= \int \rho(\mathbf{r})\epsilon_x[\rho(\mathbf{r})]\, d\mathbf{r} + \int \rho(\mathbf{r})\epsilon_c[\rho(\mathbf{r})]\, d\mathbf{r} = E_x^{LDA}[\rho] + E_c^{LDA}[\rho], \end{aligned} \tag{3-12}$$

where ϵ_{xc} in Eq. 3-12 represents the exchange-correlation energy density per electron in the HEG. An analytical expression of $E_x^{LDA}[\rho]$ was derived in Ref. [101] and is given by

$$E_x^{LDA}[\rho] = -\frac{3}{4}\left(\frac{3}{\pi}\right)^{1/3} \int \rho(\mathbf{r})^{4/3} d\mathbf{r}. \tag{3-13}$$

$E_c^{LDA}[\rho]$ can be obtained through a parametrization of accurate quantum Monte Carlo (QMC) calculations [102], as in Vosko-Wilk-Nusair (VWM) [103], Perdew-Zunger (PZ) [104], and Perdew-Wang (PW) [105]. Despite the simple approximations, the LDA works successfully for a number of materials. This success is attributed to the facts [106, 107] that the spherically averaged exchange-correlation hole is precisely reproduced and the correct sum rule is satisfied for the LDA exchange-correlation hole, i.e., $\int d^3r' \rho_{xc}^{LDA}(\mathbf{r}, \mathbf{r}') = -1$.

3.3.2 Generalized-gradient approximation

One improves over the LDA by incorporating the gradient of the electronic density in the exchange-correlation functional, and this approach is known as the generalized-gradient approximation (GGA) [108, 109]. The exchange-correlation functional of the GGA can be expressed as

$$\begin{aligned} E_{xc}^{GGA}[\rho] &= \int f^{GGA}[\rho(\mathbf{r}), \nabla\rho(\mathbf{r})]\, d\mathbf{r} \\ &= \int \rho(\mathbf{r})\epsilon_x[\rho(\mathbf{r})] F_{xc}(r_s, s, t)\, d\mathbf{r}, \end{aligned} \tag{3-14}$$

where ϵ_x reflects the exchange energy density used in Eq. 3-12. F_{xc} is an enhancement factor expressed in terms of a dimensionless reduced gradient, s. Here, s is defined as

$$s = \frac{|\nabla\rho(\mathbf{r})|}{2(3\pi^2)^{1/3}\rho(\mathbf{r})^{4/3}}. \tag{3-15}$$

A number of GGA functionals with the different F_{xc} have been reported: Becke88 [110], Lee-Yang-Parr (LYP) [111], Pewdew-Wang (PW) [112], and Perdew-Burke-Ernzerhof (PBE) [113]. The Becke88, PW, and PBE are highly popular functionals. Unlike the Becke functional, PW and PBE use non-empirical parameters for the exchange enhancement factor F_x. Compared to the PW approach, PBE has a simpler form and derivation, but it yields similar results [113]. Therefore, we mainly employ the PBE functional for our calculations.

In the PBE, the exchange energy functional $E_x^{PBE}[\rho]$ is given by

$$E_x^{PBE}[\rho] = \int \rho(\mathbf{r})\epsilon_x[\rho(\mathbf{r})]F_x^{PBE}(s)\, d\mathbf{r}. \tag{3-16}$$

F_x^{PBE} is the simplified exchange enhancement factor:

$$F_x^{PBE}(s) = 1 + \kappa - \frac{\kappa}{(1 + \mu s^2/\kappa)}, \tag{3-17}$$

where κ and μ are non-empirical parameters determined by physical conditions. The correlation energy functional $E_c^{PBE}[\rho]$, in turn, takes the form

$$E_c^{PBE}[\rho] = \int \rho(\mathbf{r})[\epsilon_c(r_s) + H(r_s, t)]\, d\mathbf{r}, \tag{3-18}$$

where t is another dimensionless reduced gradient, which is given by

$$t = \frac{|\nabla\rho(\mathbf{r})|}{2(4k_F/\pi)^{1/2}\rho(\mathbf{r})}. \tag{3-19}$$

The gradient contribution H in Eq. 3-18 is defined as

$$H(r_s, t) = \gamma \ln\left\{1 + \frac{\beta}{\gamma}\, t^2 \left[\frac{1 + At^2}{1 + At^2 + A^2t^4}\right]\right\}, \tag{3-20}$$

where

$$A = \frac{\beta}{\gamma}\,[\exp(-\epsilon_c/\gamma) - 1]^{-1}, \tag{3-21}$$

and $\beta = 0.066725$, $\gamma = (1 - \ln 2)/\pi^2$.

Overall, these GGA functionals provide an improvement of results over the LDA for numerous properties. In spite of successful applications to many systems, the GGA and LDA functionals have deficiencies such as the unphysical self-interaction error and missing van der Waals interaction, which result in incorrect electronic properties [53, 114, 115].

3.4 Van der Waals interactions

Van der Waals (vdW) interactions play a crucial role in weakly interacting systems like organic crystals or layered structures. Unfortunately, conventional DFT calculations are prone to fail to describe long-range vdW interactions as the exchange-correlation functional does not capture such interactions. To address this problem,

one adds an inter-atomic potential to the energy obtained by the DFT. The total energy, including such a dispersion, can be expressed as

$$E_{tot} = E_{DFT} + E_{disp}, \tag{3-22}$$

where E_{disp} represents the long-range dispersion energy. A number of theoretical approaches have been developed to compute the dispersion energy within the DFT [54–63]. In this section, we focus on the DFT-D2 method proposed by Grimme [55], the Tkatchenko-Scheffler (TS) functional [57], and the many-body dispersion method [61].

3.4.1 The DFT-D2 approach

The DFT-D2 method uses an atom-pairwise additive model, and its long-range dispersion energy is given as

$$E_{disp} = -\frac{1}{2} s_6 \sum_{ij} \frac{C_6^{ij}}{(r_{ij})^6} f_d(r_{ij}), \tag{3-23}$$

where s_6 represents a global scaling factor that depends on the exchange-correlation functional. In general, one sets $s_6 = 0.75$ for the PBE functional. r_{ij} is the interatomic distance between i–th and j–th atoms. f_d is a damping function that prevents singularities for small interatomic distances, and it reads

$$f_d(r_{ij}) = \frac{1}{1 + \exp\left[-d(r_{ij}/s_R R_{ij} - 1)\right]}, \tag{3-24}$$

where d is a damping factor that is set to 20, R_{ij} is the sum of the atomic van der Waals radii, i.e., $R_{ij} = R_i + R_j$, and s_R is a scaling parameter that is fixed to one in this approach. We obtain the C_6^{ij} coefficients from a geometric mean of atomic dispersion values, C_6^{ii}:

$$C_6^{ij} = \sqrt{C_6^{ii} C_6^{jj}}. \tag{3-25}$$

This method, which has negligible computational cost, performs well and yields accurate results of binding energies in a wide range of materials. Nevertheless, DFT-D2 has limitations. This method does not include chemical or geometrical environments surrounding each individual atom, but just employs static C_6^{ii} as well as R_i. DFT-D3 can tackle this shortcoming. In contrast to the DFT-D2 method, the dispersion coefficients C_6^{ij} are geometry-dependent. This can be computed by employing the concept of fractional coordination numbers.

3.4.2 TS approach

Tkatchenko and Scheffler [57] devised a density-dependent atom-pairwise approach (TS). Since this method employs the same pairwise interatomic contributions as DFT-D2, the long-range dispersion energy in the TS scheme can also be computed with the equation used in the DFT-D2 (see Eq. 3-23). The difference between the DFT-D2 and TS methods is how dispersion coefficients and van der Waals radii are evaluated. For the TS method, the coefficients and radii are rescaled. The dispersion coefficients C_6^{ii} in a solid can be calculated as follows:

$$C_6^{ii} = C_{6,free}^{ii} \left(\frac{V_i^{eff}}{V_i^{free}} \right)^2, \tag{3-26}$$

where $\frac{V_i^{eff}}{V_i^{free}}$ indicates the ratio between the effective volume of atom i in a solid and the volume of free atom. To compute the ratio, one uses Hirshfeld partitioning [116]:

$$\frac{V_i^{eff}}{V_i^{free}} = \frac{\int r^3 w_i(\mathbf{r}) \rho(\mathbf{r}) d\mathbf{r}^3}{\int r^3 \rho_i^{free}(\mathbf{r}) d\mathbf{r}^3}, \tag{3-27}$$

where the weight for atom i, $w_i(\mathbf{r})$, takes the form

$$w_i(\mathbf{r}) = \frac{\rho_i^{free}(\mathbf{r})}{\sum_j \rho_j^{free}(\mathbf{r})}. \tag{3-28}$$

The C_6^{ij} coefficients are estimated by the Slater−Kirkwood formula [117] in the following way:

$$C_6^{ij} = \frac{2 C_6^{ii} C_6^{jj}}{\left[\frac{\alpha_j}{\alpha_i} C_6^{ii} + \frac{\alpha_j}{\alpha_i} C_6^{jj} \right]}. \tag{3-29}$$

Here, the static polarizability of atom i, α_i, is defined as

$$\alpha_i = \alpha_i^{free} \frac{V_i^{eff}}{V_i^{free}}. \tag{3-30}$$

The Fermi-type damping function (see Eq. 3-24) is also employed in the TS method. For this damping function, one defines rescaled van der Waals radii R_i similar to Eq. 3-26 and Eq. 3-30 as

$$R_i = R_i^{free} \left(\frac{V_i^{eff}}{V_i^{free}} \right)^{1/3}. \tag{3-31}$$

The damping parameter d is set to 20, which is the same as for the DFT-D2 case, and $s_R = 0.94$ is adopted in the case of the PBE functional. In addition, the global scaling factor s_6 is determined to be one. The values of α^{free} and R^{free} correspond to a free-atom polarizability and van der Waals radii, respectively. They are tabulated in Refs. [118, 119].

3.4.3 Many-body dispersion

The atom-pairwise additive models discussed in Secs. 3.4.1 and 3.4.2 sometimes fail to capture dispersion interactions for systems where the many-body nature is essential because they neglect many-body effects as well as screening effects. The many-body dispersion (MBD) method has been developed to incorporate these effects in a van der Waals correction [61]. The MBD approach considers a system of quantum harmonic oscillators (QHOs). In practice, each atom in a system corresponds to a single QHO. The QHO is characterized by a screened polarizability, $\bar{\alpha}_i$, and its characteristic frequency, $\bar{\omega}_i$. For a system of coupled QHOs, one is able to compute the many-body dispersion energy using the coupled fluctuating dipole model (CFDM). The corresponding Hamiltonian is expressed as

$$\mathcal{H} = -\frac{1}{2}\sum_{i=1}^{N}\nabla_{\chi_i}^2 + \frac{1}{2}\sum_{i=1}^{N}\bar{\omega_i}^2\chi_i^2 + \sum_{i=1}^{N}\bar{\omega_i}\bar{\omega_j}\sqrt{\bar{\alpha_i}\bar{\alpha_j}}\chi_i\mathbf{T}_{ij}\chi_i, \tag{3-32}$$

where χ_i denotes the mass-weighted dipole moment of the QHO. The first and second terms of Eq. 3-32 are the kinetic and potential energy of an individual QHOs, respectively. The last term represents dipole-dipole interaction between QHOs. The dipole-dipole interaction tensor, $\mathbf{T}_{ij}$, in Eq. 3-32 is expressed as

$$\mathbf{T}_{ij} = \nabla_{r_i} \otimes \nabla_{r_j} W(r_{ij}), \tag{3-33}$$

in which $W(r_{ij})$ is the range-separated Coulomb potential [120] that attenuates short-range interoscillator interactions:

$$W(r_{ij}) = \frac{1 - \exp\left[-(r_{ij}/\bar{R}_{ij})^{\beta}\right]}{r_{ij}}, \tag{3-34}$$

with $\bar{R}_{ij} = \bar{R}_i + \bar{R}_j$. Here, the range-separated parameter β depends on the exchange-correlation functional. The optimal β for the PBE functional is 2.56 [61]. The many-body dispersion energy can be obtained by diagonalizing the $3N \times 3N$ Hamiltonian matrix in Eq. 3-32, and the energy can be expressed as the difference between the zero-point energy of coupled QHOs and that of uncoupled QHOs:

$$E_{disp} = \frac{1}{2}\sum_{i=1}^{3N}\sqrt{\lambda_i} - \frac{3}{2}\sum_{i=1}^{N}\bar{\omega}_i, \tag{3-35}$$

where λ_i are the Hamiltonian matrix eigenvalues.

The many-body dispersion energy can alternatively be computed by employing a range-separation approach in a dipole-dipole interaction tensor [59]. For this method which is referred to as MBD@rsSCS, one separates the self-consistently screened

atomic polarizabilities into short-range and long-range parts. The dispersion energy is given as

$$E_{disp} = \int_0^\infty \frac{d\omega}{2\pi} \mathrm{Tr}\{\ln(\mathbf{1} - \mathbf{A}_{LR}(\omega)\mathbf{T}_{LR})\}. \tag{3-36}$$

Here, $\mathbf{T}_{LR}$ and $\mathbf{A}_{LR}$ denote the long-range interaction tensor and frequency-dependent polarizability, respectively. Unfortunately, the method was designed for finite non-periodic systems. Therefore, calculations of large supercells are required to obtain the converged dispersion energy, resulting in high computational cost. Such a method is not applicable in systems under periodic boundary conditions, such as solid state systems. To overcome this drawback, a reciprocal space implementation of the approach has been derived [60]. A detailed derivation of the MBD@rsSCS method for periodic systems will be discussed in Sec. 5.3.

3.5 Solving the Kohn-Sham equation

The Kohn-Sham equation (see. Eq. 3-11) defines a non-linear eigenvalue problem because the effective potential $\hat{v}_{eff}(\mathbf{r})$ has a dependence on the wave function obtained from the electron density. To solve this, we need an iterative procedure that employs a linear problem with a fixed potential $\hat{v}^{\mathrm{in}}_{eff}(\mathbf{r})$. The procedure is performed until self-consistency is achieved, and it is known as the *self-consistent field cycle*.

Figure **3-1** shows the self-consistent field cycle to obtain a solution of the Kohn-Sham equation. First, an initial input potential $\hat{v}^{\mathrm{in}}_{eff}(\mathbf{r})$ obtained from an initial guess density $\rho^{\mathrm{in}}(\mathbf{r})$ is constructed, and then one can solve Eq. 3-11 to obtain the wave functions $\psi_i^{KS}(\mathbf{r})$. From the $\psi_i^{KS}(\mathbf{r})$, an output density $\rho^{\mathrm{out}}(\mathbf{r})$ can be computed and, subsequently, this is used to calculate the effective potential $\hat{v}^{\mathrm{out}}_{eff}(\mathbf{r})$. One can obtain ground state properties when effective input and output potentials are equivalent. If the potentials are different, $\hat{v}^{\mathrm{out}}_{eff}(\mathbf{r})$ is served as $\hat{v}^{\mathrm{in}}_{eff}(\mathbf{r})$ for the next iteration. In practice, this iterative process is repeatedly performed until convergence criteria are reached between two consecutive iterations, and $\hat{v}^{\mathrm{in}}_{eff}(\mathbf{r}) \approx \hat{v}^{\mathrm{out}}_{eff}(\mathbf{r})$.

For the self-consistent loop, the convergence is not guaranteed when only $\hat{v}^{\mathrm{out}}_{eff}(\mathbf{r})$ is directly used as the input of the next iteration. Thus, a new input potential is constructed by using both $\hat{v}^{\mathrm{out}}_{eff}(\mathbf{r})$ and $\hat{v}^{\mathrm{in}}_{eff}(\mathbf{r})$. A common approach for the new potential is to mix $\hat{v}^{\mathrm{out}}_{eff}(\mathbf{r})$ and $\hat{v}^{\mathrm{in}}_{eff}(\mathbf{r})$ at every step. One can also achieve self-consistency in the electron density by applying this mixing based on the density instead of the potential.

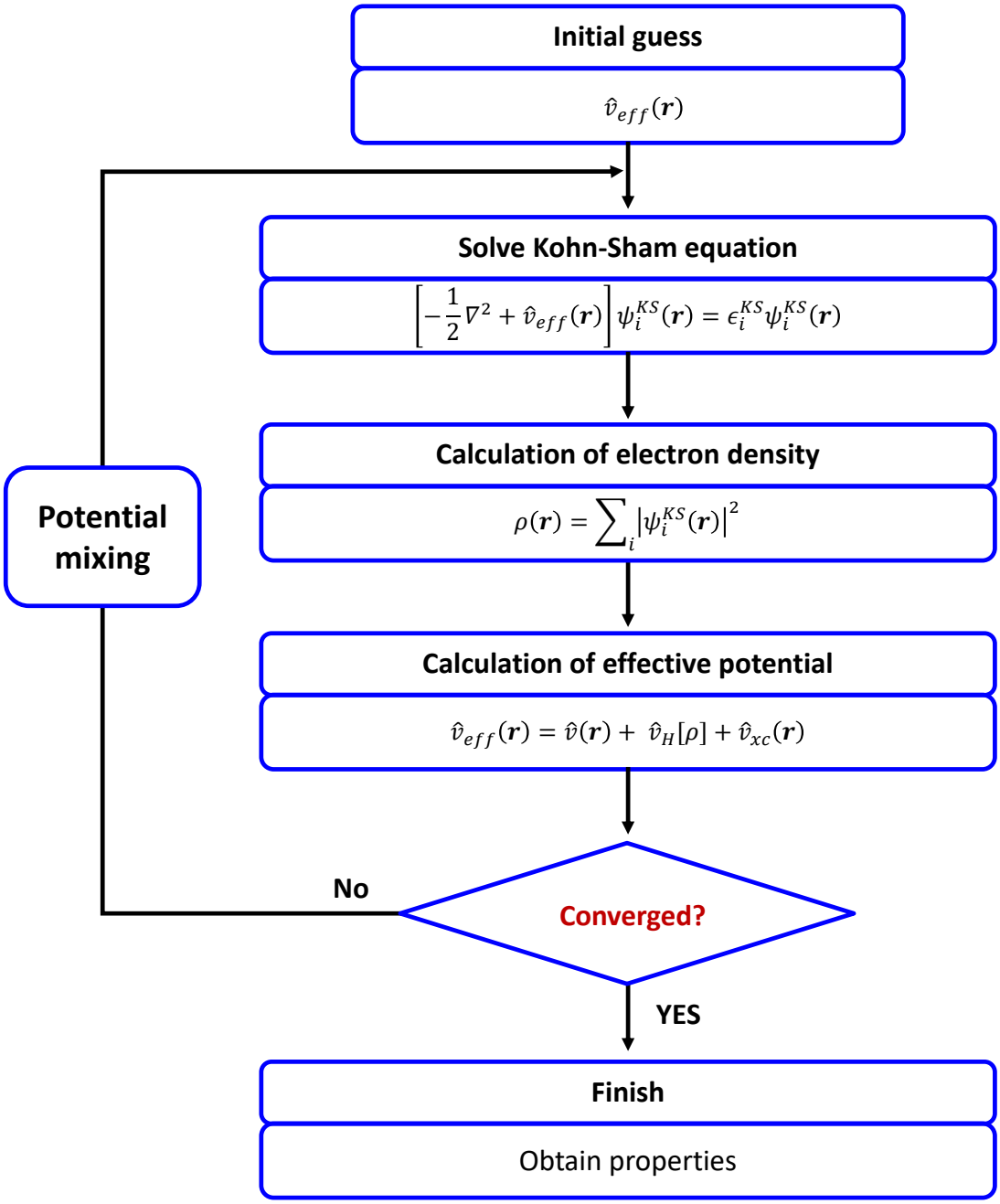

Figure **3-1**: Flow chart of the self-consistent field cycle to solve the Kohn-Sham equations.

3.6 Mixing

Typically, the mixing accelerates convergence of self-consistent field iterations. A number of different mixing methods have been developed [45, 46, 121–128]. In this section, we describe linear mixing, Pulay mixing, and multisecant Broyden methods. For the sake of convenience, we use v instead of $\hat{v}_{eff}$.

3.6.1 Linear mixing

Linear mixing is the simplest method, and it contains a damping parameter α. This mixing is defined as follows:

$$v_{i+1}^{\text{in}}(\mathbf{r}) = v_i^{\text{in}}(\mathbf{r}) + \alpha \left[(v_i^{\text{out}}(\mathbf{r}) - v_i^{\text{in}}(\mathbf{r}) \right], \tag{3-37}$$

In general, α is a value in the range between 0 and 1. There is no mixing in the case of $\alpha = 0$. The efficiency of this mixing depends on α. Indeed, the optimal α varies with respect to modeled systems. For example, for semiconductors and insulators, the convergence becomes faster with a larger value of α, while a smaller value is suitable for metallic systems [129]. However, such significantly small value causes rather slow convergence.

3.6.2 Pulay mixing

Pulay mixing [45, 46] typically outperforms linear mixing, and sometimes it is referred to as *direct inversion in the iterative subspace* (DIIS). The main idea of Pulay mixing is to store past iterations' input potentials $v_i^{\text{in}}(\mathbf{r})$ and residuals $R_i = v_i^{\text{out}}(\mathbf{r}) - v_i^{\text{in}}(\mathbf{r})$ to construct the optimal potential as well as the corresponding residual. They are given as

$$\begin{aligned} v_{\text{opt}}^{\text{in}} &= \Sigma_i \omega_i v_i^{\text{in}} \\ R_{\text{opt}}^{\text{in}} &= \Sigma_i \omega_i R_i^{\text{in}}, \end{aligned} \tag{3-38}$$

where ω_i is the weight coefficient, and it needs to be constrained:

$$\Sigma_i \omega_i = 1. \tag{3-39}$$

With this constraint, one can find ω_i that minimize the norm of the residual $R_{\text{opt}}^{\text{in}}$ [38, 39]:

$$\omega_i = \frac{\Sigma_j A_{ji}^{-1}}{\Sigma_{jk} A_{kj}^{-1}}, \tag{3-40}$$

where

$$A_{ij} = \int R_j^{\text{in}}(\mathbf{r}) R_i^{\text{in}}(\mathbf{r}) d^3 r. \tag{3-41}$$

The $(i{+}1)$-th potential can generally be updated as

$$v_{i+1}^{\text{in}} = v_{\text{opt}}^{\text{in}} + \alpha R_{\text{opt}}^{\text{in}}, \tag{3-42}$$

where α is the parameter as discussed in Sec. 3.6.1. Likewise, this parameter improves the efficiency of convergence.

3.6.3 Multisecant Broyden mixing

Another method showing an improvement over linear mixing is Broyden mixing [121]. This mixing uses an estimated Jacobian from previous iterations, and an updated potential is expressed as

$$v_{i+1}^{\text{in}} = v_{i}^{\text{in}} - \mathcal{J}_i^{-1} R_i, \tag{3-43}$$

where $\mathcal{J}$ denotes the Jacobian, and R_i is the residual. In addition, the mixing consists of two types depending on how the Jacobian is updated: Broyden type–1 and type–2 [121]. The Broyden type–1 directly constructs the Jacobian. After this, one can invert the Jacobian to apply Eq. 3-43. The Broyden type–2 constructs the inverse Jacobian $H = \mathcal{J}^{-1}$, which can be directly used in Eq. 3-43. To reduce computational cost for the construction of these Jacobians, one needs to use an approximation of these Jacobians that satisfies the secant equation:

$$\mathcal{J}_i \left(v_i^{\text{in}} - v_{i-1}^{\text{in}}\right) = R_i - R_{i-1}, \tag{3-44}$$

and

$$H_i \left(R_i - R_{i-1}\right) = v_i^{\text{in}} - v_{i-1}^{\text{in}}. \tag{3-45}$$

Like the standard Broyden mixing, multisecant Broyden mixing considers stored input potentials and residuals of m previous iterations. Newly updated Jacobians of the standard Broyden mixing satisfy the secant equation for only recent potentials and residuals, while those of the multisecant Broyden mixing satisfy all secant equations over the entire m in the following manner:

$$\mathcal{J}_i \, S_i = Y_i, \tag{3-46}$$

and

$$H_i \, Y_i = S_i. \tag{3-47}$$

S_i and Y_i are matrices of differences of the input potential and the residual, and they are defined as

$$\begin{aligned} S_i &= \left[\Delta v_{i-m+1}^{\text{in}}, \Delta v_{i-m+2}^{\text{in}}, \cdots, \Delta v_{i}^{\text{in}}\right] \\ Y_i &= \left[\Delta R_{i-m+1}, \Delta R_{i-m+2}, \cdots, \Delta R_{i}\right]. \end{aligned} \tag{3-48}$$

These Jacobians can be analytically estimated as [35, 124]

$$\mathcal{J}_i = \mathcal{J}_{i-1} + (Y_i - \mathcal{J}_{i-1}S_i)(S_i^T S_i)^{-1}S_i^T, \tag{3-49}$$

for the multisecant Broyden type-1 method and

$$H_i = H_{i-1} + (S_i - H_{i-1}Y_i)(Y_i^T Y_i)^{-1}Y_i^T, \tag{3-50}$$

for its type-2 method.

Marks and Luke devised a method where scaling, regularization and preconditioning techniques are added in the multisecant Broyden mixing [124, 130]. An updated potential method is given by

$$v_{i+1}^{\text{in}} = v_i^{\text{in}} - A_0(I - Y_{i-1}A_i)R_i - S_{i-1}A_iR_i, \tag{3-51}$$

where A_i depends on the type of method. A_0 represents an initial inverse Jacobian estimate, and this can be approximated as $A_0 = \sigma I$, where σ is a dynamic step length. Marks and Luke confirmed that including preconditioning and regularization approaches in A_i improves a performance [124]. For the multisecant Broyden type-1 method, A_i can be constructed as

$$A_i = \Psi_i \left(\Psi_i \hat{S}_{i-1}^T \hat{Y}_{i-1}\Psi_i + \alpha I\right)^{-1} \Psi_i \hat{S}_{i-1}^T \Omega_i, \tag{3-52}$$

where α is the regularization parameter [131]. Ψ_i is a diagonal matrix and it renormalizes Y_i. Here, one defines $\hat{S}_i = \Omega_i S_i$ and $\hat{Y}_i = \Omega_i Y_i$ with the preconditioner Ω_i. This method has been initially implemented in WIEN2k [132]. In **exciting** [34], a simplified variant of it, which does not involve scaling and an approach for controlling the step size, has been implemented.

3.6.4 Charge sloshing

Although various mixing methods, such as the Pulay mixing and multisecant Broyden mixing, accelerate and stabilize convergence of SCF iterations in a wide range of systems, some cases still show instabilities to reach self-consistency due to charge sloshing [35–42], i.e., the charge density oscillates during iterations. Charge sloshing is particularly problematic in metallic systems with a large unit cell. The error in the output potential is given by

$$\delta v_{\text{KS}}^{\text{out}}(\mathbf{G}) = \sum_{\mathbf{G}} \frac{4\pi}{G^2}\chi(|\mathbf{G}|)\delta v_{\text{KS}}^{\text{in}}(\mathbf{G}). \tag{3-53}$$

It can be clearly seen in Eq. 3-53 that because of G^{-2} in the Hartree potential, the error diverges quadratically at small nonzero $\mathbf{G}$ components. Therefore, the change

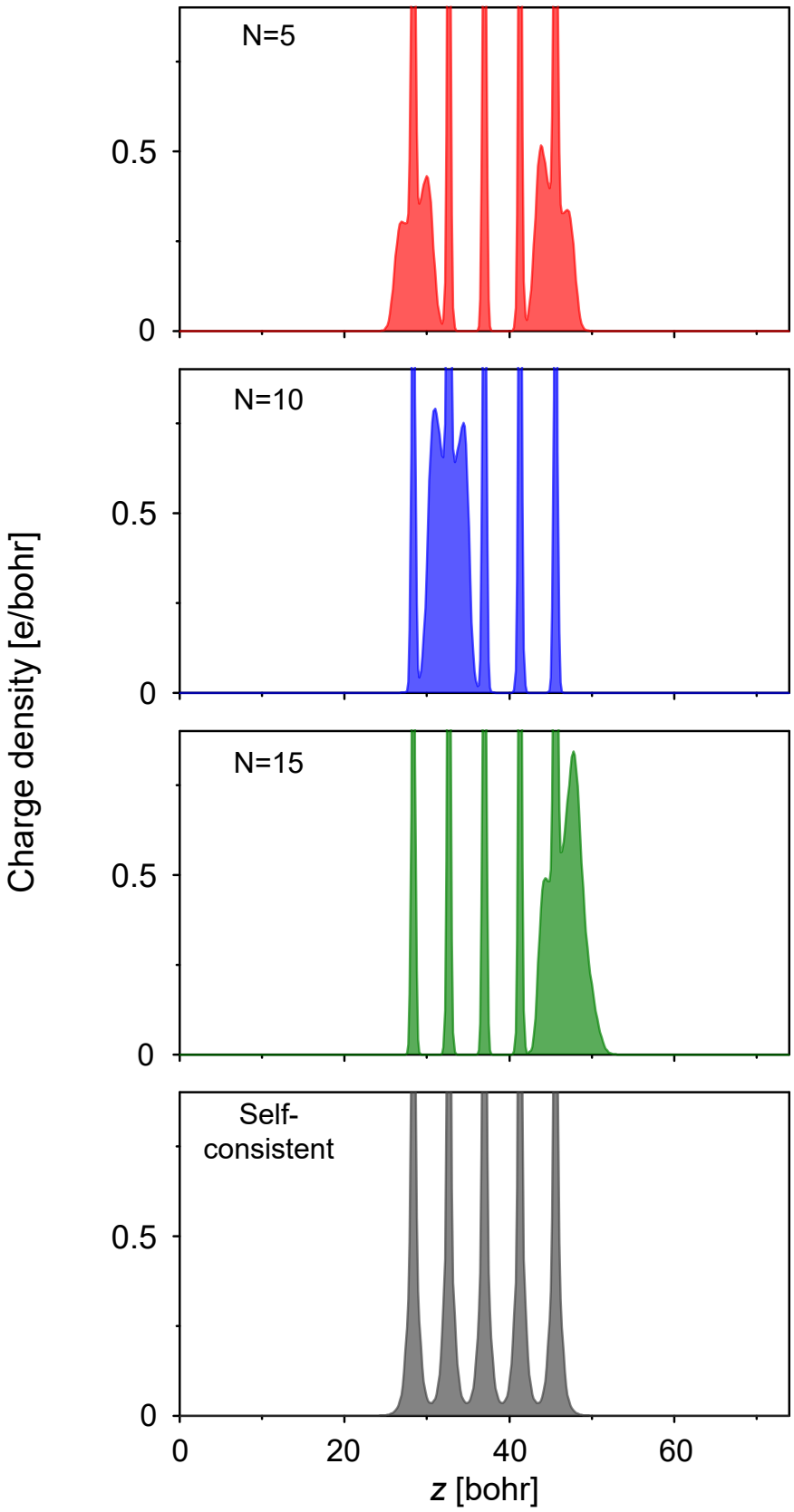

Figure **3-2**: An illustration of charge sloshing for the Pd(111) surface. Plane-averaged charge densities after 5– (red), 10– (blue), and 15– (green) iterations that are performed by linear mixing. For comparison, the fully converged charge density (gray) obtained by a robust mixing is shown.

in the input potential δv^{in} is amplified. This is the main source of the charge sloshing. Such an issue is worse for large unit cells that have extremely small $\mathbf{G}$. In the case of insulating systems, the susceptibility can be expressed as $\chi(|\mathbf{G}|) \propto G^{-2}$ [133]. The susceptibility cancels out G^{-2} in the Hartree potential. On the other hand, the susceptibility of metallic systems is a constant, therefore, this cannot suppress pronounced charge sloshing.

Figure **3-2** demonstrates the charge sloshing instability in Pd(111) with five atomic layers. We use the linear mixing algorithm in this calculation. In the figure, the gray curve denotes the self-consistent charge density, which is obtained by another robust mixer. We observe that the charge density largely fluctuates within the Pd slab during iterations. For example, the density at the 10–th iteration is more localized at the bottom side of the slab, while it is mainly distributed at the upper side in the case of 15–th iterations. Therefore, the linear mixing does not lead to the converged density, and does not reach self-consistency due to the oscillatory behavior.

To address this charge sloshing problem, numerous methods have been introduced [36–39, 134–136]. Typically, one considers the Kerker preconditioner [37], which stabilizes SCF convergence for large-scale metallic systems. The preconditioner is given in reciprocal space as

$$P(\mathbf{G}) = \alpha \frac{G^2}{G^2 + \lambda^2}, \tag{3-54}$$

with the screening parameter λ. When $\mathbf{G}$ is quite big, the right-hand side of Eq. 3-54 becomes equal to α, and then conventional mixing methods are performed. On the other hand, when $\mathbf{G}$ is small, $P(\mathbf{G}) \sim \alpha\, G^2/\lambda^2$, which leads to damping of potentials in the mixing.

4. Electronic structure methods

The Kohn-Sham equations can be solved with a variety of methods. We will focus on the family of the full-potential all-electron methods based on linearised augmented plane waves (FP-LAPW). They enable a highly precise description of the electronic structure. These methods take into account the behavior of wave functions that vary rapidly and in some cases oscillate in the vicinity of nuclei.

4.1 The APW method

The augmented plane-wave (APW) approach was proposed by Slater [137]. In this method, a unit cell consists of spheres centered at atomic positions known as muffin-tin (MT) spheres and the interstitial region (I). Figure **4-1** displays the space division of a unit cell. The basis functions are described differently, depending on these regions. They are defined as follows:

$$\phi_{\mathbf{G}+\mathbf{k}}(\mathbf{r}) = \begin{cases} \frac{1}{\sqrt{\Omega}} e^{i(\mathbf{G}+\mathbf{k})\mathbf{r}} & \mathbf{r} \in I \\ \sum_{lm} A_{lm\alpha}^{\mathbf{G}+\mathbf{k}} u_{l\alpha}(r_\alpha) Y_{lm}(\widehat{\mathbf{r}}_\alpha) & \mathbf{r} \in \mathrm{MT}_\alpha, \end{cases} \tag{4-1}$$

where $\mathbf{G}$ are reciprocal lattice vectors, Ω is the volume of the unit cell, and l and m are the azimuthal quantum number and the magnetic quantum number, respectively. $\mathbf{k}$ is the Bloch vector and $\mathbf{r}_\alpha$ is the difference between $\mathbf{r}$ and the center position of atoms labelled α, i.e., $\mathbf{r}_\alpha = \mathbf{r} - \mathbf{R}_\alpha$. In the interstitial region, planewaves are employed, whereas spherical harmonics and radial functions expand $\phi_{\mathbf{G}+\mathbf{k}}(\mathbf{r})$ inside MT spheres. $A_{lm\alpha}$ are coefficients that match the basis functions between MTs and I at the atomic sphere boundary. With the Rayleigh expansion, $A_{lm\alpha}^{\mathbf{G}+\mathbf{k}}$ is given as

$$A_{lm\alpha}^{\mathbf{G}+\mathbf{k}} = \frac{4\pi}{\sqrt{\Omega}} e^{i(\mathbf{G}+\mathbf{k})\mathbf{R}_\alpha} i^l Y_{lm}^*(\widehat{\mathbf{G}+\mathbf{k}}) \frac{j_l(|\mathbf{G}+\mathbf{k}|\, r_\alpha)}{u_{l\alpha}(r_\alpha)}, \tag{4-2}$$

where $j_l(kr)$ are spherical Bessel functions. To obtain $u_{l\alpha}(r_\alpha)$, one solves the radial Schrödinger equation with the spherically averaged potential $v(r)$:

$$\left[-\frac{1}{2} \frac{\mathrm{d}^2}{\mathrm{d}r^2} + \frac{l(l+1)}{2r^2} + v(r) - \epsilon_{i\mathbf{k}} \right] r u_{l\alpha}(r_\alpha) = 0. \tag{4-3}$$

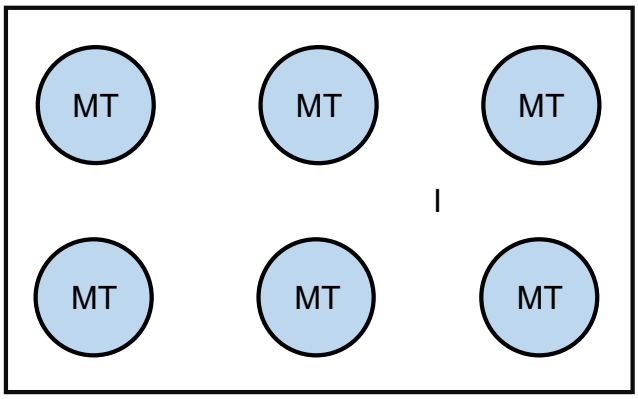

Figure **4-1**: Muffin-tin (MT) spheres and their surrounding interstitial region (I) in the unit cell.

One solves the Kohn-Sham equation in Eq. 3-11 by expanding the Kohn-Sham wave functions in terms of the basis set. The Kohn-Sham wave functions are expressed as:

$$\psi_{i\mathbf{k}}(\mathbf{r}) = \sum_{\mathbf{G}} C^{\mathbf{k}}_{i\mathbf{G}} \phi_{\mathbf{G}+\mathbf{k}}(\mathbf{r}). \tag{4-4}$$

With the APW basis, the Kohn-Sham equation transforms into

$$H^{\mathbf{k}} C^{\mathbf{k}} = \epsilon^{\mathbf{k}} S^{\mathbf{k}} C^{\mathbf{k}}, \tag{4-5}$$

where $S^{\mathbf{k}}$ and $H^{\mathbf{k}}$ are the overlap and Hamiltonian matrices, respectively. They are constructed as

$$H^{\mathbf{k}}_{\mathbf{GG'}} = \langle \phi_{\mathbf{G}+\mathbf{k}}| -\frac{1}{2}\nabla^2 + \hat{v}_{eff}(\mathbf{r}) \,|\phi_{\mathbf{G'}+\mathbf{k}}\rangle \,, \tag{4-6}$$

and

$$S^{\mathbf{k}}_{\mathbf{GG'}} = \langle \phi_{\mathbf{G}+\mathbf{k}}|\phi_{\mathbf{G'}+\mathbf{k}}\rangle \,. \tag{4-7}$$

Equations 4-6 and 4-7 have an implicit dependence on the eigenenergy of the secular equation, since the APW basis is constructed using $\epsilon_{i\mathbf{k}}$. Thus, Eq. 4-5 is non-linear in the energy. Therefore, the APW method is computationally inefficient.

4.2 The LAPW method

To avoid the shortcoming of the APW approach, the *Linearized Augmented Planewave* (LAPW) method was introduced by Andersen [138]. To eliminate the dependence of the basis on the eigenenergy, one introduces the energy derivative of $u_{l\alpha}(r_\alpha, \epsilon)$, i.e., $\dot{u}_{l\alpha}(r_\alpha, \epsilon_{l\alpha}) = \partial u_{l\alpha}(r_\alpha, \epsilon)/\partial\epsilon$, where $\epsilon_{l\alpha}$ is a fixed linearization energy. The LAPW

basis is given by

$$\phi^{LAPW}_{\mathbf{G+k}}(\mathbf{r}) = \begin{cases} \frac{1}{\sqrt{\Omega}} e^{i(\mathbf{G+k})\mathbf{r}} & \mathbf{r}\in I \\ \sum_{lm} \left[A^{\mathbf{G+k}}_{lm\alpha} u_{l\alpha}(r_\alpha, \epsilon_{l\alpha}) + B^{\mathbf{G+k}}_{lm\alpha} \dot{u}_{l\alpha}(r_\alpha, \epsilon_{l\alpha}) \right] Y_{lm}(\widehat{\mathbf{r}}_\alpha) & \mathbf{r}\in \mathrm{MT}_\alpha, \end{cases} \tag{4-8}$$

One determines two coefficients $A_{lm\alpha}$ and $B_{lm\alpha}$ to ensure continuity of value and slope of $\phi^{LAPW}_{\mathbf{G+k}}(\mathbf{r})$ at the boundary between MTs and I.

Two cutoff parameters are introduced: (i) the planewave cutoff G_{max} and (ii) the maximum angular momentum in the MT spheres, l_{max}. l_{max} restricts the spherical harmonics expansion in the basis functions of MTs. G_{max} determines the size of the basis, and thus controls the accuracy of calculations [also the lm expansion is also important for the precision]. However, as shown in Eq. 4-8, the basis set has also a dependence on the muffin-tin sphere radius R_{MT}. For a given level of accuracy, the bigger is R_{MT}, the smaller G_{max} is required, since the wave functions away from the nuclei are easier to describe than nearby the nuclei. In practice, therefore, one uses a dimensionless parameter $R^{min}_{MT} G_{max}$, where R^{min}_{MT} denotes the smallest muffin-tin sphere radius of a species in a system.

4.3 The APW+lo method

The LAPW basis does not depend on the Kohn-Sham energies, but it requires an increased number of basis functions compared to the APW to attain the same level of accuracy. Such a property is explained by the continuous first derivative at the muffin-tin boundary. An alternative method has been proposed to combine the advantages of the APW and LAPW methods [139]. In this method, a set of local orbitals (lo) is added to the APW basis (APW+lo). The APW+lo is composed of two types basis functions. One is the original basis functions of Eq. 4-1 with fixed energies $\epsilon_{l\alpha}$ in the following manner:

$$\phi_{\mathbf{G+k}}(\mathbf{r}) = \begin{cases} \frac{1}{\sqrt{\Omega}} e^{i(\mathbf{G+k})\mathbf{r}} & \mathbf{r}\in I \\ \sum_{lm} A^{\mathbf{G+k}}_{lm\alpha} u_{l\alpha}(r_\alpha, \epsilon_{l\alpha}) Y_{lm}(\widehat{\mathbf{r}}_\alpha) & \mathbf{r}\in \mathrm{MT}_\alpha, \end{cases} \tag{4-9}$$

The other is the local orbitals (lo) that can be expressed as

$$\phi^{lo}(\mathbf{r}) = \begin{cases} 0 & \mathbf{r}\in I \\ \left[A^{lo}_{lm\alpha} u_{l\alpha}(r_\alpha, \epsilon_{l\alpha}) + B^{lo}_{lm\alpha} \dot{u}_\alpha(r_\alpha, \epsilon_{l\alpha}) \right] Y_{lm}(\widehat{\mathbf{r}}_\alpha) & \mathbf{r}\in \mathrm{MT}_\alpha, \end{cases} \tag{4-10}$$

The two coefficients $A^{lo}_{lm\alpha}$ and $B^{lo}_{lm\alpha}$ satisfy the following conditions: (i) zero value of the local orbitals at the atomic sphere boundary and (ii) normalization of the local

orbitals $\int_\Omega \left|\phi^{lo}(\mathbf{r})\right|^2 d\mathbf{r} = 1$. Using this APW+lo method, the wave functions in the MT region become

$$\begin{aligned}\psi_{i\mathbf{k}}(\mathbf{r}) = &\sum_{\mathbf{G}}\sum_{lm} C^{\mathbf{k}}_{i\mathbf{G}} A^{\mathbf{G}+\mathbf{k}}_{lm\alpha} u_{l\alpha}(r_\alpha, \epsilon_{l\alpha}) \\ &+ \sum_{lm} C^{\mathbf{k}}[A^{lo}_{lm\alpha} u_{l\alpha}(r_\alpha, \epsilon_{l\alpha}) + B^{lo}_{lm\alpha}\dot{u}_\alpha(r_\alpha, \epsilon_{l\alpha})]\, Y_{lm}(\widehat{\mathbf{r}}_\alpha).\end{aligned} \tag{4-11}$$

One can also include higher-order derivatives of $u_{l\alpha}(r_\alpha, \epsilon)$ in this method, e.g.,

$$\phi^{lo}(\mathbf{r}) = \left[A^{lo}_{lm\alpha} u_{l\alpha}(r_\alpha, \epsilon_{l\alpha}) + B^{lo}_{lm\alpha}\ddot{u}_{l\alpha}(r_\alpha, \epsilon_{l\alpha})\right] Y_{lm}(\widehat{\mathbf{r}}_\alpha), \tag{4-12}$$

where the coefficients are determined by the same requirements as described above. Equation 4-12 can be represented by combinations of $\dot{u}_{l\alpha}(r_\alpha, \epsilon_{l\alpha})$ and $\ddot{u}_{l\alpha}(r_\alpha, \epsilon_{l\alpha})$.

4.4 Potential and density formalism in FP-LAPW

The full-potential LAPW method [141, 142] does not use shape approximations in the interstitial region and muffin-tin spheres for the full-potential and charge density, which are applied to the Kohn-Sham equation. In the interstitial and muffin-tins, one expands the potential (and density) into planewaves and spherical harmonics, respectively:

$$v(\mathbf{r}) = \begin{cases} \sum\limits_{\mathbf{G}} v_I(\mathbf{G}) e^{i\mathbf{G}\mathbf{r}} & \mathbf{r}\in I \\ \sum\limits_{lm} v^\alpha_{lm}(\mathbf{r}) Y_{lm}(\widehat{\mathbf{r}}) & \mathbf{r}\in \mathrm{MT}_\alpha, \end{cases} \tag{4-13}$$

and

$$\rho(\mathbf{r}) = \begin{cases} \sum\limits_{\mathbf{G}} \rho_I(\mathbf{G}) e^{i\mathbf{G}\mathbf{r}} & \mathbf{r}\in I \\ \sum\limits_{lm} \rho^\alpha_{lm}(\mathbf{r}) Y_{lm}(\widehat{\mathbf{r}}) & \mathbf{r}\in \mathrm{MT}_\alpha. \end{cases} \tag{4-14}$$

The electron density under periodic boundary conditions is constructed as

$$\rho(\mathbf{r}) = \sum_{\mathbf{k}} \omega_{\mathbf{k}} \sum_{\mathrm{i}} f_{\mathrm{i}\mathbf{k}} \left|\psi_{\mathrm{i}\mathbf{k}}(\mathbf{r})\right|^2, \tag{4-15}$$

where $f_{\mathrm{i}\mathbf{k}}$ represents the occupation factor, and $\omega_{\mathbf{k}}$ is the weight of the $\mathbf{k}$-point.

4.4.1 Evaluation of the Hartree potential

After $\rho(\mathbf{r})$ is constructed, one evaluates the Hartree potential $v_H(\mathbf{r})$. $v_H(\mathbf{r})$ is determined via the Poisson equation:

$$\nabla^2 v_H(\mathbf{r}) = -4\pi\rho(\mathbf{r}). \tag{4-16}$$

In reciprocal space, the solution of the Poisson equation is straightforwardly

$$v_H(\mathbf{G}) = \frac{4\pi\rho(\mathbf{G})}{G^2}. \tag{4-17}$$

However, in the FP-LAPW scheme, $\rho(\mathbf{r})$ varies significantly near the nuclei. This indicates that a Fourier transformation of $\rho(\mathbf{r})$ is neither easy nor fast to perform. Therefore, directly computing $v_H(\mathbf{r})$ based on Eq. 4-17 is inefficient. This drawback can be addressed via the pseudo-charge method proposed by Weinert [143]. In this method, one constructs a smooth pseudo-charge density $\bar{\rho}(\mathbf{r})$ that yields the correct electrostatic potential v_H in the interstitial region. The charge density in the muffin-tin spheres contributes to the potential in the interstitial region as follows:

$$v(\mathbf{r}) = \sum_{l=0}^{\infty}\sum_{m=-l}^{l}\frac{4\pi}{2l+1}\frac{q_{lm}^{\alpha}}{r^{l+1}}Y_{lm}(\widehat{\mathbf{r}}_{\alpha}), \tag{4-18}$$

where the multipole moments q_{lm}^{α} are defined as

$$q_{lm}^{\alpha} = \int_{S_{\alpha}} Y_{lm}^{*}(\widehat{\mathbf{r}})r^{l}\rho(\mathbf{r})d\mathbf{r}. \tag{4-19}$$

According to the pseudo-charge method, $\rho(\mathbf{r})$ is substituted with the pseudo-charge density $\bar{\rho}(\mathbf{r})$. $\bar{\rho}(\mathbf{r})$ is defined as a sum of the interstitial density and the density in each muffin-tin sphere that is replaced by a smooth one $\tilde{\rho}^{\alpha}(\mathbf{r})$: $\rho(\mathbf{r}) \rightarrow \bar{\rho}(\mathbf{r}) = \rho_I(\mathbf{r}) + \sum_{\alpha}\tilde{\rho}^{\alpha}(\mathbf{r})$. Note that the multipole moments of $\bar{\rho}(\mathbf{r})$ and $\rho(\mathbf{r})$ are identical. The potential in the interstitial region becomes

$$v_I(\mathbf{r}) = \sum_{\mathbf{G}}\frac{4\pi}{G^2}\ \bar{\rho}(\mathbf{G})e^{i\mathbf{G}\mathbf{r}}. \tag{4-20}$$

For Eq. 4-20, one performs the Fourier transform of $\tilde{\rho}^{\alpha}(\mathbf{r})$, given by

$$\tilde{\rho}^{\alpha}(\mathbf{G}) = \frac{4\pi}{\Omega}e^{-i\mathbf{G}\cdot\mathbf{R}^{\alpha}}\sum_{l=0}^{\infty}\sum_{m=-l}^{l}\frac{(-i)^{l}}{(2l+1)!!}\frac{(2l+2n+3)!!j_{l+n+1}(GR_{\alpha})}{R_{\alpha}^{l+n+1}G^{n+1}}Y_{lm}(\widehat{\mathbf{G}})\tilde{q}_{lm}^{\alpha}, \tag{4-21}$$

where n is a parameter, and $j_l(r)$ represent the Bessel functions of the first kind. In case of $\mathbf{G} = 0$, Eq. 4-21 transforms into

$$\tilde{\rho}^{\alpha}(0) = \frac{\sqrt{4\pi}}{\Omega}\tilde{q}_{00}^{\alpha}. \tag{4-22}$$

The potential in the muffin-tin region is determined by the Dirichlet boundary value problem. We obtain this potential by employing the Green's function method [144]. The Green's function reads

$$\mathcal{G}(\mathbf{r},\mathbf{r}') = \sum_{l=0}^{\infty}\sum_{m=-l}^{l}\frac{4\pi}{2l+1}\frac{r_{<}^{l}}{r_{>}^{l+1}}\left(1-\frac{r_{>}^{2l+1}}{R_{\alpha}^{2l+1}}\right)Y_{lm}^{*}(\widehat{\mathbf{r}}')Y_{lm}(\widehat{\mathbf{r}}), \tag{4-23}$$

with $r_<$ ($r_>$) being the larger (smaller) value of $\mathbf{r}$ and $\mathbf{r}'$, and the normal derivative of $\mathcal{G}(\mathbf{r}, \mathbf{r}')$ is given by

$$\begin{aligned} \frac{\partial \mathcal{G}}{\partial n'} &= \left.\frac{\partial \mathcal{G}}{\partial r'}\right|_{r'=R_\alpha} \\ &= -\frac{4\pi}{R_\alpha^2} \sum_{l=0}^{\infty} \sum_{m=-l}^{l} Y_{lm}^*(\widehat{\mathbf{r}}') Y_{lm}(\widehat{\mathbf{r}}) \frac{r^l}{R_\alpha^l}. \end{aligned} \tag{4-24}$$

Part II

Results

5. Implementation and applications

We present the development and implementation of advanced mixing methods with the Kerker preconditioner as well as the inverse Kerker metric. We further implement a range-separated (rs) many-body dispersion method under periodic boundary conditions that involves the self-consistent screening (SCS) of polarizabilities (MBD@rsSCS).

5.1 Advanced mixers

5.1.1 Kerker method in LAPW

As discussed in Sec. 3.6.4, calculations of metallic systems with a large unit cell fail because a small change of v_i^{in} can cause a significant change of v_i^{out} at small $\mathbf{G}$ components. Such an issue, known as charge-sloshing [35–42] leads to large charge fluctuations during the self-consistency iterations. The Kerker preconditioner can remarkably stabilize calculations and accelerate self-consistency [37]. The mixing involving the preconditioner is referred to as to Kerker mixing and it is given as

$$v_{i+1}^{\text{in}}(\mathbf{G}) = v_i^{\text{in}}(\mathbf{G}) + \alpha \frac{G^2}{G^2 + \lambda^2} \left(v_i^{\text{out}}(\mathbf{G}) - v_i^{\text{in}}(\mathbf{G}) \right), \tag{5-1}$$

where λ is a parameter. The implementation of Eq. 5-1 is straightforward in the planewave method, but not as simple in other methods. As described in Chapter 4, the unit cell consists of the interstitial region and atomic spheres (MT_α). In general, one can evaluate the potential and density as Eqs. 4-13 and 4-14. The potential and density are expanded into spherical harmonics series in the muffin-tin spheres, while the expansion in terms of planewaves is carried out in the interstitial region. Thus, applying a Fourier transform to the potential or density is impractical for this method. In other words, it is not appropriate to calculate directly v_{i+1}^{in} using Eq. 5-1.

We reformulate Eq. 5-1 into a real space representation to make it compatible with the FP-LAPW method. The equation then becomes

$$v_{i+1}^{\text{in}}(\mathbf{r}) = v_i^{\text{in}}(\mathbf{r}) + \alpha \left(1 + \lambda^2 \left[\nabla^2 - \lambda^2\right]^{-1}\right) \left(v_i^{\text{out}}(\mathbf{r}) - v_i^{\text{in}}(\mathbf{r})\right). \tag{5-2}$$

The operator $\hat{K} = [\nabla^2 - \lambda^2]^{-1}$ is not directly applicable to a function. Instead, we evaluate $V(\mathbf{r}) = \hat{K} f(\mathbf{r})$ with some function $f(\mathbf{r})$ by solving the screened Poisson equation as follows:

$$\left(\nabla^2 - \lambda^2\right) V(\mathbf{r}) = f(\mathbf{r}). \tag{5-3}$$

For example, when $f(\mathbf{r}) = -4\pi\rho(\mathbf{r})$, $V(\mathbf{r})$ is equivalent to the potential induced by the charge density $\rho(\mathbf{r})$ assuming screened Coulomb interaction. Therefore, we can apply the operator by treating Eq. 5-3 like it is an electrostatic problem, where we use $\rho(\mathbf{r}) = -\left[v_i^{\text{out}}(\mathbf{r}) - v_i^{\text{in}}(\mathbf{r})\right]/4\pi$ as an input. Afterwards, $V(\mathbf{r})$ can be obtained. The screened Poisson equation can be solved via Weinert's pseudo-charge method [143]. Originally, it was used to evaluate the Hartree potential in the FP-LAPW method, as explained in Sec. 4.4.1. However, Ref. [145] showed that the screened Poisson equation can also be solved in the same manner. Although that study, which uses Weinert's algorithm, was focused on implementing the screened exchange in a hybrid exchange-correlation functional, the algorithm is also suitable for our implementation. We outline essential steps of the method below.

We note that the input *charge density* for this pseudo-charge method has the same form as Eq. 4-13. In the first step, a smooth pseudo-charge density $\bar{\rho}(\mathbf{r})$, which can easily perform the Fourier transform, substitutes the charge density $\rho(\mathbf{r})$. The pseudo-charge density can be expressed as

$$\bar{\rho}(\mathbf{r}) = \sum_{\mathbf{G}} \rho_{\mathbf{G}} e^{i\mathbf{G}\mathbf{r}} + \sum_{\alpha} \tilde{\rho}^{\alpha}(\mathbf{r}). \tag{5-4}$$

The first term of Eq. 5-4 represents the interstitial density. Dissimilar to Eq. 4-13, in Eq. 5-4 planewaves are extended into the muffin-tin spheres . The smoothly varying density $\tilde{\rho}^{\alpha}(\mathbf{r})$ is constructed in the muffin-tin spheres, and it is given by

$$\tilde{\rho}^{\alpha}(\mathbf{r}) = \sum_{l=0}^{\infty} \sum_{m=-l}^{l} Q_{lm}^{\alpha} Y_{lm}(\widehat{\mathbf{r}}) \sigma_{lm}^{\alpha}(r), \tag{5-5}$$

where Q_{lm}^{α} are constants that are obtained such that multipole moments of $\bar{\rho}(\mathbf{r})$ are equal to those of $\rho(\mathbf{r})$. In the case of the screened Coulomb interaction, the multipole moments inside the muffin-tin spheres are defined as follows:

$$q_{lm}^{\alpha} = \frac{(2l+1)!!}{\lambda^l} \int_{S_{\alpha}} Y_{lm}^{*}(\widehat{\mathbf{r}}) i_l(\lambda r) \rho(\mathbf{r}) d\mathbf{r}, \tag{5-6}$$

where $i_l(r)$ are the modified spherical Bessel functions of the first kind. Due to the interstitial charge density being extended into the muffin-tin spheres, the multipole moments q_{lm}^{α} are modified. These modified multipoles $\tilde{q}_{lm}^{\alpha}$ are given as

$$\tilde{q}_{lm}^{\alpha} = Q_{lm}^{\alpha} \frac{(2l+1)!!}{\lambda^l} \int_{S_\alpha} i_l(\lambda r)\ \rho(\mathbf{r})\ \sigma_{lm}^{\alpha}(r) d\mathbf{r}. \tag{5-7}$$

One can define $\tilde{q}_{lm}^{\alpha}$ as the difference between the multipoles inside the muffin-tin spheres and those of the extended interstitial charge: $\tilde{q}_{lm}^{\alpha} = q_{lm}^{\alpha} - q_{lm}^{I\alpha}$, where $q_{lm}^{I\alpha}$ reads:

$$\begin{aligned} q_{lm}^{I\alpha} = & \sum_{\mathbf{G}} \frac{4\pi(2l+1)!! i^l R_\alpha^2}{\lambda^l (G^2+\lambda^2)} \rho_{\mathbf{G}} e^{i\mathbf{G}\cdot\mathbf{R}^\alpha} Y_{lm}^*(\widehat{\mathbf{G}}) \\ & \times \left(\lambda j_l(GR_\alpha) i_{l-1}(\lambda R_\alpha) - \mathbf{G} j_{l-1}(GR_\alpha) i_l(\lambda R_\alpha)\right), \end{aligned} \tag{5-8}$$

with $j_l(r)$ being the spherical Bessel functions of the first kind. For $\mathbf{G} = 0$, Eq. 5-8 becomes

$$\delta_{l0}\sqrt{4\pi} \frac{R_\alpha^2 i_1(\lambda R_\alpha)}{\lambda} \rho_0. \tag{5-9}$$

Next, an arbitrary function in Eq. 5-5 is expressed as

$$\sigma_{lm}^{\alpha}(r) = r^l \left(1 - \frac{r^2}{R_\alpha^2}\right)^n. \tag{5-10}$$

Here, $n = \frac{R_\alpha G_{max}}{2}$ is generally used [146], whereas we find that results are less sensitive to $n = \frac{R_\alpha G_{max}}{4}$ for our cases. With these formulas, we analytically carry out a Fourier transform of $\tilde{\rho}^{\alpha}(\mathbf{r})$, and it reads

$$\tilde{\rho}^{\alpha}(\mathbf{G}) = \frac{4\pi}{\Omega} e^{-i\mathbf{G}\cdot\mathbf{R}^\alpha} \sum_{l=0}^{\infty} \sum_{m=-l}^{l} \frac{(-i)^l}{(2l+1)!!} \frac{\lambda^{l+n+1} j_{l+n+1}(GR_\alpha)}{i_{l+n+1}(\lambda R_\alpha) G^{n+1}} Y_{lm}(\widehat{\mathbf{G}}) \tilde{q}_{lm}^{\alpha}. \tag{5-11}$$

For $\mathbf{G} = 0$, Eq. 5-11 becomes

$$\tilde{\rho}^{\alpha}(0) = \frac{\sqrt{4\pi}}{\Omega} \frac{(\lambda R_\alpha)^{n+1}}{(2n+3)!! i_{n+1}(\lambda R_\alpha)} \tilde{q}_{00}^{\alpha}. \tag{5-12}$$

After performing the Fourier transform of Eq. 5-4, the interstitial potential using the pseudo-charge density can be expressed by

$$V_I(\mathbf{G}) = \frac{4\pi}{G^2+\lambda^2}\ \bar{\rho}(\mathbf{G}). \tag{5-13}$$

We obtain the potential inside the muffin-tin region by solving the Dirichlet boundary-value problem with the original density $\rho(\mathbf{r})$. For this, a Green's function method [144] is employed, and the potential can be written as

$$V^{\alpha}(\mathbf{r}) = \int_{MT_\alpha} \mathcal{G}(\mathbf{r}, \mathbf{r}') \rho(\mathbf{r}') d\mathbf{r}' - \frac{R_\alpha^2}{4\pi} \oint_{S_\alpha} V_I(R_\alpha) \frac{\partial \mathcal{G}}{\partial n'} d\Omega', \tag{5-14}$$

where the Green's function is given by

$$\begin{aligned}\mathcal{G}(\mathbf{r},\mathbf{r}') =& 4\pi\lambda\sum_{l=0}^{\infty}\sum_{m=-l}^{l} i_l(\lambda r_<)k_l(\lambda r_>) \\ &\times\left(1-\frac{i_l(\lambda r_>)k_l(\lambda R_\alpha)}{k_l(\lambda r_>)i_l(\lambda R_\alpha)}\right)Y_{lm}^*(\widehat{\mathbf{r}}')Y_{lm}(\widehat{\mathbf{r}}).\end{aligned} \tag{5-15}$$

Its normal derivative at the atomic sphere boundary is expressed as

$$\begin{aligned}\frac{\partial\mathcal{G}}{\partial n'} &= \left.\frac{\partial\mathcal{G}}{\partial r'}\right|_{r'=R_\alpha} \\ &= -\frac{4\pi}{R_\alpha^2}\sum_{l=0}^{\infty}\sum_{m=-l}^{l} Y_{lm}^*(\widehat{\mathbf{r}}')Y_{lm}(\widehat{\mathbf{r}})\frac{i_l(\lambda r)}{i_l(\lambda R_\alpha)},\end{aligned} \tag{5-16}$$

where $k_l(r)$ are the modified spherical Bessel functions of the second kind, and $r_<$ ($r_>$) is the maximum (minimum) value between $\mathbf{r}$ and $\mathbf{r}'$.

The algorithm described in this section does not apply only to the mixing of potentials. For example, instead of the potentials, Eq. 5-2 can also be performed with input and output densities. Also in the case of density mixing, the procedure of solving the screened Poisson equation remains unchanged.

5.1.2 Revised Pulay mixing

As described in Sec. 3.6.2, in the Pulay method, Eq. 3-41 is computed over the whole unit cell, i.e., the interstitial region and muffin-tin spheres. When the generalized-gradient approximation (GGA) is employed, noisy potentials in the interstitial region may be observed, especially in slab calculations with vacuum. This numerical noise has an effect on the calculation of the weights ω_i, and it prevents obtaining the optimal potential in Eq. 3-38. To solve this issue, we replace Eq. 3-41 with

$$A_{ij} = \sum_{\alpha}\int_{\mathrm{MT}_\alpha} R_j^{\mathrm{in}}(\mathbf{r})R_i^{\mathrm{in}}(\mathbf{r})d^3r. \tag{5-17}$$

In other words, we consider only the muffin-tin part of the residuals at this step. This indicates that $R_{\mathrm{opt}}^{\mathrm{in}}$ is minimized within the muffin-tin spheres. The summation of the residual shown in Eq. 3-38 is, nevertheless, carried out over the whole unit cell. Unlike the potential case, a negligible level of noise in the charge density is observed in the interstitial region. Therefore, Eq. 5-17 is not necessary for mixing densities. In this dissertation, Eqs. 3-41 and 5-17 are used for the density and potential mixing. We refer to the method employing this approach as `simple Pulay`.

The Kerker preconditioner, as discussed in Sec. 5.1.1, can also be used in the Pulay method to address charge-sloshing [38, 39, 41, 42]. In this case, the typical

Pulay in Eq. 3-42 transforms into

$$v_{i+1}^{\text{in}}(\mathbf{G}) = v_{\text{opt}}^{\text{in}}(\mathbf{G}) + \alpha \frac{G^2}{G^2 + \lambda^2} R_{\text{opt}}^{\text{in}}(\mathbf{G}). \tag{5-18}$$

This form of the equation is almost consistent with Eq. 5-1 and can be evaluated exploiting the same idea as discussed in Sec. 5.1.1. We apply this preconditioner only in the first n self-consistent field iterations and Eq. 3-42 is thereafter. We employ five iterations ($n = 5$) in our calculations. The convergence behavior of this method depends on the choice of mixing parameters, α and λ. α is set to 0.4 throughout this dissertation. For the screening parameter λ, studies using the Thomas-Fermi screening wavenumber k_{TF} have been reported [147,148]. We evaluate it by following Ref. [148]:

$$k_{TF} \approx \sqrt{4\pi N(\varepsilon_F)}, \tag{5-19}$$

where $N(\varepsilon_F)$ is the density of states at the Fermi energy.

Another approach to suppress charge sloshing is to introduce the inverse Kerker metric in Eq. 3-41 [38, 39]. The inverse Kerker metric is given by

$$A_{ij} = \sum_{\mathbf{G}} R_i^{*,\text{in}}(\mathbf{G}) \frac{G^2 + \lambda'^2}{G^2} R_j^{\text{in}}(\mathbf{G}). \tag{5-20}$$

It was basically designed for the planewave basis. Therefore, applying this metric to the FP-LAPW directly is impractical. We tackle this problem by considering a similar procedure used for the Kerker mixing (see Sec. 4.4.1). $R_j(\mathbf{G})/G^2$ is the Hartree potential when the charge density corresponds to $\rho(\mathbf{r}) = -R_j(\mathbf{G})/4\pi$. Equation 5-20 can be transformed into a real space representation as

$$A_{ij} = \int\int R_i^{\text{in}}(\mathbf{r}) \left(\delta(\mathbf{r} - \mathbf{r}') - \frac{\lambda'^2}{4\pi} \frac{1}{|\mathbf{r} - \mathbf{r}'|} \right) R_j^{\text{in}}(\mathbf{r}') d^3r' d^3r. \tag{5-21}$$

Equation 5-21 corresponds to Eq. 5-20 when integrals are evaluated in the entire unit cell. We consider this metric for the mixing of densities. The modified Pulay method, using the Kerker preconditioner and the inverse Kerker metric, is referred to as `Pulay-KP` in this dissertation.

5.2 Applications of implemented mixing schemes

To evaluate the robustness and efficiency of the implemented mixing methods in the **`exciting`** code [34], we construct a test suite. Metal surfaces are suitable for numerical tests since such metallic systems are prone to charge sloshing (see Sec. 3.6.4). Thus, we consider two metal surfaces as the test samples: (i) the 2×2 Au(111) surface with a vacancy and (ii) the Pd(111) surface. The former contains five layers of Au(111) (termed 5L-(2×2)Au(111)-V), and the latter consists of 15 atomic layers (termed 15L-Pd(111)). Figure **5-1** shows both structures.

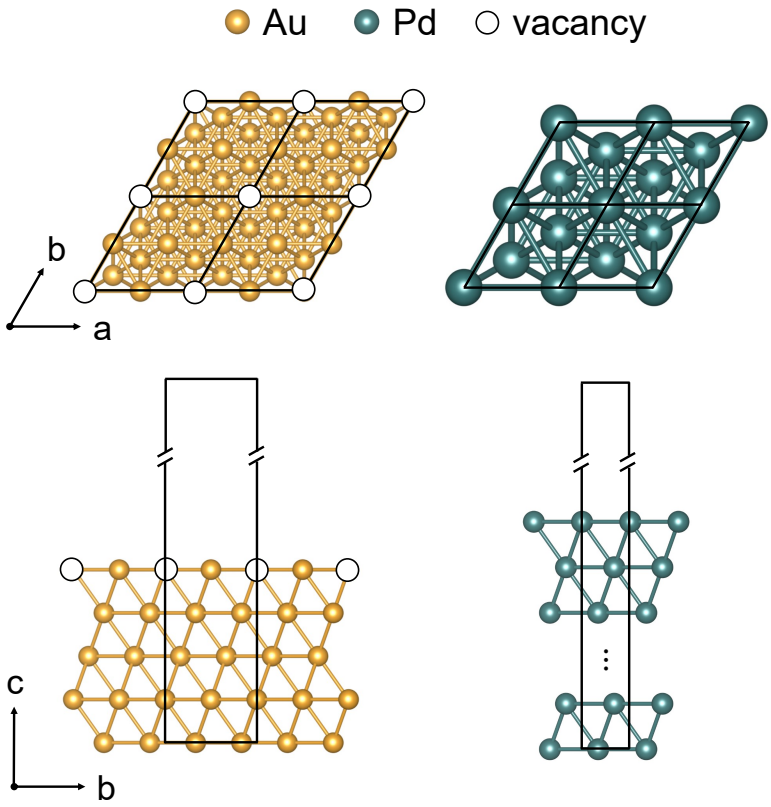

Figure **5-1**: Left: Top view (top) and side view (bottom) of a 2×2 Au(111) surface with a vacancy. Right: Top view (top) and side view (bottom) of a Pd(111) surface with 15 layers. The unit cells are indicated by black lines.

5.2.1 Computational details

To create these slabs, we employ lattice constants of 4.19 Å and 3.95 Å for Au and Pd, respectively. These slabs are not relaxed further. The vacuum spacing along the z direction corresponds to 30 Å and 20 Å for the investigated Au and Pd surfaces, respectively. This choice is made to avoid spurious interactions between replica of the slabs.

The muffin-tin radii are set to $R_{MT}^{Au} = 2.4$ bohr and $R_{MT}^{Pd} = 1.9$ bohr. A value of $R_{MT}G_{max} = 7$ is employed for the LAPW cutoff for both cases. Exchange and correlation effects are approximated by the PBE parameterization [113] of the GGA. For comparison, we also adopt the Perdew-Wang parametrization [105] of the LDA. We employ a planewave cutoff of $G_{max}^{v} = 18$ bohr^{-1} for both benchmark systems. The Brillouin zone (BZ) is sampled with a $4 \times 4 \times 1$ and a $10 \times 10 \times 1$ **k**-grid for 5L-(2×2)Au(111)-V and 15L-Pd(111), respectively. The self-consistent field iterations are performed until the difference of the total energy and residual norm

between two successive iterations is below 10^{-6}. Potentials (densities) and residuals from previous steps (m) are stored for `simple Pulay`, `Pulay-KP`, and a variant of the multisecant Broyden method, which is termed `msec`. In the case of the 5L-(2 × 2)Au(111)-V system, stored potentials and residuals of $m = 12$ are used. Further, $m = 30$ is employed for the 15L-Pd(111) calculations, since large m results in a stable performance.

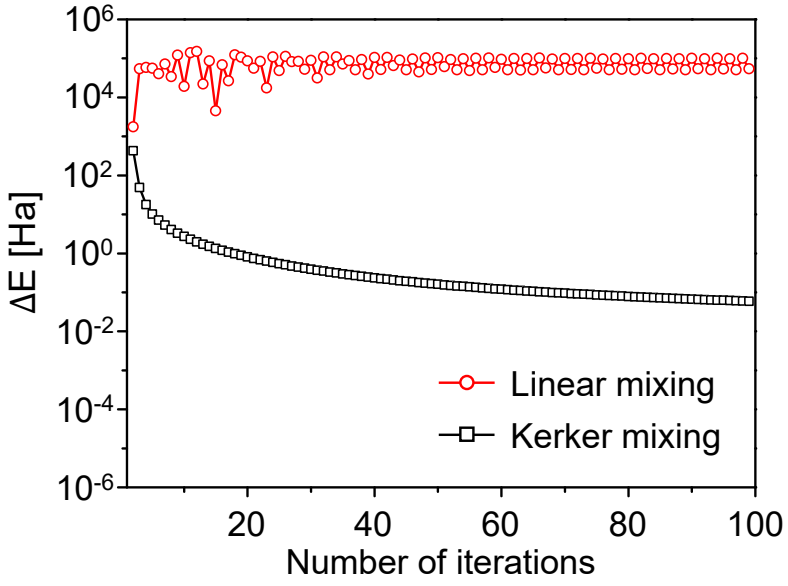

Figure **5-2**: Comparison of total energy (in Ha) convergence of linear and Kerker mixings for 5L-(2 × 2)Au(111)-V.

5.2.2 2×2 Au(111) surface with a vacancy

In this section, we verify the convergence behavior of the implemented mixing algorithms for 5L-(2 × 2)Au(111)-V. First, linear mixing and Kerker mixing are tested with the mixing of potentials. Here, the mixing parameters in Eqs. 3-37 and 5-1 are set to $\alpha = 0.4$ for both methods and $\lambda = 1.0$ bohr $^{-1}$ for the Kerker mixing. The change of the total energy between two successive iterations, ΔE, for these methods is illustrated in Fig. **5-2**. Our result clearly shows that the linear mixing not only does not reach to a required convergence threshold during 100 iterations, but also that this quantity oscillates overall within 10^4 – 10^5 Ha. The huge fluctuation of ΔE is attributed to large changes in the effective Kohn-Sham potential. In the muffin-tin spheres, the potential changes dramatically. This has a significant influence on the radial functions in the LAPW basis set. Due to their nodal structure, large changes of the total energy are caused.

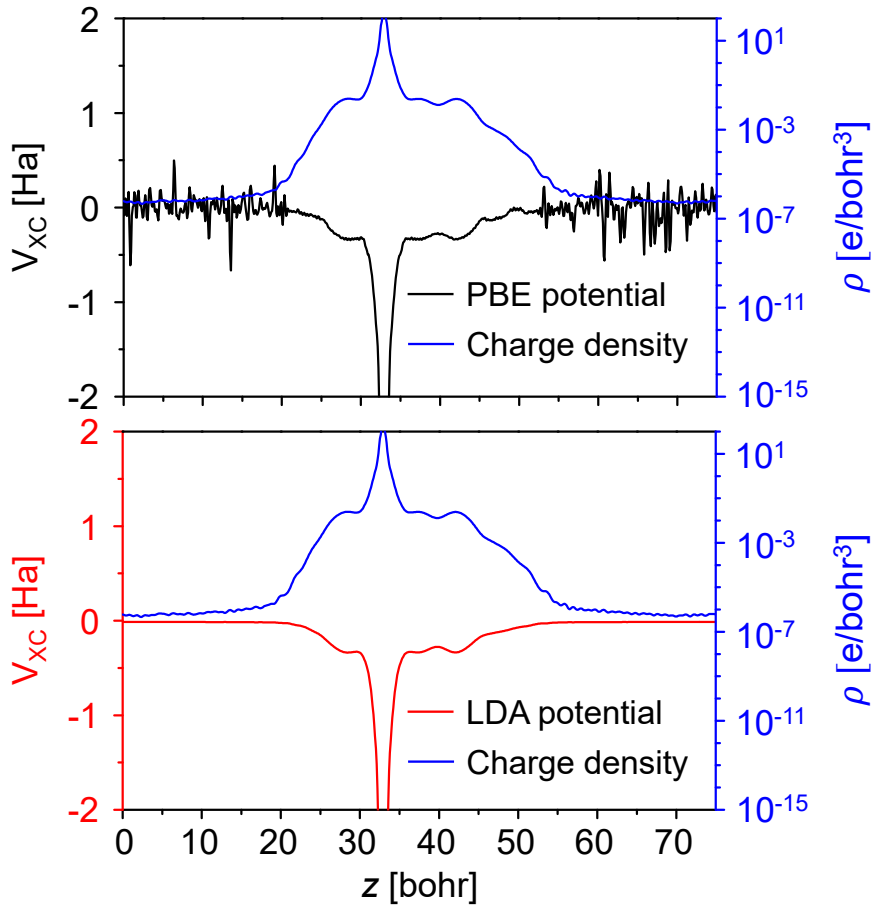

Figure **5-3**: Exchange-correlation potential and corresponding charge density (blue lines) of 5L-(2 × 2)Au(111)-V along the z axis. The exchange-correlation potential from PBE (top) and LDA (bottom) are displayed as black and red lines, respectively.

Compared to the linear mixing, the Kerker mixing achieves rather stable convergence. This implies that the charge sloshing instability is restrained. However, this method is too slow to be practical.

Another problem leading to the slow convergence for 5L-(2 × 2)Au(111)-V is the noisy GGA potential in the vacuum region. To illustrate this, we present the self-consistent exchange-correlation potentials $v_{\mathrm{xc}}(\mathbf{r})$ and the corresponding electron densities of 5L-(2 × 2)Au(111)-V obtained by LDA and GGA in Fig. **5-3**. The densities are similar, whereas the exchange-correlation potentials are significantly different. For the LDA case, an overall smooth potential is observed in the entire unit cell, showing only slight oscillations in the low-charge density region ($\rho < 10^{-4}$ bohr). The noise in the GGA potential is ascribed to the gradient term ($\nabla\rho/\rho^{4/3}$), which tends to cause large changes in the low-charge density region [44]. We perform additional tests with an increased LAPW cutoff of $R_{MT}G_{max} = 8.5$, a planewave cutoff of $G^{v}_{max} = 32$ bohr^{-1}, and a **k**-mesh of 10 × 10 × 1. According to our

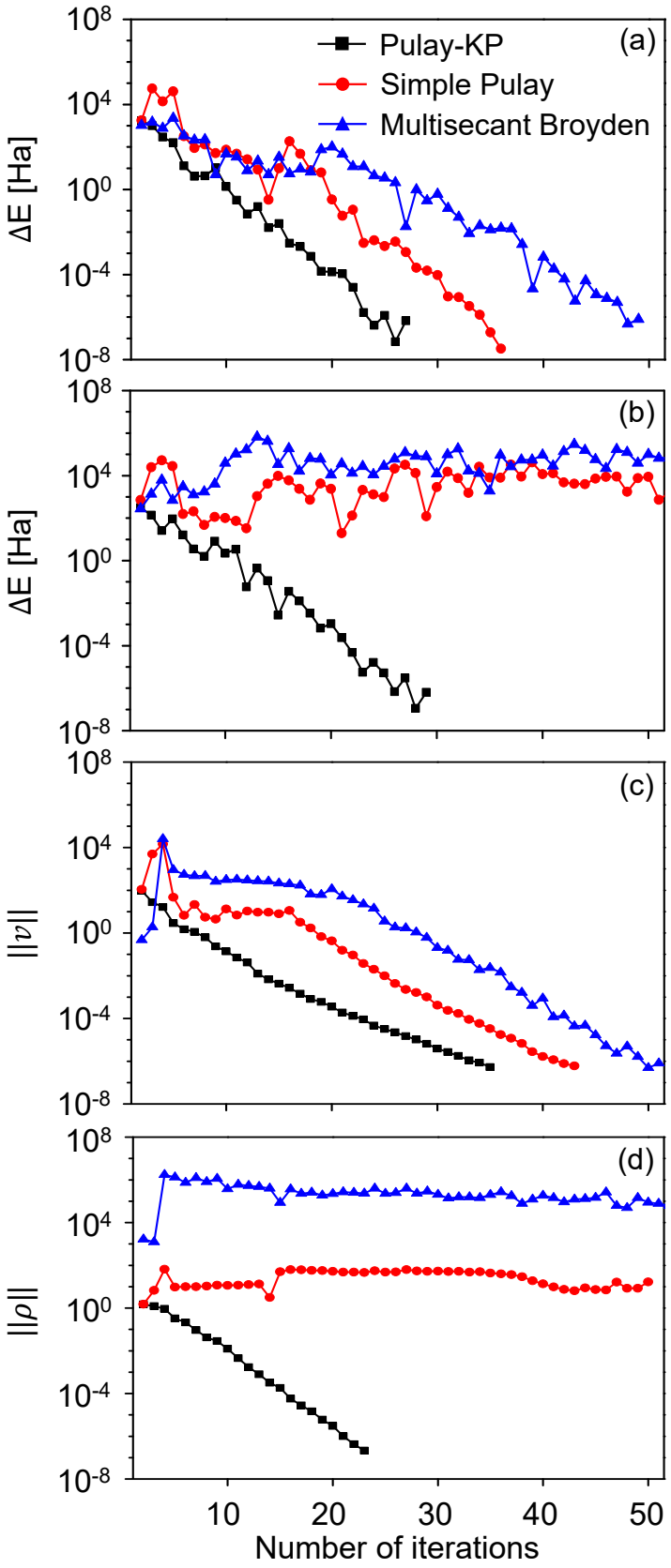

Figure **5-4**: Comparison of total energy ((a) and (b)) and residual norm ((c) and (d)) convergence of the methods `msec`, `simple Pulay`, and `Pulay-KP` for 5L-(2 × 2)Au(111)-V by using potential ((a) and (c)) and density ((b) and (d)) mixing.

numerical tests, the noisy GGA potential remains unchanged. This confirms that GGA calculations of systems in the low-density region, such as slabs with vacuum, show more unstable convergence than the LDA case upon potential mixing.

Our `simple Pulay` and `revised Pulay` methods are less affected by these shortcomings. To prove this, we compare the total energy and residual norm convergence for both schemes and the `msec` scheme with the mixing of potentials (see Figs. **5-4** (a) and (c)). We note that unlike an initial method introduced by Mark and Luke [124], "unpredicted components" for adjusting step size and "scaling" of the potential (or density) between the inside and outside muffin-tin spheres are not included in the `msec` method. We expect that the convergence will become more stable and faster if the `msec` scheme considers these elements. All considered methods reach the total energy tolerance within 25–50 iterations compared to the linear and Kerker mixings discussed in Fig. **5-2**. The convergence of the residual norm with those three methods is slightly slower than that of the total energy. The `simple Pulay` and `Pulay-KP` methods converge faster than the `msec` scheme, which does not handle the noisy potential.

Density mixing can also be applied to this test case. In Fig. **5-4** (b) and (d), we present the convergence behavior of the total energy and the residual norm. We observe that the selected convergence thresholds cannot be achieved within the first 100 iterations for the `simple Pulay` and `msec` methods. On the other hand, the `Pulay-KP` method reaches self-consistency in 36 and 24 steps, respectively. Overall, `Pulay-KP` is robust and outperforms the other considered methods.

5.2.3 Pd(111) surface with 15 atomic layers

To further investigate the convergence, we choose 15L-layer Pd(111) as the second benchmark system. This system is not only metallic with a large unit cell, but also has a high density of states near the Fermi level. Thus, a more pronounced charge-sloshing instability is to be expected [35, 149]. A comparison of the convergence of the total energy and residual norm with three schemes, i.e., `simple Pulay`, `msec`, and `Pulay-KP`, is provided in Fig. **5-5**. Regardless of whether density or potential mixing is considered, only `Pulay-KP` converges in this test case.

The other two methods fail to converge for either type of mixing. In particular, `msec` for the density mixing case cannot finish the self-consistency iterations as it produces an unphysical density. In contrast, `Pulay-KP` requires 35 (density) and 36 (potential) steps to achieve the target energy tolerance, respectively. In addition, the convergence of the residual norm computed by this `Pulay-KP` method is completed in 32 (density) and 38 (potential) iterations. These results imply that the charge-

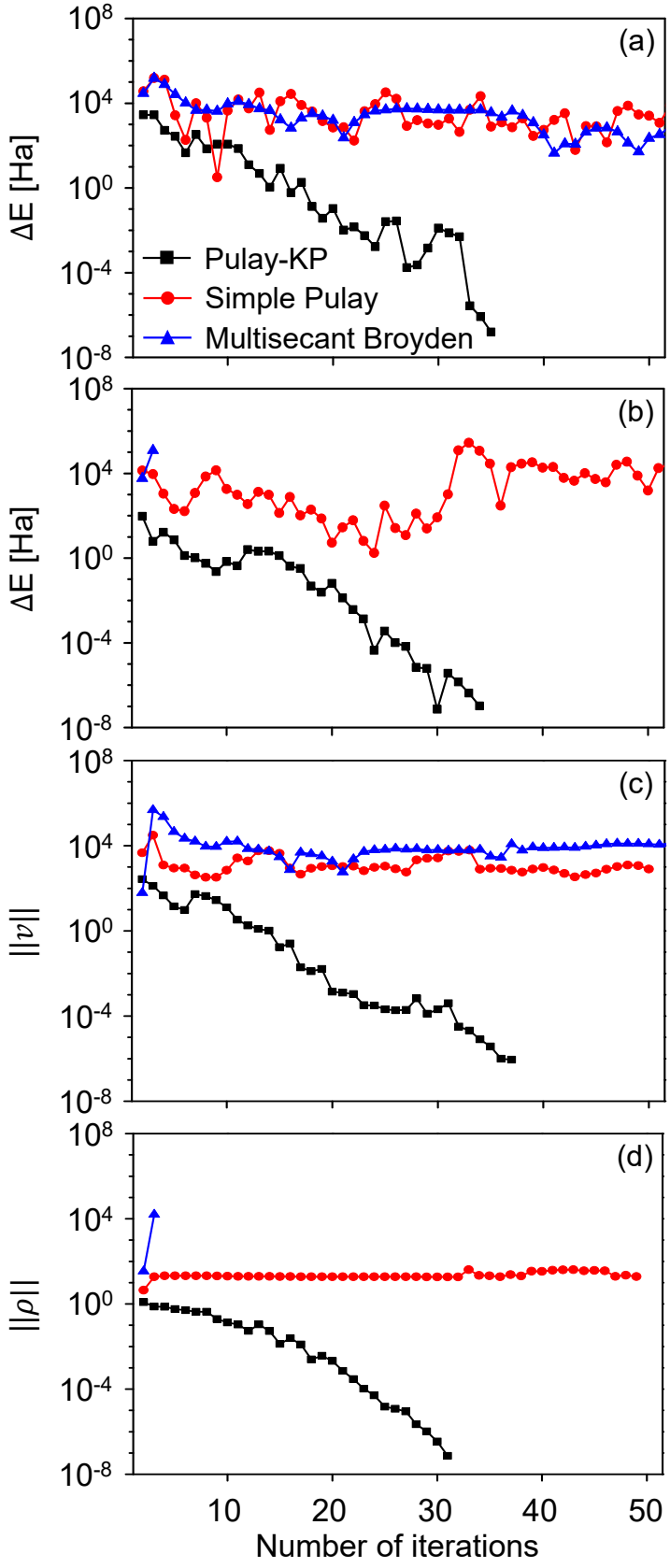

Figure **5-5**: Comparison of total energy ((a) and (b)) and residual norm ((c) and (d)) convergence of the methods `msec`, `simple Pulay`, and `Pulay-KP`for 15L-Pd(111) by using potential ((a) and (c)) and density ((b) and (d)) mixing.

sloshing is well suppressed by reducing long-wavelength variations. As a result, this method significantly improves its efficiency and robustness compared to the `standard Pulay` method and the `msec` method.

5.3 MBD@rsSCS for periodic systems

The MBD@rsSCS scheme incorporates many-body dispersion and screening effects. To prevent double counting of long-range screening effects, a range-separation (rs) approach is introduced in this MBD@rsSCS method [59]. In this regard, the dipole-dipole interaction tensor is separated into short-range and long-range parts. The short-range screening in the MBD@rsSCS is determined by the screened polarizability obtained from the polarizability of free atoms. The screened polarizability can be computed by solving the self-consistent screening (SCS). Finally, the many-body long-range dispersion energy is evaluated using the polarizability and long-range dipole-dipole interaction tensor. The computation of the dispersion energy is outlined in three major steps:

(1) Calculation of the Tkatchenko-Scheffler (TS) atomic polarizability from the polarizability of free atoms

(2) Evaluation of the self-consistently screened polarizability based on the short-range dipole-dipole interaction

(3) Computation of the long-range dispersion energy using the screened polarizability

Unfortunately, the MBD@rsSCS approach was originally designed to be applied only to non-periodic systems, which requires large supercells for calculations. Thus, the MBD@rsSCS method was not suited for periodic systems. To be able to treat them, a reciprocal space implementation of the MBD@rsSCS scheme has been proposed [60]. In this section, we describe the implementation of the MBD@rsSCS for periodic systems in **`exciting`** and test its performance.

5.3.1 TS atomic polarizability

At first, we evaluate the Tkatchenko-Scheffler (TS) atomic polarizability, α^{TS} [57]. As explained in Sec. 3.4.2, it is defined as

$$\alpha_i^{\mathrm{TS}} = \alpha_i^{free} \frac{V_i^{eff}}{V_i^{free}}, \tag{5-22}$$

where α^{free}, $\frac{V^{eff}}{V^{free}}$ are the polarizability of the free atom and the ratio between the effective volume of an atom in a molecule and the volume of the free atom, respectively. The atomic volume is obtained from the Hirshfeld partitioning as

follows [116]:

$$\frac{V_i^{eff}}{V_i^{free}} = \frac{\int r^3 w_i(\mathbf{r})\rho(\mathbf{r})d\mathbf{r}^3}{\int r^3 \rho_i^{free}(\mathbf{r})d\mathbf{r}^3}. \tag{5-23}$$

Here, $\rho(\mathbf{r})$ is the charge density of a system and $\rho_i^{free}(\mathbf{r})$ is the electron density of the neutral free atom i. The Hirshfeld weight $w(\mathbf{r})$ is determined as

$$w_i(\mathbf{r}) = \frac{\rho_i^{free}(\mathbf{r})}{\sum_j \rho_j^{free}(\mathbf{r})}. \tag{5-24}$$

Another useful atomic parameter for the MBD@rSCS is the rescaled van der Waals radius, given by

$$R_{\mathrm{vdW},i} = R_i^{free}\left(\frac{V_i^{eff}}{V_i^{free}}\right)^{1/3}, \tag{5-25}$$

where R^{free} indicates the free-atom vdW radius.

5.3.2 Self-consistently screened polarizability

According to the range-separation method [59, 60], the self-consistently screened polarizability, $\tilde{\boldsymbol{\alpha}}^{\mathrm{SCS}}$, is calculated by employing the short-range part of the dipole-dipole interaction, $\mathbf{T}_{SR}$, as follows:

$$\tilde{\boldsymbol{\alpha}}^{\mathrm{SCS}}(\omega) = \alpha^{\mathrm{TS}}(\omega)\left(\mathbf{1} - \mathbf{T}_{SR}(\omega)\tilde{\boldsymbol{\alpha}}^{\mathrm{SCS}}(\omega)\right), \tag{5-26}$$

where $\alpha^{\mathrm{TS}}(\omega)$ is the frequency dependent polarizability:

$$\alpha_i^{\mathrm{TS}}(\omega) = \frac{\alpha_i^{\mathrm{TS}}}{1 + (\omega/\omega_i)^2}. \tag{5-27}$$

The characteristic frequency ω of an atom i in Eq. 5-27, is written as

$$\omega_i = \frac{4}{3}\frac{C_{6,free}^{ii}}{(\alpha_i^{free})^2} \tag{5-28}$$

where $C_{6,free}^{ii}$ is the free-atom dispersion coefficient.

In the next step, we define the short-range dipole-dipole interaction tensor in Eq. 5-26 as

$$\mathbf{T}_{SR,ij}^{ab}(\omega) = \sum_{\boldsymbol{L}}{}'(1 - f(S_{\mathrm{vdW},ij}, r_{ij,\boldsymbol{L}}))\partial r_{i,\boldsymbol{L}}^a \partial r_{j,\boldsymbol{L}}^b \left[\frac{\mathrm{erf}(r_{ij,\boldsymbol{L}}/\sigma_{ij}(\omega)}{r_{ij,\boldsymbol{L}}}\right]. \tag{5-29}$$

Here, $\boldsymbol{L}$ are all translations of a unit cell, and r_{ij} is a distance between atoms i and j. a and b represent the Cartesian components of r_{ij}. σ_i is the Gaussian function's width of atom i in the following manner:

$$\sigma_i(\omega) = \left(\sqrt{\frac{2}{\pi}}\frac{\alpha_i^{\mathrm{TS}}(\omega)}{3}\right)^{1/3}. \tag{5-30}$$

The effective correlation length between atoms i and j is defined as $\sigma_{ij}(\omega) = \sqrt{\sigma_i(\omega) + \sigma_j(\omega)}$. The summation in Eq. 5-29 is performed until $r_{ij,\boldsymbol{L}}$ is smaller than a defined cutoff distance, R_{cut}. Following Ref. [60], we use a value of $R_{cut} =$ 120 Å that causes negligible change in the dispersion energies compared to larger R_{cut} values. One considers a Fermi-type damping function to reduce interactions when distances between atoms are too small:

$$f(S_{\mathrm{vdW},ij}, r_{ij,\boldsymbol{L}}) = \frac{1}{1 + \exp[-d(r_{ij,\boldsymbol{L}}/S_{\mathrm{vdW},ij} - 1)]}, \tag{5-31}$$

with d being a parameter, which we fix to 6. S_{vdW} corresponds to the sum of van der Waals radii of atoms i and j, R_{vdW}, with another parameter β, i.e., $S_{\mathrm{vdW}} = \beta(R_{\mathrm{vdW},i} + R_{\mathrm{vdW},j})$. β has been optimized with a value of 0.83 for the PBE functional [59].

The solution of Eq. 5-26 can be obtained by partial contraction of the screened non-local polarizability matrix, as suggested in Refs. [60, 61, 150]:

$$\tilde{\boldsymbol{\alpha}}_i^{\mathrm{SCS}}(\omega) = \sum_{j=1}^{N} \tilde{\mathbf{A}}_{ij}(\omega), \tag{5-32}$$

where $\tilde{\mathbf{A}}_{ij}$ is given by

$$\tilde{\mathbf{A}}_{ij}(\omega) = \left[\frac{1}{\alpha_i^{\mathrm{TS}}(\omega)} \delta_{ij}\delta_{ab} + \mathbf{T}_{SR,ij}^{ab}(\omega) \right]^{-1}. \tag{5-33}$$

$\tilde{\boldsymbol{\alpha}}^{\mathrm{SCS}}$ is used for calculating the long-range dispersion energy.

5.3.3 Long-range dispersion energy

The adiabatic connection fluctuation-dissipation (ACFD) theorem provides the exact correlation energy [151] that reads

$$E_c = -\frac{1}{2\pi} \int_0^\infty d\omega \int_0^1 d\lambda \mathrm{Tr}[(\chi_\lambda v - \chi_0 v)], \tag{5-34}$$

where $\chi_\lambda(\mathbf{r}, \mathbf{r}', \mathrm{i}\omega)$ and $\chi_0(\mathbf{r}, \mathbf{r}', \mathrm{i}\omega)$ indicate the response function of an interacting system and the bare response function obtained from Kohn–Sham orbitals, respectively. $v(\mathbf{r}, \mathbf{r}') = 1/|\mathbf{r} - \mathbf{r}'|$ is the Coulomb potential and λ is the coupling strength. χ_λ is commonly approximated using the random-phase approximation (RPA). In the RPA, the interacting response function χ_λ^{RPA} can be described via the self-consistent Dyson equation: $\chi_\lambda^{RPA} = \chi_0 + \chi_0 \lambda v \chi_\lambda^{RPA}$. Employing the Dyson equation and integrating over λ in Eq. 5-34, the correlation energy in RPA is written as [152]

$$E_c = -\frac{1}{2\pi} \int_0^\infty d\omega \sum_{n=2}^{\infty} \frac{1}{n} \mathrm{Tr}[(\chi_0 v)^n]. \tag{5-35}$$

One can substitute χ_0, which has a high computational cost, with the atomic response functions based on quantum harmonic oscillators. With this replacement, the long-range dispersion energy for periodic systems can be expressed as follows [60]:

$$E_{disp} = -\sum_{\boldsymbol{k}} w_{\boldsymbol{k}} \int_0^\infty \frac{d\omega}{2\pi} \mathrm{Tr}\{\ln(\mathbf{1} - \mathbf{A}_{LR}(\omega)\mathbf{T}_{LR}(\boldsymbol{k}))\}, \tag{5-36}$$

where $w_{\boldsymbol{k}}$ denotes the weighting factor of $\boldsymbol{k}$-points. We construct $\mathbf{A}_{LR}$ using the screened isotropic polarizability $\tilde{\alpha}^{\mathrm{SCS,iso}}$:

$$A^{ab}_{LR,ij}(\omega) = \tilde{\alpha}^{\mathrm{SCS,iso}}_i(\omega)\delta_{ij}\delta_{ab}, \tag{5-37}$$

where $\tilde{\alpha}^{\mathrm{SCS,iso}}$ corresponds to one-third of the trace of the screened polarizability in Eq 5-32. It then becomes

$$\tilde{\alpha}^{\mathrm{SCS,iso}}_i = \frac{1}{3}\mathrm{Tr}\left[\tilde{\boldsymbol{\alpha}}^{\mathrm{SCS}}_i(\omega)\right]. \tag{5-38}$$

$\mathbf{T}_{LR}$ in Eq. 5-36 is the long-range dipole-dipole interaction tensor that includes the damping function $f(\tilde{S}_{\mathrm{vdW},ij}, r_{ij,\boldsymbol{L}})$ and the full-range second-order interaction tensor. The tensor is given by

$$\mathbf{T}^{ab}_{LR,ij}(\boldsymbol{k}) = {\sum_{\boldsymbol{L}}}' f(\tilde{S}_{\mathrm{vdW},ij}, r_{ij,\boldsymbol{L}})\mathbf{T}^{ab}_{ij,\boldsymbol{L}} \cdot \mathrm{e}^{-\mathrm{i}\boldsymbol{k}\cdot\boldsymbol{L}}, \tag{5-39}$$

with

$$\mathbf{T}^{ab}_{ij} = \frac{3r^a_{ij}r^b_{ij} - \delta_{ab}r^2_{ij}}{r^5_{ij}}. \tag{5-40}$$

Similar to S_{vdW} discussed in Sec. 5.3.2, $\tilde{S}_{\mathrm{vdW}}$ is defined as

$$\tilde{S}_{\mathrm{vdW}} = \beta(\tilde{R}_{\mathrm{vdW},i} + \tilde{R}_{\mathrm{vdW},j}). \tag{5-41}$$

The van der Waals radii of the screened atoms $\tilde{R}_{\mathrm{vdW}}$ is determined by

$$\tilde{R}_{\mathrm{vdW},i} = R_{\mathrm{vdW},i}\left(\frac{\tilde{\alpha}^{\mathrm{SCS,iso}}_i}{\alpha^{\mathrm{TS}}_i}\right)^{1/3}. \tag{5-42}$$

It should be stressed that the dispersion energy depends on the number of $\boldsymbol{k}$-points. Therefore, convergence tests of the dispersion energy with respect to the number of $\boldsymbol{k}$-points are necessary.

To compute interatomic forces for structure optimizations, we consider the dispersion-energy gradient:

$$\mathbf{F}_{disp} = \sum_{\boldsymbol{k}} w_{\boldsymbol{k}} \int_0^\infty \frac{d\omega}{2\pi} \mathrm{Tr}\{[\mathbf{1} - \mathbf{A}_{LR}(\omega)\mathbf{T}_{LR}(\boldsymbol{k})]^{-1}\nabla[\mathbf{A}_{LR}(\omega)\mathbf{T}_{LR}(\boldsymbol{k})]\}. \tag{5-43}$$

In Appendix A, a detailed expression of the interatomic forces is given.

5.4 Application of the MBD@rsSCS

We demonstrate the performance of our implementation of the MBD@rsSCS in **exciting** for layered materials where van der Waals interactions are essential. We consider three test cases: (i) graphite, (ii) hexagonal boron nitride (h-BN), and (iii) graphite fluoride.

5.4.1 Computational details

The experimental in-plane lattice parameters of $a = 2.46$ Å [153] and 2.50 Å [154] are taken for graphite and h-BN calculations, respectively. In the case of graphite fluoride, following Ref. [155], a value of $a = 2.582$ Å is used. The muffin-tin radii for atomic spheres are set to $R^C_{MT} = 1.2$ bohr, $R^B_{MT} = 1.2$ bohr, $R^N_{MT} = 1.2$ bohr, and $R^F_{MT} = 1.1$ bohr. A value of $R_{MT}G_{max} = 8$ is used and the Brillioun zone (BZ) sampling is carried out with a $16 \times 16 \times 8$ **k**-point mesh for all cases. All calculations are performed using the Perdew-Berke-Ernzerhof (PBE) functional for the semi-local part of xc effects.

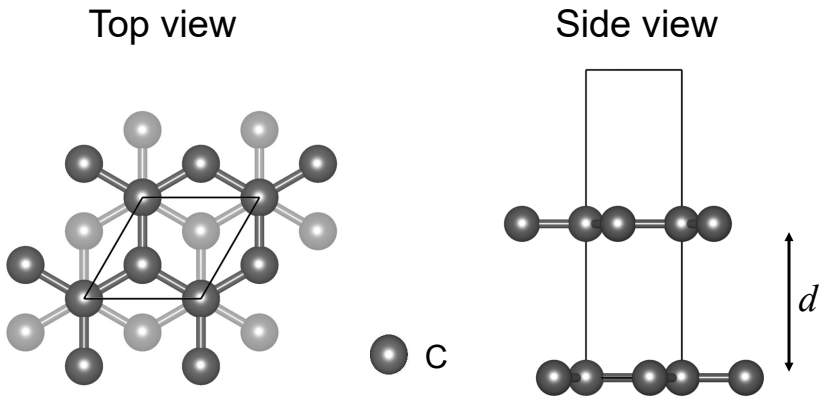

Figure **5-6**: Top view (left) and side view (right) of graphite. The black line represents the unit cells. d is the interlayer distance.

5.4.2 Graphite

The structure of graphite is displayed in Fig. **5-6**. The optimized interlayer distance d_{opt} and binding energy E_b with various vdW corrected methods and experimental values are listed in Table **5-1**. Our implemented MBD@rsSCS provides values of $E_b = 49$ meV/atom and $d_{opt} = 3.42$ Å which are very close to other theoretical results

Table **5-1**: Optimized interlayer distance d_{opt} and binding energy E_b for graphite.

Property	Method	**exciting**	Theory	Experiment
d_{opt}	PBE	4.40	4.42 [157]	3.354 [153]
(Å)	DFT-D2	3.22	3.23 [157, 158]	
	TS	3.33	3.33 [158], 3.34 [159]	
	vdW-DF	3.61 [156]	-	
	MBD@rsSCS	3.42	3.41 [60]	
E_{b}	PBE	1	1 [157]	52±5 [160]
(meV/atom)	DFT-D2	57	57 [157], 57 [158]	
	TS	83	82 [157], 85 [158]	
	vdW-DF	51 [156]	-	
	MBD@rsSCS	49	48 [60]	

computed with MBD@rsSCS [60]. The calculated results agree with experimental values although d_{opt} is slightly overestimated. In previous theoretical studies, DFT-D2 [55] provides a reasonable E_b, whereas d_{opt} is slightly underestimated. The TS approach [57] yields the closest d_{opt} to the experimental value among considered methods, but it largely overestimates E_b. On the other hand, vdW-DF yields a reasonable value of E_b but d_{opt} is rather far from the experimental value. The MBD@rsSCS method gives slightly larger d_{opt}, but it is better than the DFT-D2 and vdW-DF methods. We note that the vdW correction, in which both values of E_b and d_{opt} are close to the experiment, is only the MBD@rsSCS method. Overall, our results demonstrate this MBD@rsSCS approach is the most reliable among those considered for the graphite system.

5.4.3 Hexagonal boron nitride

We investigate hexagonal boron nitride (h-BN) as our second example. h-BN has a layered structure like graphite. However, there are noticeable differences in the electronic properties and stacking patterns between h-BN and graphite. For example, graphite is a semimetal whereas h-BN is an insulator with a large band gap. Moreover, while an AB stacking sequence is found for graphite, h-BN exhibits an AA' stacking where boron atoms are bound to nitrogen atoms in adjacent layers. Figure **5-7** illustrates the h-BN structure. The computational and experimental data of E_b and d_{opt} are shown in Table **5-2**. An experimental value of E_b has yet to be reported. All methods overestimate E_b in comparison with the RPA scheme (39 meV/atom) [162, 163]. Comparing d_{opt} among different vdW correction methods,

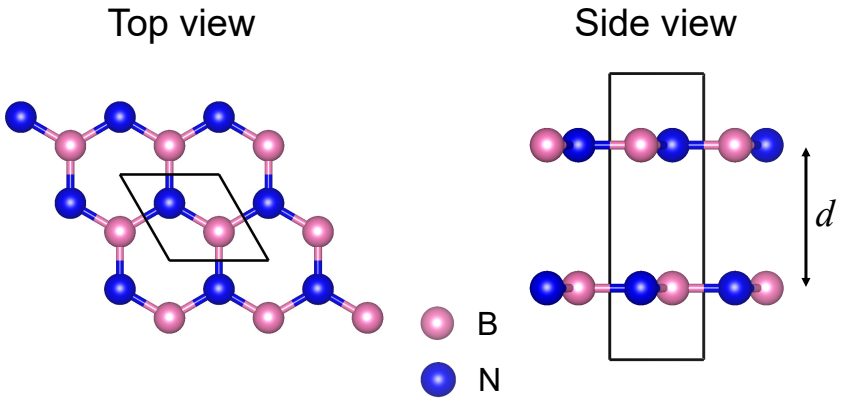

Figure **5-7**: Top view (left) and side view (right) of h-BN. The black line represents the unit cells. d is the interlayer distance.

DFT-D2 shows a small value, while vdW-DF yields a comparably large d_{opt}. This trend is the same as in the graphite case (see Sec. 5.4.2). Here, d_{opt} obtained by MBD@rsSCS coincides well with the experimental value compared to other methods. This further indicates that this MBD@rsSCS represents an improvement over the pairwise-additive model.

Table **5-2**: Optimized interlayer distance d_{opt} and binding energy E_b for h-BN.

Property	Method	**exciting**	Theory	Experiment
d_{opt}	PBE	4.29	-	3.331 [154, 161]
(Å)	DFT-D2	3.09	3.09 [157]	
	TS	3.31	3.32 [159]	
	vdW-DF	3.58 [156]	-	
	MBD@rsSCS	3.32	3.30 [60]	
E_{b}	PBE	2	-	-
(meV/atom)	DFT-D2	77	77 [157]	
	TS	85	87 [159]	
	vdW-DF	51 [156]	-	
	MBD@rsSCS	62	59 [60]	

5.4.4 Graphite fluoride

Graphite fluoride is a derivative of graphite where covalent bonds between carbon and fluorine atoms are formed [164]. Experimental and theoretical studies have

shown that its most stable conformation consists of chair-type cyclohexane rings with an AA stacking sequence [155, 165]. Four atoms are contained in the unit cell, and we display the AA stacked graphite fluoride in Fig. **5-8**. Our MBD@rsSCS approach yields the optimal interlayer separation of $d_{opt} = 5.91$ Å as well as a binding energy of $E_b = 25$ meV/fu. These values are the same as those computed with the same method implemented in the Vienna ab initio simulation package (VASP) [166]. We compare the values with those of the RPA reference [155, 166]: $d_{opt} = 5.88$ Å and $E_b = 35$ meV/fu. E_b and d_{opt} obtained by the MBD@rsSCS are reasonably close to that from the RPA.

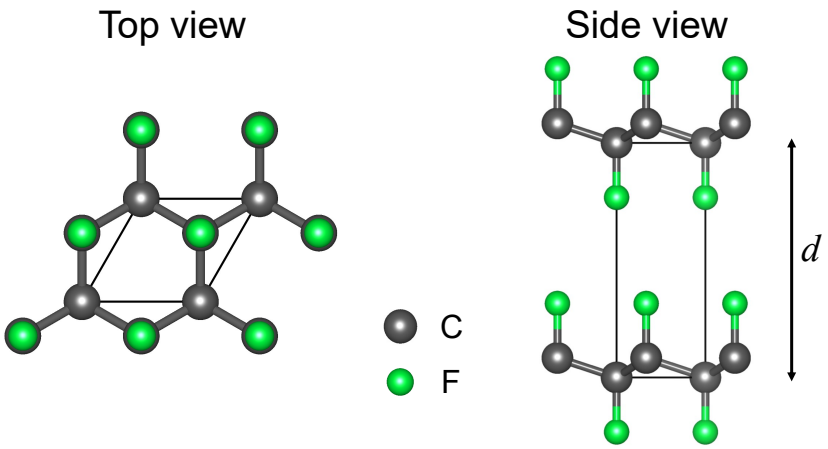

Figure **5-8**: Top view (left) and side view (right) of graphite fluoride. The black line represents the unit cells. d is the interlayer distance. Gray- and green-colored balls denote carbon and fluorine atoms, respectively.

6. Organic/metal interfaces

In this chapter, we discuss the results of a calculation on dithiol terminated PEG (PEG(thiol)) on two metallic surfaces, Au(111) and Ag(111), and investigate how the molecule affects their work functions. The impact of the PEG molecular length and the molecular arrangement on the work-function change is also studied.

6.1 Polyethylene glycol derivatives

Polyethylene glycol (PEG) has been generally used for a variety of applications, especially in the pharmaceutical field [167]. PEG is chemically inert due to its hydrophilic properties. Moreover, it is a non-toxic and safe material [168]. Due to these properties, PEG-based derivatives can enhance water-solubility and stability of nanoparticles by modulating their surfaces [169–171]. In recent years, some of these derivatives have been used for organic electronics devices [21–27,172]. These experimental studies have revealed that interlayers consisting of these derivatives are spontaneously formed between organic semiconductors and metal surfaces like Ag, Al, and Au. The performance of devices is improved by PEG-based interlayers that tune the work function at the interface [22, 25, 27]. Such PEG additives have higher surface energy, e.g., $\sim$ 43 mJ/m^2 for PEG [173] compared to that of organic materials, e.g., $\sim$ 33 mJ/m^2 for diketopyrrolopyrrole thieno[3,2-b] thiophene D–A copolymer (DPP-T-TT) [25], $\sim$ 26 mJ/m^2 for poly(9,9-dioctylfluorene-alt-benzothiadiazole) (F8BT) [174], $\sim$ 27 mJ/m^2 for poly(3-hexylthiophene-2,5-diyl) (P3HT) [175], and $\sim$ 38 mJ/m^2 for phenyl C61-butyric acid methyl ester (PCBM) [173]. When fabricating devices, the derivatives are accumulated at the bottom of a metal/organic interface and do not move to the organic/air interface [176].

All PEG derivatives have polar O–C bonds in their backbones. The difference among these derivatives is their end groups. We note that the end groups of such derivatives do not always have an affinity to metal surfaces [21]. For example, PEG(alcohol) and PEG(acetate) do not form an interlayer at a Au/organic interface, whereas PEG(thiol) interacts with a Au surface. In this chapter, we examine the

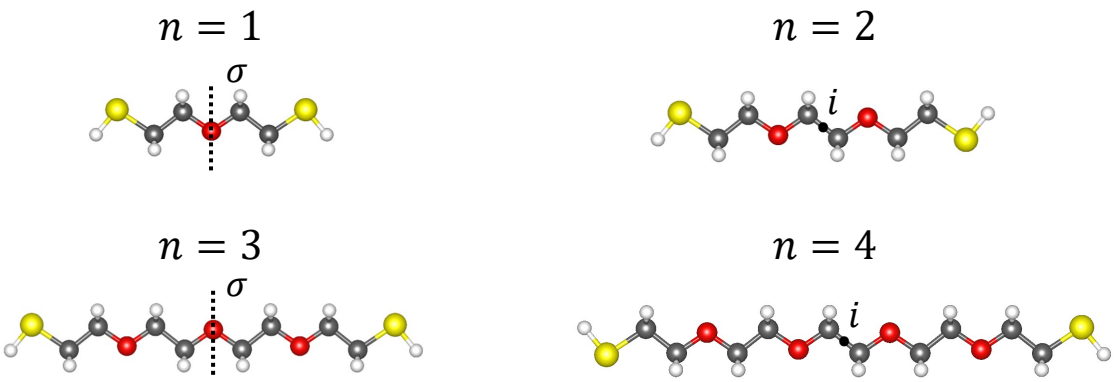

Figure **6-1**: Chemical structure of PEG(thiol) with $n = 1$–4. σ and i indicate the mirror plane and the inversion center, respectively.

PEG(thiol), which has the highest affinity with a Au surface among these PEG derivatives. We also adopt $n = 1$–4 repeat units in the backbone. All considered PEG(thiol) molecules are illustrated in Fig. **6-1**. The molecules with odd n have a vertical mirror plane while an inversion center is found for even n.

Regarding the electronic properties, we depict the molecular orbitals, HOMO and LUMO, of PEG(thiol) with $n = 1$ in Fig. **6-2**. The electron distribution of the HOMO is localized at the S atoms and shows a non-bonding state of p orbitals. A non-bonding state of p orbitals is also observed for the O atom. In addition, sp hybridization is formed between C atoms and adjacent H atoms. The LUMO is distributed along the molecular backbone.

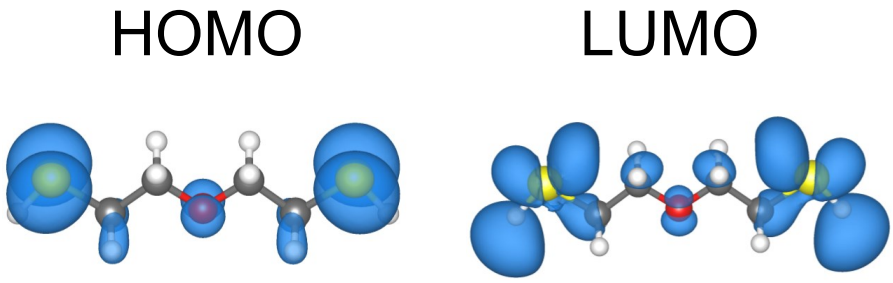

Figure **6-2**: Frontier molecular orbitals, HOMO and LUMO, of PEG(thiol) with $n = 1$.

6.2 PEG(thiol) adsorbed on Au(111)

6.2.1 Computational details

First, we describe the PEG(thiol) molecules adsorbed on Au(111) with various numbers of repeat units of the PEG chain (n = 1–4) [n-PEG(thiol)@Au(111)]. In Fig. **6-3**, we display this structure. Typically, the molecular packing density on the surface has a great influence on the adsorption geometry. At high-coverage, an ordered self-assembled monolayer (SAM) of PEG(thiol) molecules can be formed due to van der Waals interactions [29]. In this chapter, the high-coverage limit is considered. According to scanning tunneling microscopy (STM) and grazing incidence X-ray diffraction (GIXD) experiments, a mixture of the $(\sqrt{3} \times \sqrt{3})R30°$ structure and its related c(4×2) overlayer is observed for thiolate deposited on Au(111) [177, 178]. The relative ratio of these structures is varied by temperature and the length of the molecular chain [178]. For long molecules, the relative proportion of the $(\sqrt{3} \times \sqrt{3})R30°$ structure is larger than the other. We therefore employ the $(\sqrt{3} \times \sqrt{3})R30°$ surface unit cell. Since a study of thioaromatic monolayers deposited on the Au(111) system has revealed that those molecules are arranged in a herringbone structure [179], we also adopt a $p(\sqrt{3} \times 3)$ unit cell that hosts two molecules. The molecular coverage in this unit cell is identical to that in the $(\sqrt{3} \times \sqrt{3})R30°$ case. In the bottom panel of Fig. **6-3**, the $p(\sqrt{3} \times 3)$ structure is depicted with the molecules arranged in a herringbone-like pattern.

To model the Au(111) surface, a repeated-slab containing four atomic layers is used in our calculations. We construct the slab with a lattice constant of 4.192 Å. The two bottom layers are not relaxed. The structural optimization of the two top layers and the PEG molecules is terminated when the maximum force on each atom is below 0.055 eV/Å. To prevent interactions between the periodic images, a vacuum space of at least 14 Å is used.

The DFT calculations are carried out using the **exciting** code. We set $R_{MT}^{Au} = 2.1$ bohr, $R_{MT}^{S} = 1.6$ bohr, $R_{MT}^{O} = 1.1$ bohr, $R_{MT}^{C} = 1.1$ bohr, and $R_{MT}^{H} = 0.7$ bohr for the muffin-tin radii, respectively. For the smallest muffin-tin sphere, a value of $R_{MT}G_{max} = 3$ is adopted. This value corresponds to 4.29 bohr^{-1} of the planewave cutoff G_{max} in the interstitial region. The sampling of the Brillouin zone (BZ) is performed with a $5 \times 5 \times 1$ and a $5 \times 3 \times 1$ **k**-point grid for the $(\sqrt{3}\times\sqrt{3})R30°$ and $p(\sqrt{3}\times 3)$ overlayer structures, respectively. A total-energy convergence criterion of 10^{-6} Ha is used for the self-consistent field cycles. We employ the GGA in the PBE parameterization [113] to describe the semi-local part of exchange and correlation

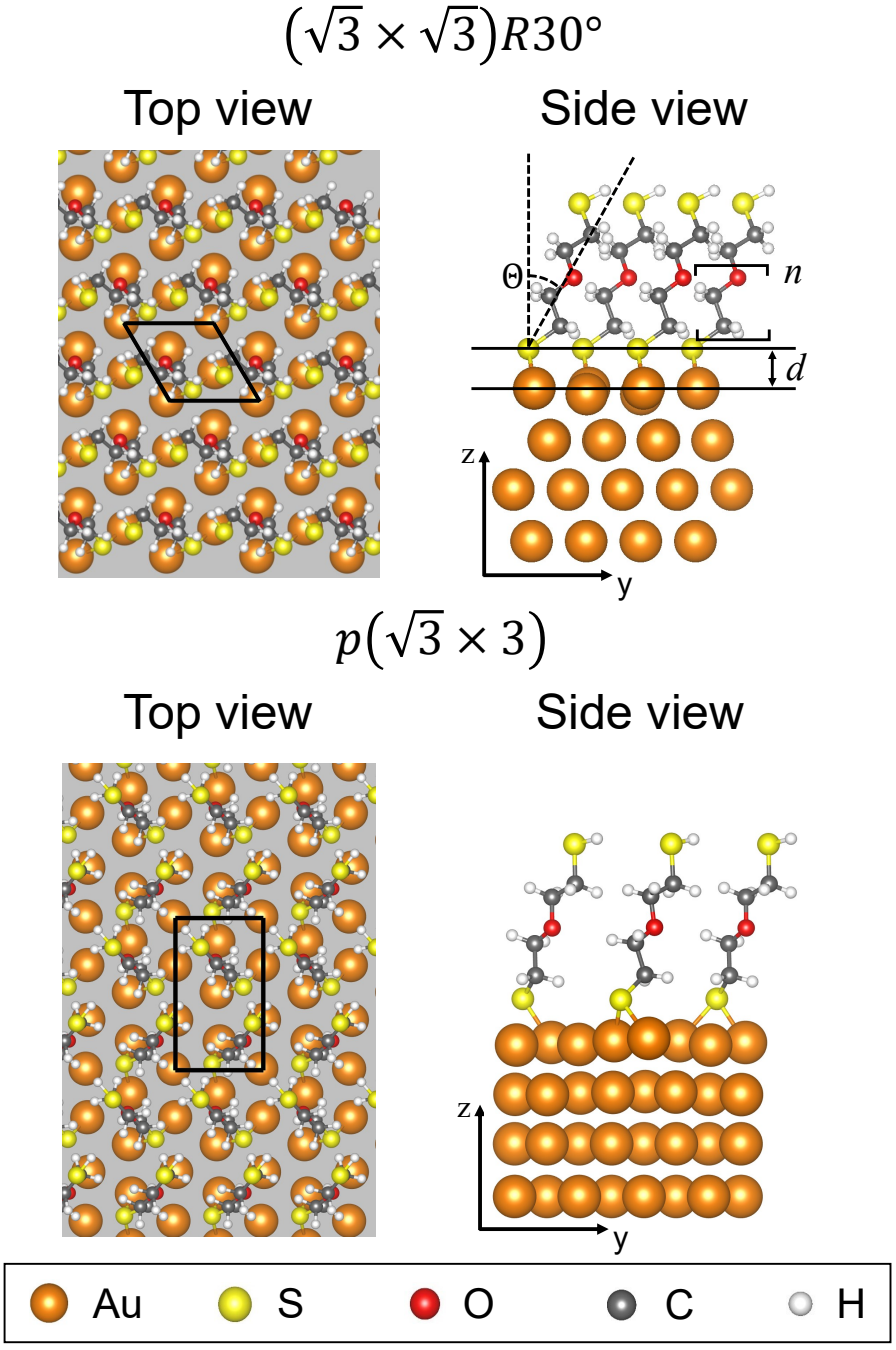

Figure **6-3**: Top view and side view of the PEG(thiol) molecules adsorbed on the Au(111) in $(\sqrt{3} \times \sqrt{3})R30°$ (middle) and $p(\sqrt{3} \times 3)$ (bottom) surface unit cells. θ is the tilting angle between the PEG backbone and the surface normal. d indicates the height from the S atom to the average position of the Au surface atoms.

effects. To consider long-range correlation effects, we employ the DFT-D2 as well as the many-body dispersion (MBD@rsSCS) methods. The implemented `Pulay-KP` mixer, which is described in Sec. 5.1, is adopted, and we discuss the convergence of this method in Appendix B. In all investigated systems, the `Pulay-KP` method requires 30 iterations to achieve self-consistency, regardless of n.

6.2.2 Adsorption geometry

Table **6-1** lists the structural properties of the optimized PEG(thiol)@Au(111) structures with different numbers of PEG repeat units. The chemically bound S atoms are slightly shifted from the hollow site toward the bridge site after structural relaxation, as illustrated by the top views of Fig. **6-3**. This agrees with various theoretical studies of thiolate adsorbed on Au(111) [180–182]. In the $(\sqrt{3}\times\sqrt{3})R30°$ case, the tilting angle θ between PEG(thiol) molecules and the surface normal is 29.5 – 31.9° depending on the length of the PEG backbone. Similar values have been reported in the case of n-alkanethiols on a Au surface [183, 184]. The two PEG(thiol) molecules are tilted by 33.3° and 33.6°, i.e., 33.5° on average in the $p(\sqrt{3}\times 3)$ structure. We observe 1.93 – 1.95 Å of adsorption heights d between the S atom and the average position of the topmost surface atoms with different numbers of repeat units for the $(\sqrt{3}\times\sqrt{3})R30°$ structure. The corresponding values in the $p(\sqrt{3}\times 3)$ pattern are 1.98 Å and 1.94 Å , i.e., an average value of 1.96 Å. Similar θ and d results are obtained in both overlayer patterns. Nevertheless, less curved molecules in the $p(\sqrt{3}\times 3)$ pattern are found in comparison with the $(\sqrt{3}\times\sqrt{3})R30°$ case, thus, the molecules in the $p(\sqrt{3}\times 3)$ pattern have an upright conformation.

Table **6-1**: Adsorption geometry of PEG(thiol) molecules adsorbed on the Au(111) surface using the MBD@rsSCS and the DFT-D2 for van der Waals corrections on top of the PBE.

Repeat units	MBD@rsSCS		DFT-D2	
n	θ [°]	d [Å]	θ [°]	d[Å]
	$(\sqrt{3}\times\sqrt{3})R30°$			
1	31.9	1.94	35.3	1.92
2	29.5	1.95	32.0	1.93
3	31.3	1.94	32.3	1.92
4	30.7	1.93	30.7	1.92
	$p(\sqrt{3}\times 3)$			
1	33.5	1.96	-	-

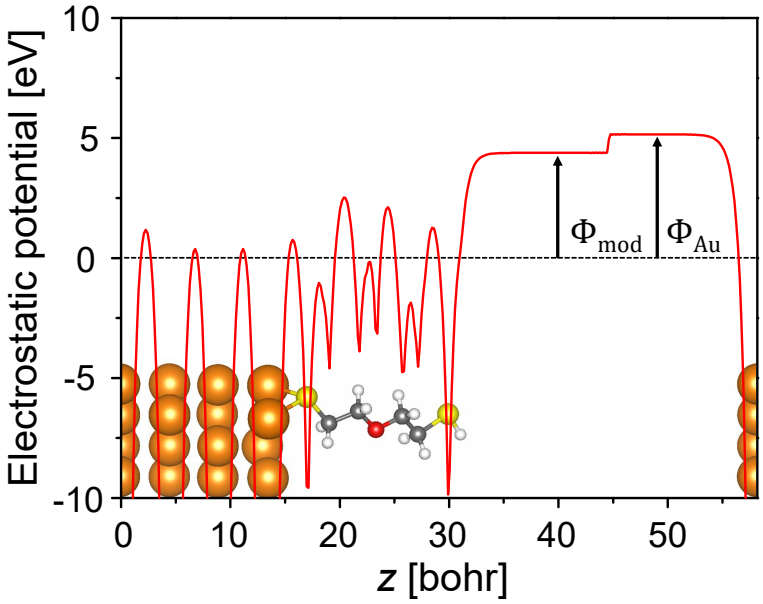

Figure **6-4**: Plane-averaged electrostatic potential of the system consisting of a PEG(thiol) monolayer adsorbed on Au(111) obtained with the MBD@rsSCS approach. We set the Fermi level to zero.

6.2.3 The change of the work-function

We investigate the PEG(thiol) molecule-induced change of the work function of Au(111). The plane-averaged electrostatic potential energy for the system with $n = 1$ is shown in Fig. **6-4**. We define the work function of the slab as

$$\Phi = E_{vac} - E_f, \tag{6-1}$$

where E_{vac} and E_f are the electrostatic potential energies at the vacuum level and the Fermi level, respectively.

One can compute the averaged electrostatic potential $\bar{V}$ in xy-planes as follows:

$$\bar{V}(z) = \frac{1}{A} \int \int V(x, y, z) dx dy, \tag{6-2}$$

with A and V being the surface area and the total electrostatic potential. In asymmetric slabs such as our investigated systems, this electrostatic potential should be discontinuous between the two sides of the slab due to a surface dipole. However, an artificial electric field is caused under periodic boundary conditions, removing this discontinuity. To compensate for the artificial electric field, a dipole correction is introduced in Eq. 6-2 [185]:

$$V_{dip}(z) = 4\pi m \left(\frac{z}{z_m} - \frac{1}{2} \right), \tag{6-3}$$

Table **6-2**: PEG(thiol)-induced change in work function, $\Delta\Phi$, and its main components for different numbers of repeat units of the PEG backbone, n. All results, obtained using MBD@rsSCS and DFT-D2, are given in eV.

Repeat units	MBD@rsSCS				DFT-D2			
n	$\Delta\Phi$	ΔV_{BD}	ΔV_{SAM}	$\Delta V_{relax-Au}$	$\Delta\Phi$	ΔV_{BD}	ΔV_{SAM}	$\Delta V_{relax-Au}$
	$(\sqrt{3}\times\sqrt{3})R30°$							
1	-0.76	-1.08	0.36	-0.04	-0.24	-1.01	0.79	-0.02
2	-1.11	-1.06	0.00	-0.05	-0.82	-1.00	0.22	-0.04
3	-0.39	-1.12	0.78	-0.05	-0.26	-1.06	0.84	-0.04
4	-1.16	-1.10	0.00	-0.06	-0.95	-1.02	0.08	-0.01
	$p(\sqrt{3}\times 3)$							
1	-0.37	-0.96	0.64	-0.05	-	-	-	-

where z_m and m denote the size of the unit cell in the z direction and the surface dipole moment, respectively.

As shown in Fig. **6-4**, different vacuum levels are found at both sides of the slab. On the metal side, the work function of the gold surface Φ_{Au} can be obtained, and it is $\Phi_{Au} = 5.15$ eV. This value is in a good agreement with an UPS experiment value of 5.15 eV [186] and theoretical studies, where values of 5.15 eV [187] and 5.12 eV [188] were obtained. The other side of the slab reflects the work function of the PEG molecule-covered surface, and a value of $\Phi_{mod} = 4.39$ eV is found. The change in the work function due to the adsorbed PEG molecules is determined by the difference between Φ_{Au} and Φ_{mod}: $\Delta\Phi = \Phi_{Au} - \Phi_{mod} = -0.76$ eV. $\Delta\Phi$, depending on n, is listed in Table **6-2**. One can find two noticeable features: (i) a significant reduction of the Au(111) work function for all considered systems and (ii) an oscillatory behavior of $\Delta\Phi$, depending on n. A larger-work function modification is observed for even numbers of repeat units. This phenomenon is referred to as an *odd-even effect* [29, 30].

To understand this work-function modification, we decompose $\Delta\Phi$ in the following manner [92–94, 189]:

$$\Delta\Phi = \Delta V_{BD} + \Delta V_{SAM} + \Delta V_{relax-Au}, \tag{6-4}$$

where ΔV_{BD} is the contribution of a dipole between the PEG(thiol) and Au(111) induced by S–Au chemical bonding and ΔV_{SAM} is the contribution due to the intrinsic dipole of the PEG(thiol) monolayer perpendicular to the surface. $\Delta V_{relax-Au}$ reflects the work-function change of the isolated Au surface due to surface relaxation induced by the adsorbed PEG(thiol). We can obtain ΔV_{SAM} through the

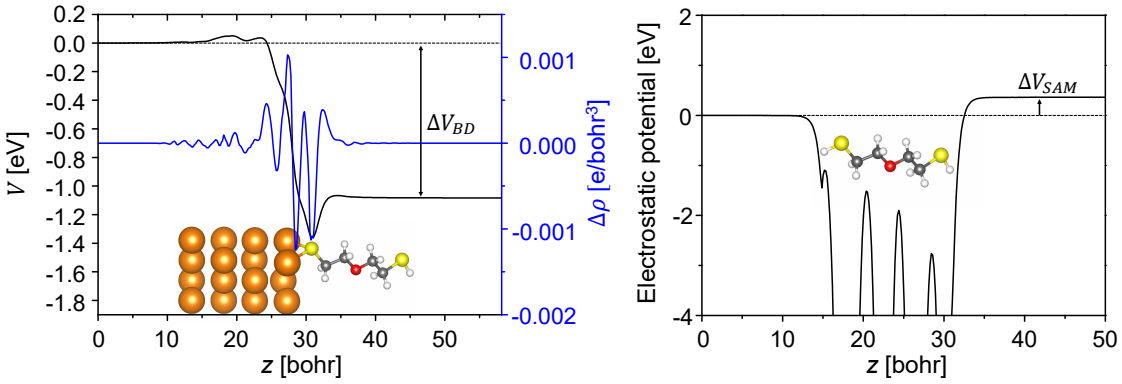

Figure **6-5**: Left: Plane-averaged charge redistribution, $\Delta\rho$, (right axis) and its change of potential energy (left axis), due to the bond dipole (BD) caused by adsorption of 1-PEG(thiol) molecules. A positive (negative) value of $\Delta\rho$ indicates accumulation (depletion) of charge density. Right: Electrostatic potential energy of a free-standing 1-PEG(thiol) layer. All quantities are calculated by the MBD@rsSCS method.

electrostatic potential step across the free-standing PEG(thiol) layer. One likewise defines $\Delta V_{relax-Au}$ as the potential energy step between the two different vacuum levels of the isolated Au(111) surface. ΔV_{BD} can be computed by employing the charge density redistribution resulting from the formation of chemical bonding that leads to the shift in the electrostatic potential ΔV. So, to obtain ΔV_{BD}, we solve the Poisson equation with the plane-averaged density change $\Delta\rho$.

$$\frac{d^2\Delta V}{dz^2} = -4\pi\Delta\rho. \tag{6-5}$$

Here, ΔV_{BD} corresponds to the potential step between the two sides of the slab (see Fig. **6-5**).

When the bonding is formed between the PEG(thiol) molecules and the Au(111) suface, there is a replacement of the S–H bond of thiol by the S–Au bond, and H_2 is released [29, 190]. Therefore, $\Delta\rho$ becomes

$$\Delta\rho = \rho_{tot} - (\rho_{SAM} + \rho_{surf} - \rho_H), \tag{6-6}$$

where ρ_{tot} is the plane-averaged charge density of the total system. ρ_{SAM}, ρ_{surf}, and ρ_H represent the plane-averaged charge densities of the molecular layer saturated with H atoms, the bare Au(111) slab, and the isolated H layer, respectively.

We note that $\Delta\Phi, \Delta V_{BD}, \Delta V_{SAM}$, and $\Delta V_{relax-Au}$ in Eq. 6-4 can be represented in terms of dipole moments, which are computed from the corresponding nuclear charges and self-consistent densities. After some algebra, the difference between the

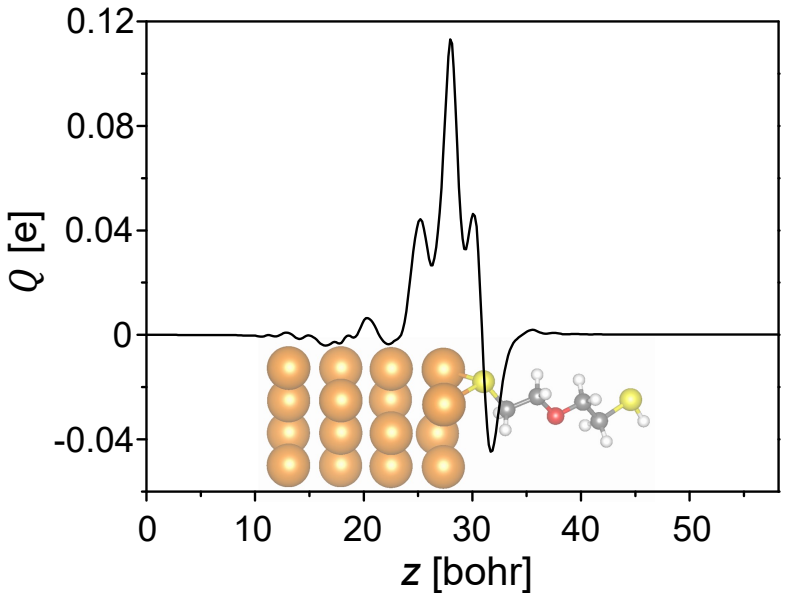

Figure **6-6**: Net charge transfer Q for the adsorption of 1-PEG(thiol) molecules on a Au(111) surface.

right-hand and left-hand sides of Eq. 6-4 is only the dipole moment of the isolated layer of H atoms. Since a H atom has a zero dipole moment along the z direction due to symmetry, we confirm that the summation of ΔV_{BD}, ΔV_{SAM}, and $\Delta V_{relax-Au}$ is consistent with $\Delta\Phi$.

In Fig. **6-5**, we present plots of ΔV_{BD} and ΔV_{SAM} computed by the MBD@rsSCS method for the 1-PEG(thiol)@Au(111) system. The plane-averaged ΔV_{BD} and $\Delta\rho$ along the z-direction are shown in the left panel. Strong fluctuations of the latter are observed at the interface region. This further indicates that $\Delta\rho$ is mostly localized in the vicinity of the interface between the topmost Au layer and the S atom. An accumulation of charge density is found in the topmost Au layer, while the density is depleted right above it. The values of the three contributions to $\Delta\Phi$ for 1-PEG(thiol)@Au(111) are $\Delta V_{BD} = -1.08$ eV, $\Delta V_{SAM} = 0.36$ eV, and $\Delta V_{relax-Au} = 0.04$ eV, respectively. According to our results, ΔV_{BD} plays a crucial role on $\Delta\Phi$. On the other hand, $\Delta V_{relax-Au}$ is negligible compared to ΔV_{BD} and ΔV_{SAM}. The bond dipole induced by the charge-density rearrangement is accompanied by charge transfer. To calculate the net charge transfer Q, $\Delta\rho$ is integrated over the z direction as follows [28, 94, 191]:

$$Q(z) = \int_{-\infty}^{z} \Delta\rho(z')dz'. \tag{6-7}$$

Q provides the total amount of charge moved from right to left in a plane at position z. In other words, a positive (negative) value of Q implies right-to-left (left-to-right)

charge transfer. Figure **6-6** shows a profile of Q for the 1-PEG(thiol) molecules adsorbed on Au(111). We observe positive Q between the sulfur atom and the second Au layer, i.e., charge is transferred from the S atom to the surface. In Fig. **6-6**, a maximum of $Q = 0.11$ e is found across the interface.

Next, we discuss how the three contributions, which determine $\Delta\Phi$, are changed depending on n and the origin of the prominent odd-even effect. We list $\Delta\Phi$, ΔV_{BD}, ΔV_{SAM}, and $\Delta V_{relax-Au}$ in Table **6-2**. ΔV_{BD} has negative values in all cases, but the difference among the values is small compared to $\Delta\Phi$. This implies that ΔV_{BD} does not affect the odd-even effect. We can clarify the insensitivity of ΔV_{BD} to

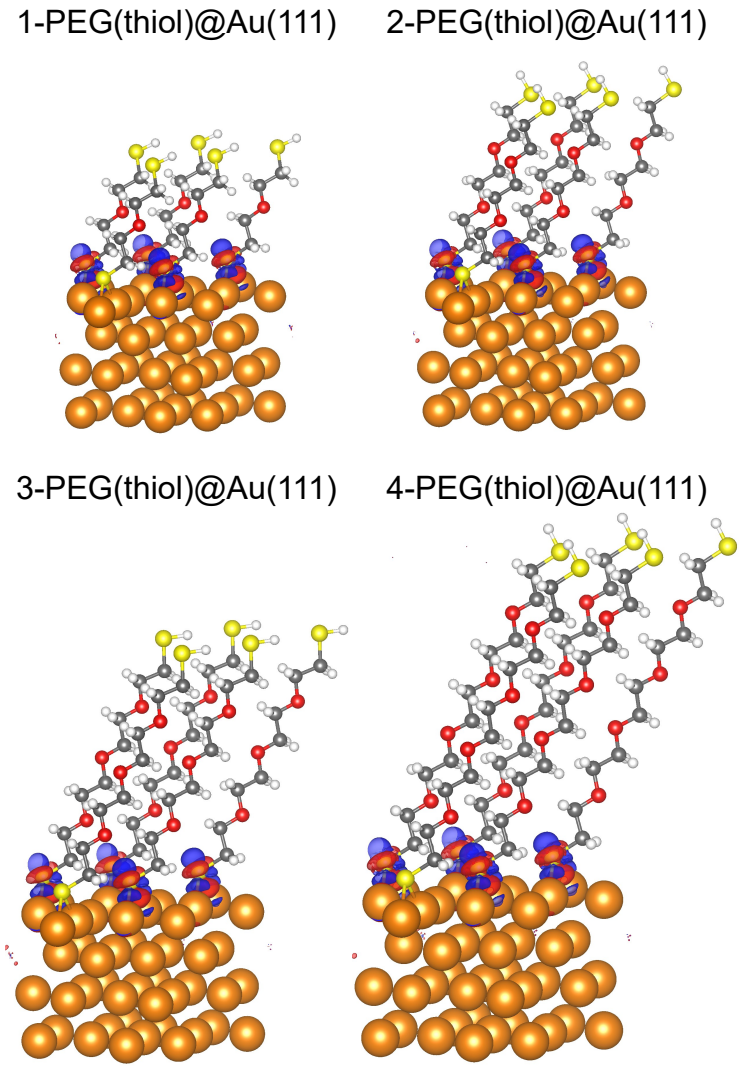

Figure **6-7**: Charge-density redistribution of PEG(thiol)@Au(111) for different numbers of PEG backbone repeat units (n). Blue and red isosurfaces depict charge accumulation and charge depletion, respectively. An isosurface value of 0.0045 e/bohr^3 is used.

n by charge-density redistribution plots for different values of n shown in Fig. **6-7**. They fluctuate mainly at the interface as mentioned before. Interestingly, the charge redistribution is similar regardless of n. This implies a minor difference of ΔV_{BD} among n. The values of $\Delta V_{relax-Au}$ are similar regardless of n and negligibly small. Thus, the surface relaxation induced by the adsorption has also no impact on the odd-even effect.

In contrast to ΔV_{BD} and $\Delta V_{relax-Au}$, ΔV_{SAM} contributes dominantly to the pronounced odd-even effect. Positive values are observed for odd n, whereas they are zero in the case of even n. The latter originates from inversion symmetry within the PEG(thiol), as shown in Fig. **6-1**. Due to symmetry, the intrinsic molecular dipole moment vanishes. We conclude that the odd-even effect is attributed to the dipole moment of PEG(thiol) with respect to the surface normal. The corresponding bond dipole caused by the charge redistribution upon adsorption and surface relaxation play a minor role in the effect.

Previous studies on n-alkanethiols and CF3-terminated n-alkanethiols adsorbed on a Au surface have also shown a similar tendency to such an odd-even effect of $\Delta\Phi$ depending on their molecular length. It was shown to result from the difference in dipole orientation induced by their molecular terminal moieties [30,31]. Noteworthy, $\Delta\Phi$ variations between odd and even molecular length of n-alkanethiols and CF3-terminated n-alkanethiols are significantly smaller than those of the PEG(thiol) molecules [31], i.e., maximally 0.3 eV for the former and 0.77 eV for the latter.

Since vdW forces are important to describe not only organic/metal interfaces [48, 49, 191], but also intermolecular interactions [192], we investigate the influence of the choice of the vdW correction on the work function modification. To this extent, additional calculations are performed using the atom-pairwise dispersion corrected DFT-D2 method [55]. In Fig. **6-8** and Table **6-2**, we report the obtained structural features and the work function modification. We find that the tilting angles θ computed with the MBD@rsSCS method are smaller than those obtained by the DFT-D2 method. The differences between both corrections are larger at shorter molecular lengths, and they decrease as the length increases, exhibiting the same value at $n = 4$. As shown in Fig. **6-8** (a), unlike the DFT-D2 case, θ obtained from the MBD@rsSCS method is not sensitive to the length of the backbone, and its difference between short and long molecules is only a few degrees. In general, short (longer) molecules have weaker (stronger) screening. Therefore, screening effects have a slight influence on θ. We obtain d of 1.92–1.93 Å and 1.93–1.95 Å computed by the DFT-D2 and MBD@rsSCS methods, respectively. The differences in the adsorption heights d are small between those corrections.

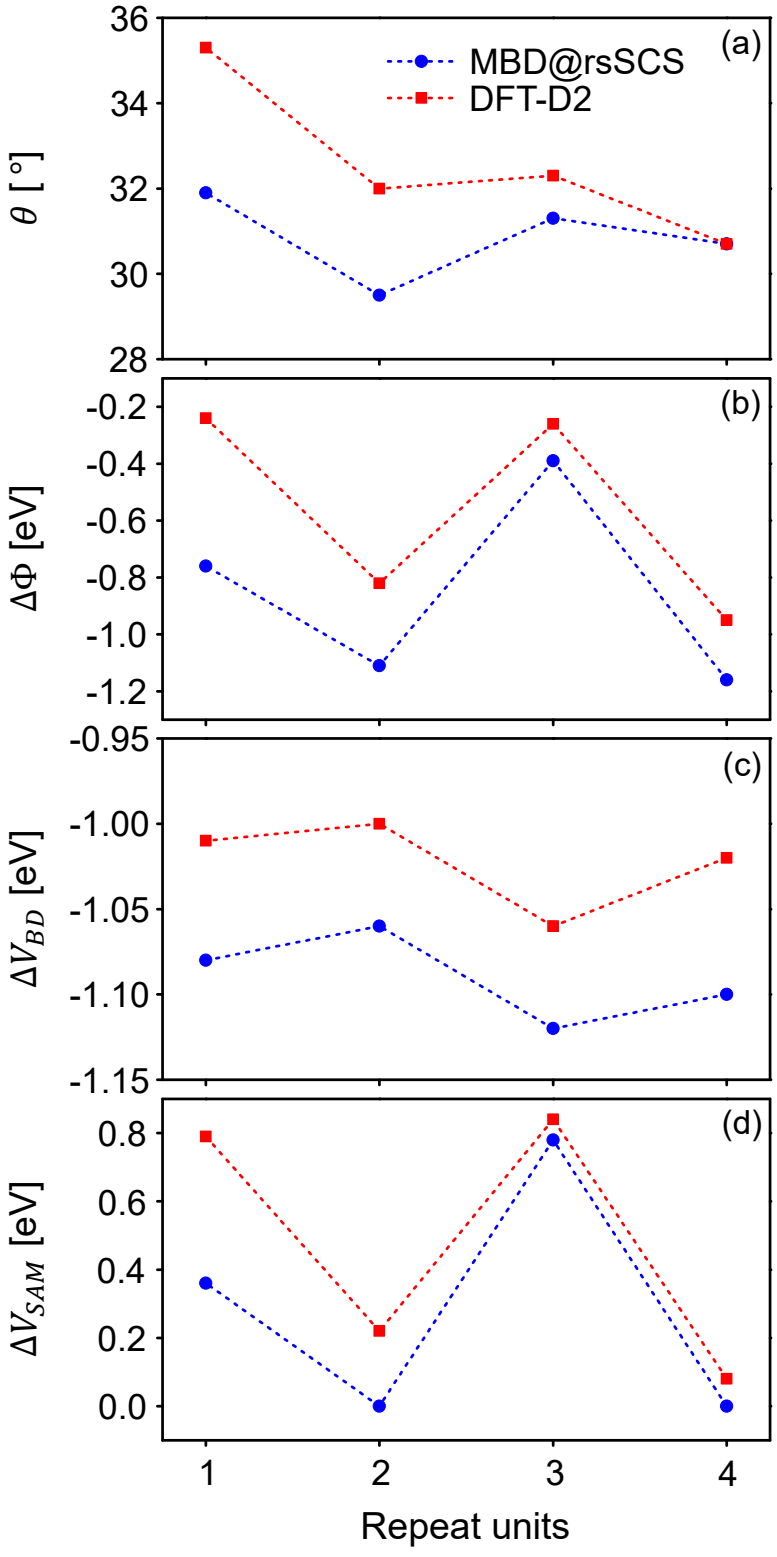

Figure **6-8**: Structural and electronic properties of PEG(thiol) molecules deposited on Au(111) as a function of repeat units, n, obtained with DFT-D2 (red) and MBD@rsSCS (blue): (a) tilting angle, θ, (b) work function modification, $\Delta\Phi$, (c) potential energy change at the interface, ΔV_{BD}, and (d) change in potential energy along the PEG(thiol) molecules, ΔV_{SAM}.

Overall, $\Delta\Phi$ shows a qualitatively similar tendency in both methods (shown in Fig. **6-8** (b)). For example, a reduction of the work function is observed for all four n and a prominent odd-even effect is also revealed. However, $\Delta\Phi$ obtained from the MBD@rsSCS method is larger than the one from the DFT-D2 method. In MBD@rsSCS, the difference of $\Delta\Phi$ between even values of n amounts to 0.05 eV. On the other hand, we observe a larger difference of 0.37 eV between $n = 1$ and $n = 3$. We find that the PEG(thiol) molecules with $n = 1$ are more bent and twisted than the molecules with other values of n. Compared to the MBD@rsSCS method, the difference between odd n is only 0.02 eV in the case of the DFT-D2 method. Therefore, we conclude that the smaller screening of the short molecule is crucial in the MBD@rsSCS results.

The other contributions, ΔV_{BD} and ΔV_{SAM}, computed with both approaches are given in Figs. **6-8** (c) and **6-8** (d). In both methods, the values of ΔV_{BD} are similar. On the contrary, ΔV_{SAM} caused by the intrinsic dipole moment of the PEG(thiol) layer depends on the type of vdW corrections. The variations in the geometry of the adsorbed PEG(thiol) molecules involving the tilting angle between results from MBD@rsSCS and DFT-D2 methods cause this difference. Particularly, in the case of even n, ΔV_{SAM} results in non-zero values for the DFT-D2 method, while those obtained with the MBD@rsSCS method are basically zero. In the DFT-D2 approach, the relaxed molecules have a curved and banana-like shape, unlike those obtained from the MBD@rsSCS method. A finite dipole moment is found due to the absence of inversion symmetry in the molecules. This causes a potential shift, ΔV_{SAM}. There are many differences between the results of the two vdW corrections, nonetheless, the main message is the same.

Lastly, we study how the $p(\sqrt{3} \times 3)$ pattern changes the work function of either Au(111). We list the modified work-function and corresponding individual contributions in Table **6-2**. Similar to the $(\sqrt{3} \times \sqrt{3})R30°$ overlayer, a decreased work function is obtained for the $p(\sqrt{3} \times 3)$ overlayer. The value of $\Delta\Phi$ amounts to -0.37 eV, which is approximately half of that in the $(\sqrt{3} \times \sqrt{3})R30°$ overlayer with $n = 1$. Fewer distorted PEG molecules in the herringbone pattern, compared to the $(\sqrt{3} \times \sqrt{3})R30°$ overlayer, result in this difference. Interestingly, $\Delta\Phi$ is similar to that in the $(\sqrt{3}\times\sqrt{3})R30°$ case for $n = 3$. The values of corresponding contributions, ΔV_{BD} and ΔV_{SAM} are slightly smaller in comparison with the structure. However, we find that the differences of these contributions are canceled out, causing nearly identical work function modification.

According to calculations obtained by the MBD@rsSCS and DFT-D2 methods for the $(\sqrt{3} \times \sqrt{3})R30°$ pattern, $\Delta\Phi$ are similar for n values with the same parity

when the adsorption molecules are less distorted and are in an upright configuration. We expect that the herringbone pattern exhibits similar behavior, thus, both overlayer structures provide similar work function changes when n is bigger than one. As explained in Sec. 6.2.1, the $p(\sqrt{3} \times 3)$ and $(\sqrt{3} \times \sqrt{3})R30°$ structures can exist simultaneously on the Au surface creating a disordered structure. From our results, for $n > 1$ we anticipate that the modification of the work function in this disordered phase is nearly the same as the case of the $p(\sqrt{3} \times 3)$ or $(\sqrt{3} \times \sqrt{3})R30°$ structure.

6.3 PEG(thiol) adsorbed on Ag(111)

6.3.1 Computational details

Silver is an alternative material that can be used as an electrode, exhibiting the highest electrical and thermal conductivity among all metals at 293 K. For the gold substrate, as described in Sec. 6.2, we consider the system of a SAM consisting of PEG(thiol) molecules adsorbed on the Ag(111) surface, termed PEG(thiol)@Ag(111) with the same numbers of repeat unit, i.e., $n = 1 - 4$. An experimental study of low-energy electron diffraction (LEED) has shown that a $(\sqrt{7} \times \sqrt{7})R10.9°$ overlayer of thiolate molecules is formed at high-coverage [193–196]. A reconstruction of the Ag(111) surface induced by thiolate has been reported experimentally [197–200]. We thus employ the $(\sqrt{7} \times \sqrt{7})R10.9°$ surface unit cell for our calculations. Based on this structure, the reconstruction of its topmost layer is considered with 2, 3, and 4 vacancies in the substrate. Such structures consist of three PEG(thiol) molecules per unit cell. For the sake of comparison, a $(\sqrt{3} \times \sqrt{3})R30°$ unit cell having only one PEG molecule is also employed. All considered structures are displayed in Fig. **6-9**.

The Ag(111) surface is modeled with a four-layer slab, and the two topmost layers are relaxed. A vacuum space of at least 14 Å along the perpendicular direction is employed to minimize interactions between periodic images of the investigated system. We adopt an in-plane lattice constant of 4.16 Å for the Ag surface. The relaxation of atomic positions is performed until the maximum force reaches less than 0.01 eV/Å. The BZ is sampled with a $5 \times 5 \times 1$ and a $8 \times 8 \times 1$ **k**-point grid for the $(\sqrt{7} \times \sqrt{7})R10.9°$ and $(\sqrt{3} \times \sqrt{3})R30°$ structures, respectively.

The calculations are computationally demanding in the FP-LAPW method because the size of the surface unit cell is large. Therefore, the calculations of the PEG(thiol)@Ag(111) system are performed using the Vienna ab initio simulation package (VASP) [39]. A many-body dispersion correction for the van der Waals in-

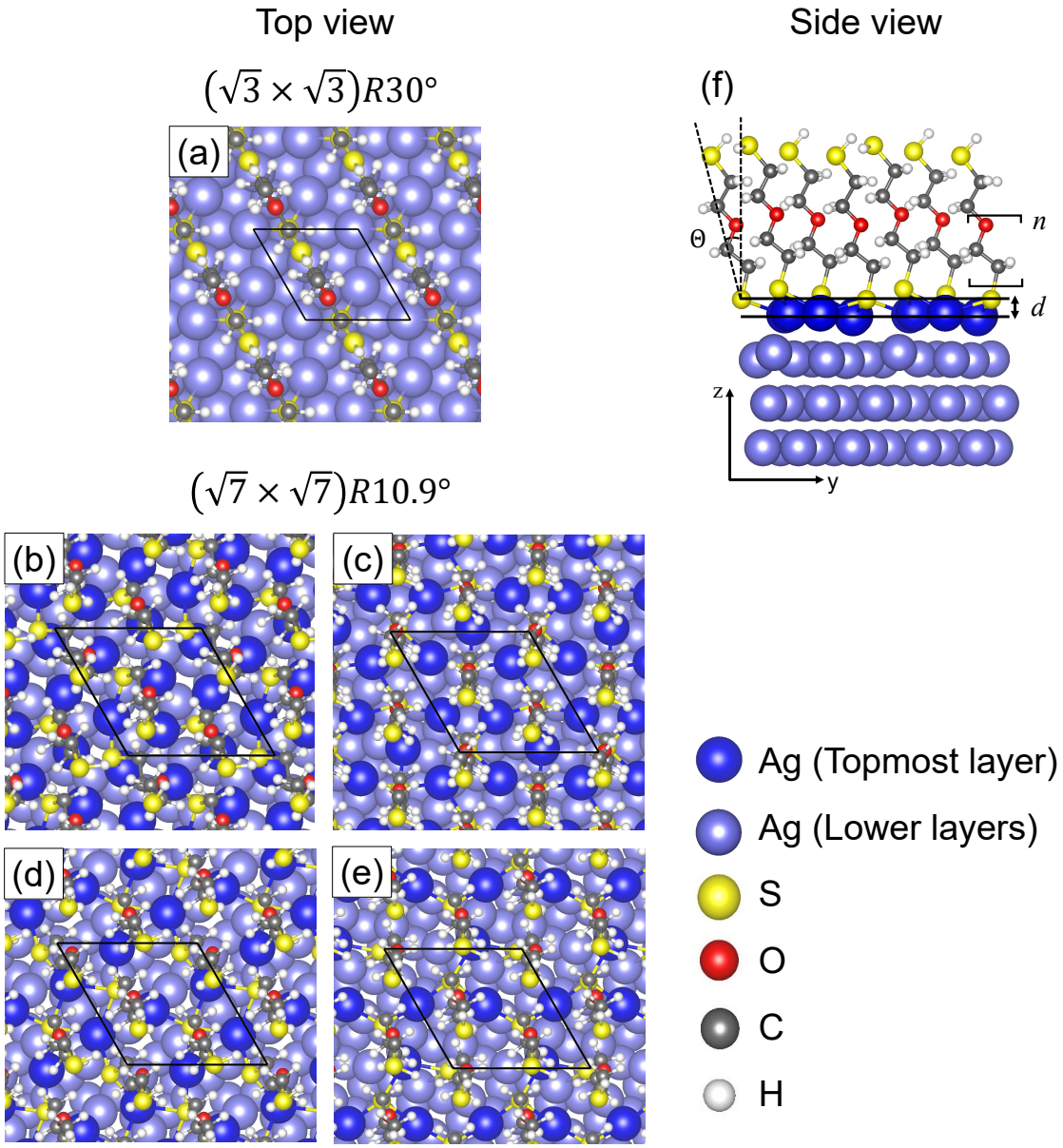

Figure **6-9**: Structures of PEG(thiol) molecules adsorbed on the Ag(111) surface in (a) $(\sqrt{3}\times\sqrt{3})R30°$ (b)–(e) $(\sqrt{7}\times\sqrt{7})R10.9°$ with substrate vacancies: (b) $v = 0$, (c) $v = 2$, (d) $v = 3$, and (e) $v = 4$. (f) Side view of the $(\sqrt{7}\times\sqrt{7})R10.9°$ structure with two vacancies. θ and d are the tilting angle between the PEG backbone and the surface normal and the adsorption height between the average position of S atoms and that of surface atoms, respectively. n indicates the number of repeat units of the PEG chain.

teractions is not implemented in VASP (version 5.3.2). Thus, to consider long-range correlation effects, we use the semi-empirical DFT-D2 functional. The energy cutoff for the plane wave basis set is set to 700 eV to solve the Kohn-Sham equations. For the exchange-correlation functional, we use the GGA in the PBE parametrization [113].

6.3.2 Adsorption geometry

To investigate the stability of investigated structures, the adsorption energy is calculated. The adsorption energy per adsorbed PEG(thiol) is given by

$$E_{ads} = \frac{E_{tot} - (E_{surf} + mE_{mol})}{m} + \frac{E_{H_2}}{2}, \tag{6-8}$$

where E_{tot} is the total energy of PEG(thiol)@Ag(111), E_{surf} and E_{mol} represent the total energies of the bare Ag(111) slab and the gas-phase PEG molecule saturated with a H atom, respectively. m indicates the number of molecules in the unit cell. E_{H_2} is the energy of the isolated hydrogen molecule. In systems with substrate vacancies, the adsorption energy is changed due to surface reconstruction. The energy to reconstruct the Ag surface is given by

$$E_{rec} = E_{surf} - E_{Ag(111)} + vE_{Ag}^{bulk}. \tag{6-9}$$

Here, E_{surf} and $E_{Ag(111)}$ are the total energies of the reconstructed and unreconstructed surfaces, respectively. E_{Ag}^{bulk} reflects the total energy of bulk Ag per atom and v is the number of vacancies. Finally, we can compute the net adsorption energy using Eqs. 6-8 and 6-9 as

$$E_{ads}^{net} = E_{ads} + \frac{E_{rec}}{m}. \tag{6-10}$$

In Table **6-3**, we list the corresponding values of E_{ads}, E_{rec}, and E_{ads}^{bulk} of our systems with one repeat unit of the PEG backbone (1-PEG(thiol)@Ag(111)). In the

Table **6-3**: Adsorption energy E_{ads}, reconstruction energy E_{rec}, and net adsorption energy E_{ads}^{net} for various Ag surface structures involving surface vacancies.

Surface structure	vacancy	E_{ads} [eV]	E_{rec} [eV]	E_{ads}^{net} [eV]
$(\sqrt{7} \times \sqrt{7})R10.9°$	-	-1.21	-	-1.21
$(\sqrt{7} \times \sqrt{7})R10.9°$	2	-1.70	1.13	-1.32
$(\sqrt{7} \times \sqrt{7})R10.9°$	3	-1.87	1.72	-1.29
$(\sqrt{7} \times \sqrt{7})R10.9°$	4	-1.72	1.48	-1.22
$(\sqrt{3} \times \sqrt{3})R30°$	-	-1.08	-	-1.08

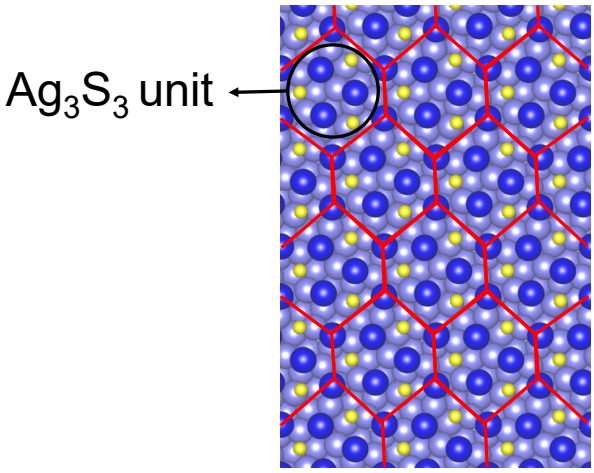

Figure **6-10**: Top view of the relaxed PEG(thiol)@Ag(111) structure with two vacancies. For the sake of convenience, we do not show the molecular backbone. Ag_3S_3 units are surrounded by the hexagonal shape formed by Ag atoms of the topmost layer.

case of the $(\sqrt{3}\times\sqrt{3})R30°$ structure, the net adsorption energy is much higher than that in all calculations of $(\sqrt{7}\times\sqrt{7})R10.9°$. Thus, the $(\sqrt{7}\times\sqrt{7})R10.9°$ structure is energetically more stable than $(\sqrt{3}\times\sqrt{3})R30°$. This result explains why the former structure is experimentally observed. In the $(\sqrt{7}\times\sqrt{7})R10.9°$ structure, the net adsorption energy of the reconstructed surface with four vacancies is close to that of the unreconstructed surface. Overall, the lowest net adsorption energy is obtained for the structure including the surface reconstruction with two vacancies. This structure thereby exhibits higher stability than other structures and supports recently reported experimental results of the reconstruction of the Ag(111) surface due to the adsorption of thiolate as mentioned above [197–200].

Our calculations show that the S atoms of the head group in three PEG(thiol) molecules occupy three adsorption sites: slightly shifted hollow sites of (i) hcp, (ii) fcc, and (iii) atop sites. As shown in Fig. **6-10**, we observe triangular shapes formed by three adsorbed molecules as well as by three Ag atoms of the topmost layer next to the molecules. A scanning tunneling microscopy (STM) experiment of sulfurs deposited on Ag(111) shows these Ag_3S_3 units [201]. In addition, a hexagonal-like arrangement of Ag atoms surrounds each of these Ag_3S_3 units, and this arrangement has also been reported in Refs. [202] and [203].

The optimized structural parameters in the $(\sqrt{7}\times\sqrt{7})R10.9°$ structure with two vacancies, referred to as PEG(thiol)@Ag(111)-2v, are listed in Table **6-4**. According to our calculations, the averaged tilting angle θ of the PEG(thiol) molecules

Table **6-4**: Adsorption geometry properties of PEG(thiol)@Ag(111) containing two vacancies.

Repeat units (n)	1	2	3	4
θ [°]	-13.58	-12.14	-11.05	-10.29
d [Å]	1.11	1.11	1.11	1.11

relative to the surface normal is $-11.77°$. This value is similar with that found for n-alkanethiols on the silver surface [194]. θ is insensitive to n, nevertheless, it is insignificantly getting smaller as n increases. Interestingly, in comparison with the PEG(thiol)@Au(111) system discussed in Sec. 6.2.2, this system yields negative values of θ irrespective of n. The adsorption height d remains unchanged while altering the molecular length. This vertical height is slightly smaller than the experimental value of 1.23±0.07 Å obtained by normal-incidence X-ray standing wave (NIXSW) analysis [198].

To understand the nature of interactions between the molecules and the Ag surface, we examine total and partial density of states (DOS) in Fig. **6-11**. The reconstruction in the topmost layer causes the slightly narrower DOS of the Ag component. The broadening of the PEG(thiol) states compared to the pristine monolayer indicates interactions between the molecules and the surface, such as the formation of new chemical bonds. As shown in Fig. **6-11** (b), Ag d-states of the first layer in the total system are wider compared to those in the clean Ag surface, and an overlap of the PDOS between the S atoms and the topmost layer is found. Therefore, the Ag–S bonds are attributed to interactions among s- and p-states of the S atoms and s-, p-, and d-states of the Ag atoms.

6.3.3 The change of the work-function

In this section, we discuss how the deposited PEG(thiol) molecules affect the work function of the Ag(111) surface and compare the results with the PEG(thiol)@Au(111) system. We firstly evaluate the work function of the surface, Φ_{Ag}. The plane-averaged electrostatic potential of 1-PEG(thiol)@Ag(111)-2v is illustrated in Fig. **6-12**. Our calculation yields a value of $\Phi_{Ag} = 4.43$ eV, which is reasonably close to that measured by an experiment (4.46 ± 0.02 eV) [204]. Like the PEG(thiol)@Au(111) system, a PEG(thiol)-induced work function modification $\Delta\Phi$ is found. The values of $\Delta\Phi$ with respect to n are summarized in Table **6-5** and Fig. **6-13** (a). Similar to the PEG(thiol)@Au(111) case, a decrease in the metal work function is found in all cases. Moreover, the variation of $\Delta\Phi$ in the range from -0.10 to -0.33 eV,

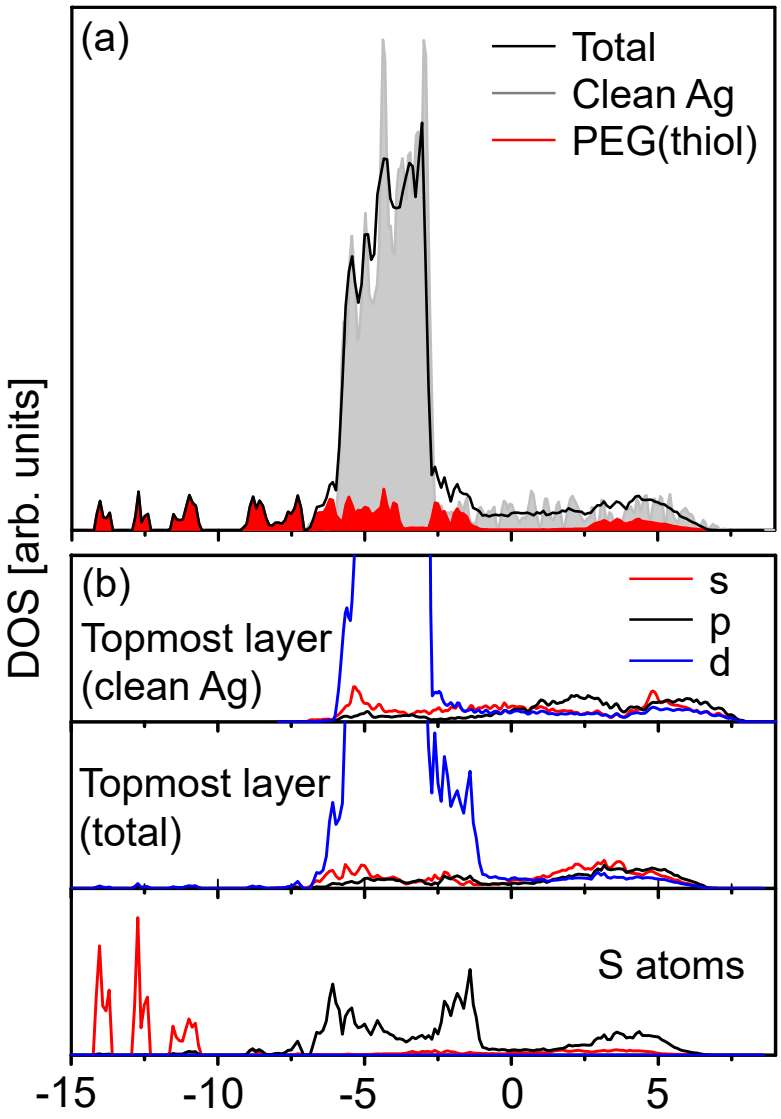

Figure **6-11**: (a) Total DOS of the clean Ag(111) surface, 1-PEG(thiol)@Ag(111)-2v, and the adsorbed PEG(thiol) molecules. (b) Partial DOS of *s*-, *p*-, and *d*-states of the topmost layer of clean Ag (top) and the total system (middle), and adsorbed S atoms (bottom). We set the Fermi level to zero.

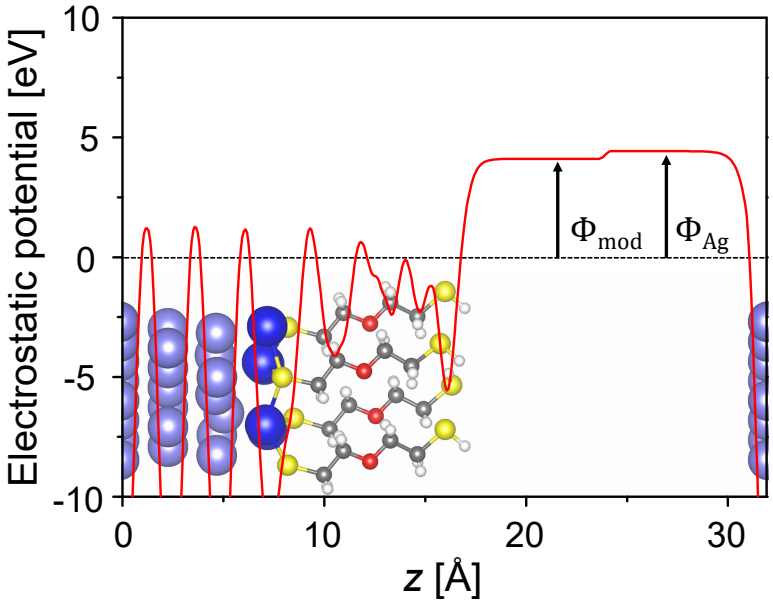

Figure **6-12**: Plane-averaged electrostatic potential of PEG(thiol) adsorbed on Ag(111) with $n = 1$. The Fermi level is set to zero.

depending on n, indicates an odd-even effect. The difference of $\Delta\Phi$ between odd and even n is 0.23 eV at maximum, which is remarkably lower than that of the system using a Au(111) surface.

As described in Sec. 6.2.3, the work function modification arises from three contributions: (i) ΔV_{BD} due to the formation of chemical bonds that results in the charge rearrangement, (ii) ΔV_{SAM} due to the intrinsic dipole of the PEG(thiol) molecular layer, and (iii) $\Delta V_{relax-Ag}$ due to the molecule-induced surface relaxation including the reconstruction. $\Delta\Phi$ can be expressed as a summation of these contributions:

$$\Delta\Phi = \Delta V_{BD} + \Delta V_{SAM} + \Delta V_{relax-Ag}. \tag{6-11}$$

Table **6-5** and Fig. **6-13** show the corresponding quantities. It should be noted that the same approaches used in Sec. 6.2.3 are exploited to compute the values of the corresponding contributions. ΔV_{SAM} and $\Delta V_{relax-Ag}$ are negative, while ΔV_{BD} is positive. In contrast, $\Delta\Phi$ of the PEG(thiol)@Au(111) is mainly dominated by ΔV_{BD}.

Figure **6-13** (b) exhibits that ΔV_{BD} increases the Ag work function for all n. The positive values indicate metal-to-molecule electron transfer at the interface. In the case of the Au(111) surface, an opposite situation (molecule-to-metal electron transfer) is encountered as explained in Sec. 6.2.3. For example, the Au work function is reduced by ΔV_{BD} and the charge is transferred from the S atoms of head group molecules to the Au surface. Similar to PEG(thiol)@Au(111), the values of ΔV_{BD}

Table **6-5**: Work function change $\Delta\Phi$ of 1-PEG(thiol)@Ag(111)-2v caused by PEG(thiol) molecules and its three contributions for various numbers of repeat units of the PEG molecular chain, n. All values are in eV.

Repeat units (n)	$\Delta\Phi$	ΔV_{BD}	ΔV_{SAM}	$\Delta V_{relax-Ag}$
1	-0.31	0.45	-0.39	-0.37
2	-0.10	0.44	-0.18	-0.36
3	-0.33	0.43	-0.39	-0.37
4	-0.23	0.46	-0.32	-0.37

are very similar regardless of the molecular backbone length. The pronounced odd-even effect thus does not come from ΔV_{BD}. $\Delta V_{relax-Ag}$ amounts to approximately -0.37 eV as shown in Fig. **6-13** (c). These values are considerably lower than those in the PEG(thiol)@Au(111) case, which exhibits negligible values. Like ΔV_{BD}, the differences of $\Delta V_{relax-Ag}$ among n are tiny. Therefore, we conclude that the reconstruction of the Ag surface induced by the adsorption of PEG(thiol) molecules has little impact on the odd-even effect.

Unlike ΔV_{BD} and $\Delta V_{relax-Ag}$, ΔV_{SAM} is sensitive to n, manifesting the odd-even effect. This implies that the dipole moment of the PEG(thiol) monolayer perpendicular to the surface contributes to the pronounced odd-even effect on $\Delta\Phi$. A similar trend is obtained in the case of PEG(thiol)@Au(111). However, we find that there is a significant difference between the systems of Ag(111) and Au(111). ΔV_{SAM} decreases the work function of the former, whereas it increases that of the latter. Such a difference is caused by the difference of the adsorption geometry, such as tilting angle θ as discussed above. For example, the molecules are adsorbed on Ag(111) in an opposite orientation to the Au(111) surface.

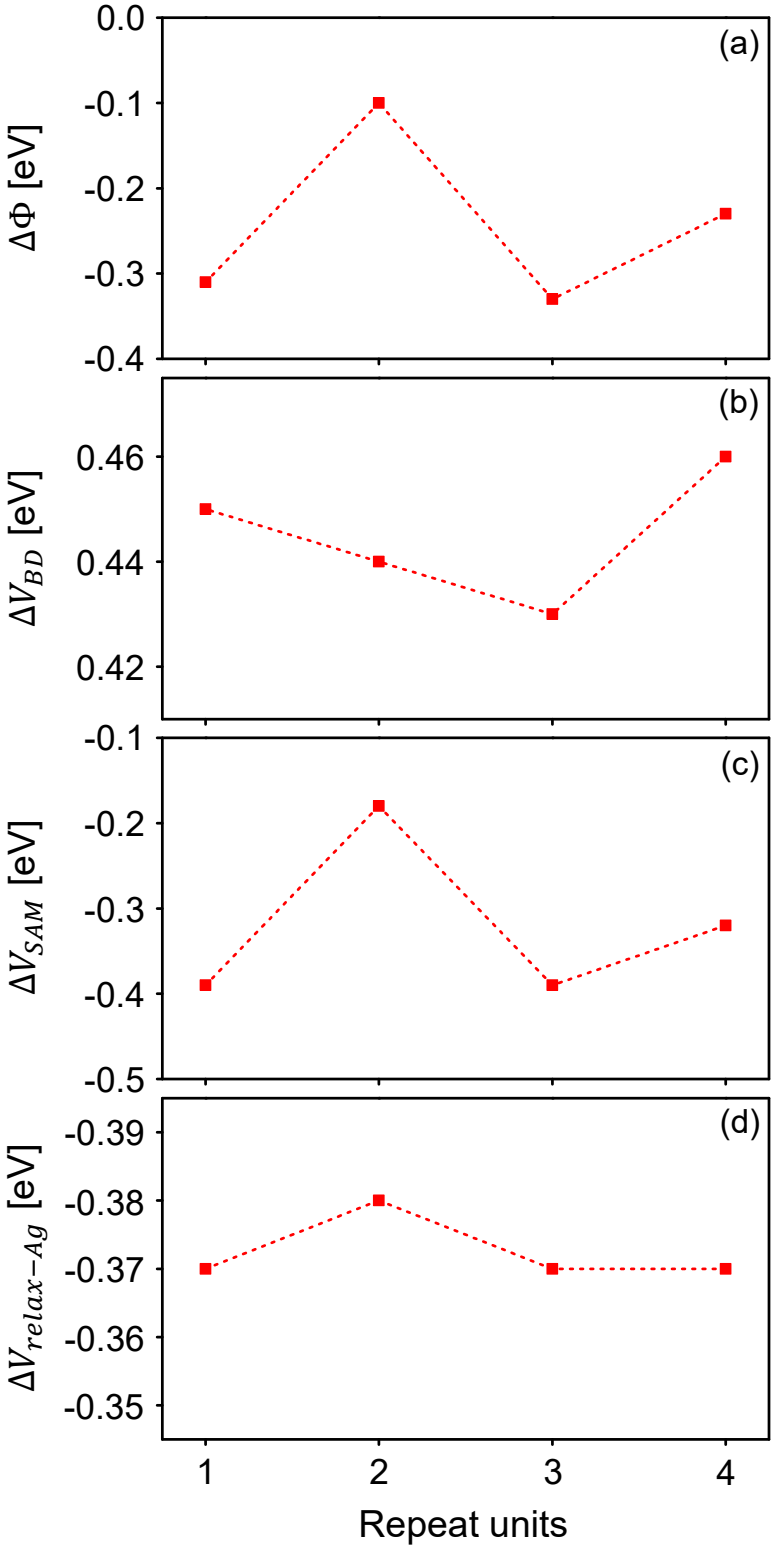

Figure **6-13**: (a) Change in work function $\Delta\Phi$, (b) bond-dipole-induced potential energy change ΔV_{BD}, (c) potential-energy change across the PEG(thiol) monolayer, and (d) work-function shift of the reconstructed Ag surface for PEG(thiol) adsorbed onto Ag(111) with respect to n.

7. Conclusions and summary

Organic electronics devices face fundamental challenges due to poor charge injection (extraction) at an organic/electrode interface. The most effective way to avoid this drawback is adjusting the work function of electrodes. Indeed, interlayers between an active layer and cathode have a significant influence on the cathode work function, thus, impacting the performance of such devices. To explain physics and chemistry behind this effect, we have performed the DFT calculations for Au(111) and Ag(111) covered by a PEG(thiol) monolayer with different numbers of repeat units in the PEG molecular backbone.

Van der Waals interactions heavily contribute to the adsorption geometry of the interface. In order to consider the interactions, we have employed the DFT-D2 and MBD@rsSCS methods, and have carried out a reciprocal space implementation of the latter method in the **exciting** code. Further, we have applied the MBD@rsSCS method to three test cases: graphene, h-BN, and graphite fluoride. The many-body effects as well as screening effects are included in MBD@rsSCS. Our results have confirmed that the inclusion of MBD@rsSCS yields an improvement of the adsorption energy and the interlayer distance over standard PBE and other methods. This indicates that this MBD@rsSCS method is accurate. Therefore, the many-body dispersion effects play an essential role in accurately predicting and designing materials.

Since our systems suffer from poor convergence of self-consistent field iteration, it is necessary to consider a newly devised mixing algorithm. To ensure smooth convergence, the Kerker preconditioner and inverse Kerker metric are reconstructed to be applied in the FP-LAPW method. The modified Pulay mixing including these approaches has been implemented in **exciting**. We have compared the performance of this method with that of other methods: simple Pulay and msec. In benchmark cases, particularly metallic systems with large unit cells, the implemented mixing algorithm provides an improvement of convergence over other methods with density and potential mixings. We have demonstrated that issues of charge-sloshing and noisy potentials are addressed, and this mixing outperforms the simple Pulay and

msec methods. Thus, it is robust and the most efficient. For our investigated systems, we have used the implemented mixing method.

According to our results, the tilting angles of approximately 30 ° have been observed between PEG(thiol) and the surface normal in PEG(thiol)@Au(111). The computed adsorption distance between the S atom and the average position of the first layer atoms amounts to $\sim$ 1.93 Å. These structural parameters are similar irrespective of the PEG backbone length. The obtained results have revealed that the PEG(thiol) molecules always decrease the work function of the Au(111) surface. This reduction reflects the minimizing charge injection (extraction) energy barriers. Interestingly, the modification of the work function varies in range from -0.24 eV to -0.95 eV depending on the number of molecular repeat units in the case of the DFT-D2 scheme. This range is corrected from -0.39 eV to -1.16 eV by the MBD@rsSCS scheme. This work function shift results from the bond dipole due to the adsorption-induced charge rearrangement at the interface. In fact, the work function of the Au(111) surface is less reduced for an odd number of repeat units of the PEG(thiol) molecules, whereas the work function change is larger for an even number. This variation is known as an odd-even effect. We have found that the profound odd-even effect mostly originates from the intrinsic dipole moment of these molecules.

The importance of the molecular arrangement pattern has been studied by considering a $p(\sqrt{3} \times 3)$ unit cell, which has a herringbone-like pattern of molecules in the 1-PEG(thiol)@Au(111) system. According to our MBD@rsSCS calculations, the parameters of the adsorption geometry are similar to those in the $(\sqrt{3} \times \sqrt{3})R30°$ pattern. In addition, a reduced work function has been also observed. Its magnitude is larger than that in $(\sqrt{3} \times \sqrt{3})R30°$ with one repeat unit. On the other hand, both surface unit cells yield nearly identical work function change when the number of repeat units is larger than one.

We have investigated different structures of PEG(thiol) adsorbed on Ag(111). These calculations have been performed by the VASP code, and we have used the DFT-D2 method for van der Waals forces. We have found that a reconstructed $(\sqrt{7} \times \sqrt{7})R10.9°$ surface unit cell involving two vacancies on the topmost layer is the most energetically stable structure. In addition, the PEG(thiol) molecules are tilted by $\sim -12°$ with respect to the surface normal. The orientation of these molecules is opposite compared to PEG(thiol)@Au(111). The adsorbed PEG(thiol) molecules lead to a decrease in the work function of the Ag surface regardless of molecular length. Like the PEG(thiol)@Au(111) case, a pronounced odd-even effect is observed on the work function modification depending on the number of repeat

units, and this effect arises from the contribution of the molecular layer dipole. All contributions to this work function change differ considerably from those in the corresponding Au case.

Part III

Appendix

A. Interatomic forces of MBD@rsSCS

The interatomic forces for structure optimizations can be expressed as

$$\mathbf{F}_{disp} = \sum_{\boldsymbol{k}} w_{\boldsymbol{k}} \int_0^\infty \frac{d\omega}{2\pi} \mathrm{Tr}\{[\mathbf{1} - \mathbf{A}_{LR}(\omega)\mathbf{T}_{LR}(\boldsymbol{k})]^{-1} \nabla[\mathbf{A}_{LR}(\omega)\mathbf{T}_{LR}(\boldsymbol{k})]\}, \tag{A-1}$$

where

$$\nabla[\mathbf{A}_{LR}(\omega)\mathbf{T}_{LR}(\boldsymbol{k})] = \mathbf{A}_{LR}(\omega)\nabla\mathbf{T}_{LR}(\boldsymbol{k}) + \nabla\mathbf{A}_{LR}(\omega)\mathbf{T}_{LR}(\boldsymbol{k}). \tag{A-2}$$

We differentiate Eq. A-2 in terms of Cartesian components of atomic positions, r_α^a.

A.1 $\nabla\mathbf{A}_{LR}(\omega)$

At first, we calculate the derivative of $\mathbf{A}_{LR}(\omega)$ with regard to r_α^a as follows:

$$\frac{\partial A_{LR,ij}^{bc}(\omega)}{\partial r_\alpha^a} = \frac{\partial \tilde{\alpha}_i^{\mathrm{SCS,iso}}(\omega)}{\partial r_\alpha^a} \delta_{ij}\delta_{bc}. \tag{A-3}$$

Following Eq. 5-32, Eq. A-3 transforms into

$$\frac{\partial \tilde{\alpha}_i^{\mathrm{SCS,iso}}(\omega)}{\partial r_\alpha^a} = \frac{1}{3}\sum_{a'}\sum_{j=1}^{N} \frac{\partial \tilde{A}_{ij}^{a'a'}(\omega)}{\partial r_\alpha^a}. \tag{A-4}$$

The derivative of $\tilde{\mathbf{A}}(\omega)$ in terms of r_α^a is proposed by Ref. [205], and it reads

$$\begin{aligned} \frac{\partial A_{ij}^{bc}}{\partial r_\alpha^a} &= \sum_{i',j'}^{N}\sum_{b',c'} A_{ii'}^{bb'} \frac{\partial T_{SR,i'j'}^{b'c'}}{\partial r_\alpha^a} A_{j'j}^{c'c} \\ &= \sum_{b'c'}\sum_{j'}^{N} A_{i\alpha}^{bb'} \frac{\partial T_{SR,\alpha j'}^{b'c'}}{\partial r_\alpha^a} A_{j'j}^{c'c} + \sum_{b'c'}\sum_{i'}^{N} A_{ii'}^{bb'} \frac{T_{SR,i'\alpha}^{b'c'}}{\partial r_\alpha^a} A_{\alpha j}^{c'c}. \end{aligned} \tag{A-5}$$

For the sake of convenience, we refer to $\tilde{\mathbf{A}}$ as $\mathbf{A}$, and ω is not written in Eq. A-5. One can obtain the derivative of short-range dipole-dipole interaction tensor in this manner:

$$\frac{\partial T_{SR,ij}^{ab}}{\partial r_i^a} = {\sum_{\boldsymbol{L}}}' \left\{ (1 - f(S_{\mathrm{vdW},ij}, r_{ij,\boldsymbol{L}})) \frac{\partial \tau_{SR,ij}^{ab}}{\partial r_i^a} - \frac{\partial f(S_{\mathrm{vdW},ij}, r_{ij,\boldsymbol{L}})}{\partial r_i^a} \tau_{SR,ij}^{ab} \right\}, \tag{A-6}$$

where

$$\tau_{SR,ij}^{ab} = -\sum_{\boldsymbol{L}}{}' \frac{3r_{ij,\boldsymbol{L}}^a r_{ij,\boldsymbol{L}}^b - (r_{ij,\boldsymbol{L}})^2\delta_{ab}}{(r_{ij,\boldsymbol{L}})^5}\left(\mathrm{erf}\left(\frac{r_{ij,\boldsymbol{L}}}{\sigma_{ij}}\right) - \frac{2}{\sqrt{\pi}}\frac{r_{ij,\boldsymbol{L}}}{\sigma_{ij}}\exp\left[-\left(\frac{r_{ij,\boldsymbol{L}}}{\sigma_{ij}}\right)^2\right]\right) + \frac{4}{\sqrt{\pi}}\frac{1}{(\sigma_{ij})^3}\frac{r_{ij,\boldsymbol{L}}^a r_{ij,\boldsymbol{L}}^b}{(r_{ij,\boldsymbol{L}})^2}\exp\left[-\left(\frac{r_{ij,\boldsymbol{L}}}{\sigma_{ij}}\right)^2\right]. \tag{A-7}$$

The derivative of $\tau_{ij}^{SR,ab}$ reads

$$\begin{aligned}\frac{\partial\tau_{SR,ij}^{ab}}{\partial r_i^a} &= -\frac{\partial\tau_{SR,ij}^{ab}}{\partial r_j^a} \\ &= \sum_{\boldsymbol{L}}{}'\Bigg[-3\left((1+2\delta_{ab})\frac{r_{ij,\boldsymbol{L}}^b}{(r_{ij,\boldsymbol{L}})^5} - 5\frac{(r_{ij,\boldsymbol{L}}^a)^2 r_{ij,\boldsymbol{L}}^b}{(r_{ij,\boldsymbol{L}})^7}\right)\mathrm{erf}\left(\frac{r_{ij,\boldsymbol{L}}}{\sigma_{ij}}\right) \\ &\quad + \frac{(1+2\delta_{ab})}{\sqrt{\pi}}\frac{r_{ij,\boldsymbol{L}}^b}{(r_{ij,\boldsymbol{L}})^4}\frac{1}{\sigma_{ij}^3}\left(6\sigma_{ij}^2 + 4(r_{ij,\boldsymbol{L}})^2\right)\exp\left[-\left(\frac{r_{ij,\boldsymbol{L}}}{\sigma_{ij}}\right)^2\right] \\ &\quad - \frac{1}{\sqrt{\pi}}\frac{(r_{ij,\boldsymbol{L}}^a)^2 r_{ij,\boldsymbol{L}}^b}{(r_{ij,\boldsymbol{L}})^6}\frac{1}{\sigma_{ij}^5}\left(30\sigma_{ij}^4 + 20\sigma_{ij}^2(r_{ij,\boldsymbol{L}})^2 + 8(r_{ij,\boldsymbol{L}})^4\right)\exp\left[-\left(\frac{r_{ij,\boldsymbol{L}}}{\sigma_{ij}}\right)^2\right]\Bigg].\end{aligned} \tag{A-8}$$

In the case of $a \neq b \neq c$, Eq. A-8 becomes

$$\begin{aligned}\frac{\partial\tau_{SR,ij}^{ab}}{\partial r_i^c} &= -\frac{\partial\tau_{SR,ij}^{ab}}{\partial r_j^c} \\ &= \sum_{\boldsymbol{L}}{}'\Bigg[-3\left(\delta_{ab}\frac{r_{ij,\boldsymbol{L}}^c}{(r_{ij,\boldsymbol{L}})^5} - 5\frac{r_{ij,\boldsymbol{L}}^a r_{ij,\boldsymbol{L}}^b r_{ij,\boldsymbol{L}}^c}{(r_{ij,\boldsymbol{L}})^7}\right)\mathrm{erf}\left(\frac{r_{ij,\boldsymbol{L}}}{\sigma_{ij}}\right) \\ &\quad + \frac{\delta_{ab}}{\sqrt{\pi}}\frac{r_{ij,\boldsymbol{L}}^c}{(r_{ij,\boldsymbol{L}})^4}\frac{1}{\sigma_{ij}^3}\left(6\sigma_{ij}^2 + 4(r_{ij,\boldsymbol{L}})^2\right)\exp\left[-\left(\frac{r_{ij,\boldsymbol{L}}}{\sigma_{ij}}\right)^2\right] \\ &\quad - \frac{1}{\sqrt{\pi}}\frac{r_{ij,\boldsymbol{L}}^a r_{ij,\boldsymbol{L}}^b r_{ij,\boldsymbol{L}}^c}{(r_{ij,\boldsymbol{L}})^6}\frac{1}{\sigma_{ij}^5}\left(30\sigma_{ij}^4 + 20\sigma_{ij}^2(r_{ij,\boldsymbol{L}})^2 + 8(r_{ij,\boldsymbol{L}})^4\right)\exp\left[-\left(\frac{r_{ij,\boldsymbol{L}}}{\sigma_{ij}}\right)^2\right]\Bigg].\end{aligned} \tag{A-9}$$

The derivative of the damping function f in Eq. A-6 is constructed using the chain rule as

$$\begin{aligned}\frac{\partial f(S_{\mathrm{vdW},ij}, r_{ij,\boldsymbol{L}})}{\partial r_i^a} &= \frac{\partial f(S_{\mathrm{vdW},ij}, r_{ij,\boldsymbol{L}})}{\partial r_{ij,\boldsymbol{L}}}\frac{\partial r_{ij,\boldsymbol{L}}}{\partial r_i^a} \\ &= -\frac{d}{S_{\mathrm{vdW},ij}}\frac{r_{ij,\boldsymbol{L}}^a}{r_{ij,\boldsymbol{L}}} f^2(S_{\mathrm{vdW},ij}, r_{ij,\boldsymbol{L}})\exp[-d(r_{ij,\boldsymbol{L}}/S_{\mathrm{vdW},ij} - 1)].\end{aligned} \tag{A-10}$$

A.2 $\nabla \mathbf{T}_{LR}(\boldsymbol{k})$

Next, as described in Ref. [60], the derivatives of $\mathbf{T}_{LR}(\boldsymbol{k})$ with regard to r_α^a is defined as follows:

$$\begin{aligned}\frac{\partial T_{LR,ij}^{bc}(\boldsymbol{k})}{\partial r_\alpha^a} =&(\delta_{\alpha i}-\delta_{\alpha j})\sum_{\boldsymbol{L}}{}'\left\{\frac{\partial T_{ij,\boldsymbol{L}}^{bc}}{\partial r_{ij,\boldsymbol{L}}^a} f(\tilde{S}_{\mathrm{vdW},ij}, r_{ij,\boldsymbol{L}})\right.\\ &\left.+ T_{ij,\boldsymbol{L}}^{bc}\frac{\partial f(\tilde{S}_{\mathrm{vdW},ij}, r_{ij,\boldsymbol{L}})}{\partial r_\alpha^a}\right\}\mathrm{e}^{-2\pi \mathrm{i}\boldsymbol{k}\cdot\boldsymbol{L}}.\end{aligned} \tag{A-11}$$

where

$$\frac{\partial T_{ij,\boldsymbol{L}}^{bc}}{\partial r_{ij,\boldsymbol{L}}^a} = -\frac{15 r_{ij,\boldsymbol{L}}^a r_{ij,\boldsymbol{L}}^b r_{ij,\boldsymbol{L}}^c - 3r_{ij}^2(r_{ij}^a\delta_{bc}+r_{ij}^b\delta_{ca}+r_{ij}^c\delta_{ab})}{r_{ij,\boldsymbol{L}}^7}. \tag{A-12}$$

Since $\tilde{S}_{\mathrm{vdW}}$ depends on atomic positions unlike S_{vdW} in Eq. A-10, $\frac{\partial f(\tilde{S}_{\mathrm{vdW},ij}, r_{ij,\boldsymbol{L}})}{\partial r_\alpha^a}$ can be computed as follows:

$$\frac{\partial f(\tilde{S}_{\mathrm{vdW},ij}, r_{ij,\boldsymbol{L}})}{\partial r_\alpha^a} = \frac{\partial f(\tilde{S}_{\mathrm{vdW},ij}, r_{ij,\boldsymbol{L}})}{\partial r_{ij,\boldsymbol{L}}}\frac{\partial r_{ij,\boldsymbol{L}}}{\partial r_\alpha^a} + \frac{\partial f(\tilde{S}_{\mathrm{vdW},ij}, r_{ij,\boldsymbol{L}})}{\partial \tilde{S}_{\mathrm{vdW},ij}}\frac{\tilde{S}_{\mathrm{vdW},ij}}{\partial r_\alpha^a}. \tag{A-13}$$

The expression on the first right-hand side in Eq. A-13 is similar to Eq. A-10:

$$\begin{aligned}\frac{\partial f(\tilde{S}_{\mathrm{vdW},ij}, r_{ij,\boldsymbol{L}})}{\partial r_{ij,\boldsymbol{L}}}\frac{\partial r_{ij,\boldsymbol{L}}}{\partial r_\alpha^a} =&(\delta_{\alpha j}-\delta_{i\alpha})\frac{d}{\tilde{S}_{\mathrm{vdW},ij}}\frac{r_{ij,\boldsymbol{L}}^a}{r_{ij,\boldsymbol{L}}}\\ &\times f^2(\tilde{S}_{\mathrm{vdW},ij}, r_{ij,\boldsymbol{L}})\exp[-d(r_{ij,\boldsymbol{L}}/\tilde{S}_{\mathrm{vdW},ij}-1)].\end{aligned} \tag{A-14}$$

On the one hand, the second term is given by

$$\begin{aligned}\frac{\partial f(\tilde{S}_{\mathrm{vdW},ij}, r_{ij,\boldsymbol{L}})}{\partial \tilde{S}_{\mathrm{vdW},ij}}\frac{\tilde{S}_{\mathrm{vdW},ij}}{\partial r_\alpha^a} =& -\frac{d\, r_{ij,\boldsymbol{L}}}{(\tilde{S}_{\mathrm{vdW},ij})^2} f^2(\tilde{S}_{\mathrm{vdW},ij}, r_{ij,\boldsymbol{L}})\\ &\times \exp[-d(r_{ij,\boldsymbol{L}}/\tilde{S}_{\mathrm{vdW},ij}-1)]\frac{\tilde{S}_{\mathrm{vdW},ij}}{\partial r_\alpha^a},\end{aligned} \tag{A-15}$$

where

$$\begin{aligned}\frac{\tilde{S}_{\mathrm{vdW},ij}}{\partial r_\alpha^a} &= \beta\left(\frac{\tilde{S}_{\mathrm{vdW},i}}{\partial r_\alpha^a}+\frac{\tilde{S}_{\mathrm{vdW},j}}{\partial r_\alpha^a}\right)\\ &= \beta\left(\frac{\tilde{S}_{\mathrm{vdW},i}}{\tilde{\alpha}_i^{\mathrm{SCS,iso}}}\frac{\partial\tilde{\alpha}_i^{\mathrm{SCS,iso}}}{\partial r_\alpha^a}+\frac{\tilde{S}_{\mathrm{vdW},j}}{\tilde{\alpha}_j^{\mathrm{SCS,iso}}}\frac{\tilde{\alpha}_j^{\mathrm{SCS,iso}}}{\partial r_\alpha^a}\right).\end{aligned} \tag{A-16}$$

In Eq. A-16, $\frac{\partial\tilde{\alpha}_i^{\mathrm{SCS,iso}}}{\partial r_\alpha^a}$ explicitly matches Eq. A-4.

B. Self-consistent field convergence of PEG(thiol)@Au(111)

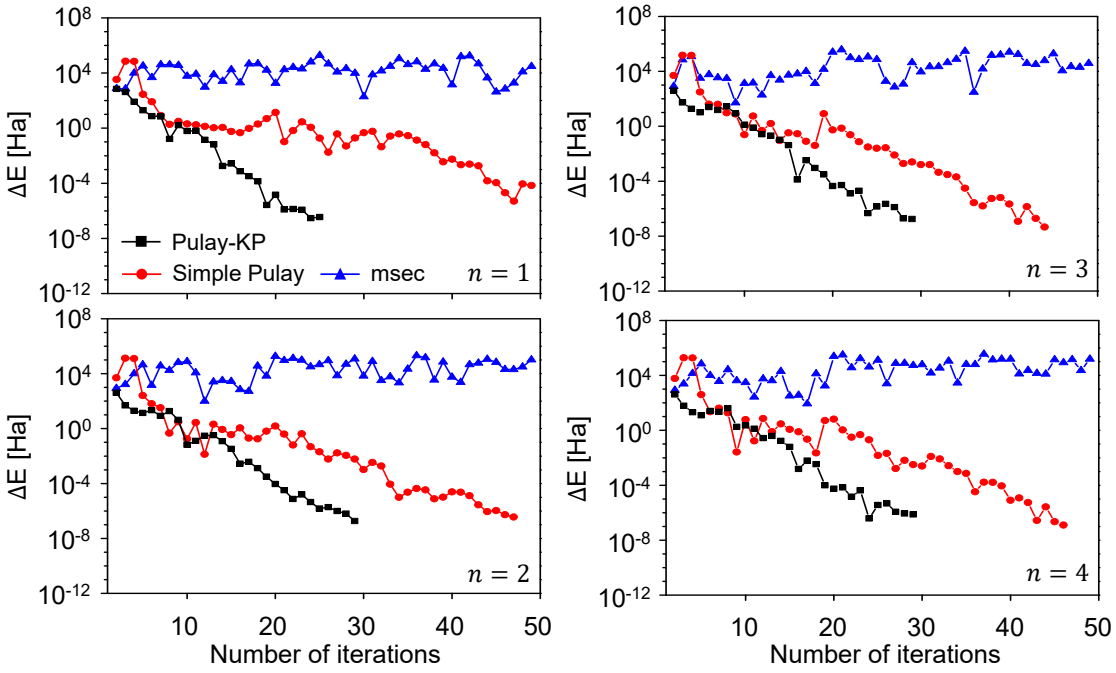

Figure **B-1**: Convergence of total energy for PEG(thiol)@Au(111) with respect to different numbers of repeat units in the molecule chain, n.

We compare the total energy convergence using potential mixing for three mixing methods: `Pulay-KP`, `simple Pulay`, and `msec`. We find that the `Pulay-KP` and `simple Pulay` methods reach a desired threshold within 50 iterations, while the `msec` method does not converge. Overrall, the `Pulay-KP` method performs faster than `simple Pulay`, converging in 30 steps for all n cases.

List of Figures

List of Tables

Publications

1. *Robust mixing in self-consistent linearized augmented planewave calculations*
   J. Kim, A. Gulans, and C. Draxl
   Electron. Struct. **2**, 037001 (2020).

2. *Work-function modification of PEG(thiol) adsorbed on the Au(111) surface: A first-principles study*
   J. Kim, A. Gulans, and C. Draxl
   Phys. Rev. Mater. **4**, 116001 (2020).

Bibliography

[1] I. D. Parker, Appl. Phys. **75**, 1656 (1994).

[2] H. Ishii, K. Sugiyama, E. Ito, and K. Seki, Adv. Mater. **11**, 605 (1999).

[3] X. Cheng, Y.-Y. Noh, J. Wang, M. Tello, J. Frisch, R.-P. Blum, A. Vollmer, J. P. Rabe, N. Koch, and H. Sirringhaus, Adv. Funct. Mater. **19**, 2407 (2009).

[4] C. Liu, Y. Xu, and Y.-Y. Noh, Materials Today **18**, 79 (2015).

[5] J. Kim, Y. S. Rim, Y. Liu, A. C. Serino, J. C. Thomas, H. Chen, Y. Yang, and P. S. Weiss, Nano Lett. **14**, 2946 (2014).

[6] S. Choi, C. Fuentes-Hernandez, C.-Y. Wang, T. M. Khan, F. A. Larrain, Y. Zhang, S. Barlow, S. R. Marder, and B. Kippelen, ACS Appl. Mater. Interfaces 8, 24744 (2016).

[7] K. Walzer, B. Maennig, M. Pfeiffer, and K. Leo, Chem. Rev. **107**, 1233 (2007).

[8] S. Chuang, C. Battaglia, A. Azcatl, S. McDonnell, J. S. Kang, X. Yin, M. Tosun, R. Kapadia, H. Fang, R. M. Wallace, and A. Javey, Nano Lett. **14**, 1337 (2014).

[9] G. Heimel, L. Romaner, E. Zojer, and J.-L. Bredas, Acc. Chem. Res. **41**, 721 (2008).

[10] C. J. Bloom, C. M. Elliott, P. G. Schroeder, C. B. France, and B. A. Parkinson, J. Phys. Chem. B **107**, 2933 (2003).

[11] D. L. Matz, E. L. Ratcliff, J. Meyer, A. Kahn, and J. E. Pemberton, ACS Appl. Mater. Interfaces **5**, 6001 (2013).

[12] Y. Zhou, C. Fuentes-Hernandez1, J. Shim, J. Meyer, A. J. Giordano, H. Li, P. Winget, T. Papadopoulos, H. Cheun, J. Kim, M. Fenoll, A. Dindar, W. Haske, E. Najafabadi, T. M. Khan, H. Sojoudi, S. Barlow, S. Graham, J.-L. Bréas, S. R. Marder, A. Kahn, B. Kippelen, Science **336**, 327 (2012).

[13] M. Jørgensen, K. Norrman, F. C. Krebs, Sol. Energy Mater. Sol. Cells **92**, 686 (2008).

[14] S. Braun, W. R. Salaneck, and M. Fahlman, Adv. Mater.**21**, 1450 (2009).

[15] T. M. Khan, Y. Zhou, A. Dindar, J. W. Shim, C. Fuentes-Hernandez, and B. Kippelen, ACS Appl. Mater. Interfaces **6**, 6202 (2014).

[16] E. L. Ratcliff, B. Zacher, and N. R. Armstrong, J. Phys. Chem. Lett. **2**, 1337 (2011).

[17] N. Koch, ChemPhysChem **8**, 1438 (2007).

[18] M. Kano, T. Minari, and K. Tsukagoshi, Appl. Phys. Lett. **94**, 143304 (2009).

[19] M.-H. Chen and C.-I Wu, J. Appl. Phys. **104**, 113713 (2008).

[20] B. deBoer, A. Hadipour, M. M. Mandoc, T. van Woudenbergh, P. W. M. Blom, Adv. Mater. **17**, 621 (2005).

[21] I. Deckman, S. Obuchovsky, M. Moshonov, and G. L. Frey, Langmuir **31**, 6721 (2015).

[22] B. Shamieh, S. Obuchovsky, and G. L. Frey, J. Mater. Chem. C **4**, 1821 (2016).

[23] J. Vinokur, S. Obuchovsky, l. Deckman, L. Shoham, T. Mates, M. L. Chabinyc, G. L. Frey, Appl. Mater. Interfaces **9**, 29889 (2017).

[24] L. Nouzman and G. L. Frey, J. Mater. Chem. C **5**, 12744 (2017).

[25] T. Sarkar, J. Vinokur, B. Shamieh, V. Savikhin, M. F. Toney, and G. L. Frey, Chem. Mater. **31**, 7046 (2019).

[26] T. Sarkar, B. Shamieh, R. Verbeek, A. J. Kronemeijer, G. H. Gelinck, and G. L. Frey, Adv. Funct. Mater. **30**, 1805617 (2020).

[27] B. Shamieh, A. S. Anselmo, U. Vogel, E. Lariou, S. C. Hayes, N. Koch, and G. L. Frey, J. Mater. Chem. C **6**, 8060 (2018).

[28] G. Heimel, F. Rissner, and E. Zojer, Adv. Mater. **22**, 2494 (2010).

[29] J. C. Love, L. A. Estroff, J. K. Kriebel, R. G. Nuzzo, and G. M. Whitesides, Chem. Rev. **105**, 1103 (2005).

[30] F. Tao and S. L. Bernasek, Chem. Rev. **107**, 1408 (2007).

[31] H. J. Lee, A. C. Jamison, and T. R. Lee, Acc. Chem. Res. **48**, 3007 (2015).

[32] J.-P. Hong, A.-Y. Park, S. Lee, J. Kang, N. Shin, and D. Y. Yoo, Appl. Phys. Lett. **92**, 143311 (2008).

[33] D. M. Alloway, A. L. Graham, X. Yang, A. Mudalige, R. Colorado, Jr., V. H. Wysocki, J. E. Pemberton, T. R. Lee, R. J. Wysocki, and N. R. Armstrong, J. Phys. Chem. C **113**, 20328 (2009).

[34] A. Gulans, S. Kontur, C. Meisenbichler, D. Nabok, P. Pavone, S. Rigamonti, S. Sagmeister, U. Werner, C. Draxl, J. Phys.: Condens. Matter. **26**, 363202 (2014).

[35] N. D. Woods, M. C. Payne, and P. J. Hasnip, J. Phys.: Condens. Matter. **31**, 453001 (2019).

[36] P. -M. Anglade and X. Gonze, Phys. Rev. B **78**, 045126 (2008).

[37] G. P. Kerker, Phys. Rev. B **23**, 3082 (1981).

[38] G. Kresse and J. Furthmüller, Comput. Mater. Sci. **6**, 15 (1996).

[39] G. Kresse and J. Furthmüller, Phys. Rev. B **54**, 11169 (1996).

[40] M. Kohyama, Modelling Simul. Mater. Sci. Eng. **4**, 397 (1996).

[41] Y. Shiihara, O. Kuwazuru, and N. Yoshikawa, Modelling Simul. Mater. Sci. Eng. **16**, 035004 (2008).

[42] R. Sundararaman, W. A. Goddard III, and T. A. Arias, J. Chem. Phys. **146**, 114104 (2017).

[43] E. Londero and E. Schröder, Phys. Rev. B **82**, 054116 (2010).

[44] E. Londero and E. Schröder, Comput. Phys. Commun. **182**, 1805 (2011).

[45] P. Pulay, Chem. Phys. Lett. **73**, 393 (1980).

[46] P. Pulay, J. Comput. Chem. **3**, 556 (1982).

[47] E. R. Johnson, I. D. Mackie, and G. A. Dilabio, J. Phys. Org. Chem. **22**, 1127 (2009).

[48] P. Sony, P. Puschnig, D. Nabok, and C. Ambrosch-Draxl, Phys. Rev. Lett. **99**, 176401 (2007).

[49] A. Tkatchenko, L. Romaner, O. T. Hofmann, E. Zojer, C. Ambrosch-Draxl, and M. Scheffler, MRS Bulletin **35**, 435 (2010).

[50] E. McNellis, J. Meyer, and K. Reuter, Phys. Rev. B **80**, 205414 (2009).

[51] S. Grimme, WIREs Rev. Comput. Mol. Sci. **1**, 211 (2011).

[52] J. Klimeš and A. Michaelides, J. Chem. Phys. **137**, 120901 (2012).

[53] S. Kristyan, P. Pulay, Chem. Phys. Lett. **229**, 175 (1994).

[54] S. Grimme, J. Comput. Chem. **25**, 1463 (2004).

[55] S. Grimme, J. Comput. Chem. **27**, 1787 (2006).

[56] S. Grimee, J. Antony, S. Ehrlich, and H. Krieg, J. Chem. Phys. **132**, 154104 (2010).

[57] A. Tkatchenko and M. Scheffler, Phys. Rev. Lett. **102**, 073005 (2009).

[58] M. Dion, H. Rydberg, E. Schröder, D. C. Langreth, and B. I. Lundqvist, Phys. Rev. Lett. **92**, 246401 (2004).

[59] A. Ambrosetti, A. M. Reilly, R. A. DiStasio Jr., and A. Tkatchenko, J. Chem. Phys. **140**, 18A508 (2014).

[60] T. Bučko, S. Lebègue, T. Gould, and J. G. Ángyán, J. Phys.: Condens. Matter. **28**, 045201 (2016).

[61] A. Tkatchenko, R. A. DiStasio, Jr., R. Car, and M. Scheffler, Phys. Rev. Lett. **108**, 236402 (2012).

[62] A. D. Becke and E. R. Johnson, J. Chem. Phys. **122**, 154104 (2005).

[63] A. D. Becke and E. R. Johnson, J. Chem. Phys. **123**, 154101 (2005).

[64] B. Geffroy, P. L. Roy, and C. Prat, Polymer International **55**, 572 (2006).

[65] C. W. Tang, S. A. VanSlyke and C. H. Chen, J. Appl. Phys. **65**, 3610 (1989).

[66] J. Shi and C. W. Tang, Appl. Phys. Lett. **70**, 1665 (1997).

[67] M. B. Khalifa, D. Vaufey, and J. Tardy, Org. Elec. **5**, 187 (2004).

[68] J. S. Huang, G. Li, E. Wu, Q. F. Xu, and Y. Yang, Adv. Mater. **18**, 114 (2006).

[69] X. Qiao, Y. Tao, Q. Wang, D. Ma, C. Yang, L. Wang, J. Qin, and Fosong Wang, J. Appl. Phys. **108**, 034508 (2010).

[70] C. W. Tang and S. A. Vanslyke, Appl. Phys. Lett. **51**, 913 (1987).

[71] Y. Shirota, Y. Kuwabara, H. Inada, T. Wakimoto, H. Nakada, Y. Yonemoto, S. Kawami and K. Imai, Appl. Phys. Lett. **65**, 807 (1994).

[72] S. Y. Kim, J.-L. Lee, K.-B. Kim, and Y.-H Tak, J. Appl. Phys. **95**, 2560 (2004).

[73] F. Nuesch, E. W. Forsythe, Q. T. Le, Y. Gao, and L. J. Rothberg, J. Appl. Phys. **87**, 7973 (2000).

[74] L. S. Hung, C. W. Tang, and M. G. Mason, Appl. Phys. Lett. **70**, 152 (1997).

[75] J. Lee, Y. Park, S. K. Lee, E. J. Cho, D. Y. Kim, H. Y. Chu, H. Lee, L. M. Do, and T. Zyung, Appl. Phys. Lett. **80**, 3123 (2002).

[76] J. Lee, Y. Park, D. Y. Kim, H. Y. Chu, H. Lee, and L. M. Do, Appl. Phys. Lett. **82**, 173 (2003).

[77] Y. Park, J. Lee, S. K. Lee, and D. Y. Kim, Appl. Phys. Lett. **79**, 105 (2001).

[78] J. C. Scott, J. Vac. Sci. Technol. A **21**, 521 (2003).

[79] C. R. Crowell and S. M. Sze, Solid-State Electronics **9**, 1035 (1966).

[80] A. Kahn, N. Koch, and W. Gao, J. Polym. Sci. B Polym. Phys. **41**, 2529 (2003).

[81] E. Itoh, M. Iwamoto, M. Burghard, and S. Roth, Jpn. J. Appl. Phys. **39**, 5146 (2000).

[82] H. Ishii and K. Seki, IEEE Trans. Electron Devices 44, 1295 (1997).

[83] N. D. Lang, W. Kohn, Phys. Rev. B **3**, 1215 (1971).

[84] N. D. Lang, W. Kohn, Phys. Rev. B **1**, 4555 (1970).

[85] N. D. Lang, Phys. Rev. Lett. **46**, 842 (1981).

[86] G. Witte, S. Lukas, P. S. Bagus, and C. Wöll, Appl. Phys. Lett. **87**, 263502 (2005).

[87] P. S. Bagus, V. Staemmler, and C. Wöll, Phys. Rev. Lett. **89**, 096104 (2002).

[88] M. Oehzelt, N. Koch, and G. Heimel, Nat. Commun. **5**, 4174 (2014).

[89] X. Crispin, V. M. Geskin, A. Crispin, J. Cornil, R. Lazzaroni, W. R. Salaneck, and J.-L. Brédas, J. Am. Chem. Soc. **124**, 8131 (2002).

[90] R. G. Parr and R. G. Pearson, J. Am. Chem. Soc. **105**, 7512 (1983).

[91] G. Heimel, L. Romaner, E. Zojer, and J.-L. Brédas, Nano lett. **7**, 932 (2007).

[92] H. Li, P. Paramonov, and J. L. Bredas, J. Mater. Chem. **20**, 2630 (2010).

[93] H. Li, P. Winget, and Jean-Luc Brédas, Chem. Mater. **26**, 631 (2014).

[94] Q. Wang, V. Diez-Cabanes, S. Dell'Elce, A. Liscio, B. Kobin, H. Li, J. Brédas, S. Hecht, V. Palermo, E. J. W. List-Kratochvil, J. Cornil, N. Koch, and G. Ligorio, ACS Appl. Nano Mater. **2**, 1102 (2019).

[95] L. H. Thomas, Proc. Camb. Phil. Soc. **23**, 542 (1926).

[96] E. Fermi, Rend. Accad. Lincei. **6**, 602 (1927).

[97] P. Hohenberg and W. Kohn, Phys. Rev. **136**, B864 (1964).

[98] W. Kohn and L. J. Sham, Phys. Rev. **140**, A1133 (1965).

[99] M. Born and J. R. Oppenheimer. Ann Physik, **84**, 458 (1927).

[100] J. P. Perdew and K. Schmidt, AIP Conference Proceedings, **577**, 1 (2001). Richard M. Martin. Electronic structure: basic theory and practical methods. Cambridge university press, 2004

[101] P. A. M. Dirac, Proc. Cambridge Phil. Soc. **26**, 376 (1930).

[102] D. M. Ceperley and B. J. Alder, Phys. Rev. Lett. **45**, 566 (1980).

[103] S. H. Vosko, L. Wilk and M. Nusair, Can. J. Phys. **58**, 1200 (1980).

[104] J. P. Perdew and A. Zunger, Phys. Rev. B **23**, 5048 (1981).

[105] J. P. Perdew and Y. Wang, Phys. Rev. B **45**, 13244 (1992).

[106] R. O. Jones and O. Gunnarsson, Rev. Mod. Phys. **61**, 689 (1989).

[107] P. P. Rushton, D. J. Tozer, and S. J. Clark, Phys. Rev. B **65**, 235203 (2002).

[108] D. C. Langreth and M. J. Mehl, Phys. Rev. B **28**, 1809 (1983).

[109] J. P. Perdew, J. A. Chevary, S. H. Vosko, K. A. Jackson, M. R. Pederson, and C. Fiolhais, Phys. Rev. B **46**, 6671 (1992).

[110] A. D. Becke, Phys. Rev. A **38**, 3098 (1988).

[111] C. Lee, W. Yang, and R. G. Parr, Phys. Rev. B **374**, 785 (1988).

[112] J. P. Perdew, *Electronic Structure of Solids '91* (Akademie Verlag, Berlin, 1991).

[113] J. P. Perdew, K. Burke, and M. Ernzerhof, Phys. Rev. Lett. **77**, 3865 (1996).

[114] P. Perdew, R. G. Parr, M. Levy, and J. L. Balduz, Phys. Rev. Lett. **49**, 1691 (1982).

[115] S. Kümmel and L. Kronik, Rev. Mod. Phys. **80**, 3 (2008).

[116] F. Hirshfeld, Theor. Chim. Acta **44**, 129 (1977).

[117] A. J. Stone, The Theory of Intermolecular Forces, Oxford University, Oxford (1997).

[118] X. Chu and A. Dalgarno, J. Chem. Phys. **121**, 4083 (2004).

[119] A. Bondi, J. Phys. Chem. **68**, 441 (1964).

[120] T. W. Whitfield and G. J. Martyna, Chem. Phys. Lett. **424**, 409 (2006).

[121] C. G. Broyden, Math. Comput. **19**, 577 (1965).

[122] D. D. Johnson, Phys. Rev. B **38**, 12807 (1988).

[123] X. Gonze, Phys. Rev. B **54**, 4383 (1996).

[124] L. D. Marks and D. R. Luke, Phys. Rev. B **78**, 075114 (2008).

[125] D. R. Bowler and M. J. Gillan, Chem. Phys. Lett. **325**, 473 (2000).

[126] H. R. Fang and Y. Saad, Linear Algebra Appl. **16**, 197 (2009).

[127] P. P. Pratapa and P. Suryanarayana, Chem. Phys. Lett. **635**, 69 (2015).

[128] A. S. Banerjee, P. Suryanarayana, and J. E. Pask, Chem. Phys. Lett. **647**, 31 (2016).

[129] J. F. Annett, Comput. Mater. Sci. **4**, 23 (1995).

[130] L. D. Marks, J. Chem. Theory Comput. **9**, 2786 (2013).

[131] P. C. Hansen, *Rank-Deficient and Discrete Ill-Posed Problems* (SIAM, Philadelphia, 1998).

[132] P. Blaha, K. Schwarz, P. Sorantin, and S.B. Trickey, Comp. Phys. Commun. **59**, 399 (1990).

[133] Ph. Ghosez, X.Gonze, R. W. Godby, Phys. Rev. B **56**, 12811 (1997).

[134] D. Raczkowski, A. Canning, and L. W. Wang, Phys. Rev. B **44**, 121101(R) (2001).

[135] D. Vanderbilt and S. G. Louie, Phys. Rev. B **30**, 6118 (1984).

[136] K. M. Ho, J. Ihm, and J. D. Joannopoulos, Phys. Rev. B **25**, 4260 (1982).

[137] J. C. Slater, Phys. Rev. **51**, 846 (1937).

[138] O. K. Andersen, Phys. Rev. B **12**, 3060 (1975).

[139] E. Sjöstedt, L. Nordström, and D. J. Singh, Solid State Commun. **114**, 15 (2000).

[140] D. Singh, Phys. Rev. B **43**, 6388 (1991).

[141] D.R. Hamann, Phys. Rev. Lett. **42**, 662 (1979).

[142] E. Wimmer, H. Krakauer, M. Weinert, and A.J. Freeman, Phys. Rev. B **24**, 864 (1981).

[143] M. Weinert, J. Math. Phys. **22**, 2433 (1981).

[144] J. D. Jackson, Classical Electrodynamics, 3rd ed., Wiley, New York, 1999.

[145] F. Tran, P. Blaha, Phys. Rev. B **83**, 235118 (2011).

[146] D. J. Singh and L. Nordström, Planewaves, Pseudopotentials and the LAPW Method, 2nd ed., Springer, Berlin (2006).

[147] P. Bendt and A. Zunger, Phys. Rev. B **26**, 3114 (1982).

[148] Y. Zhou, H. Wang, Y. Liu, X. Gao, H. Song, Phys. Rev. E **97**, 033305 (2018).

[149] S. Mohr, M. Eixarch, M. Amsler, M. J. Mantsinen, and L. Genovese, Nucl. Mater. Energy **15**, 64 (2018).

[150] M. A. Blood-Forsythe, T. Markovich, R. A. DiStasio, Jr., R. Car, A. Aspuru-Guzik, Chem. Sci. **7**, 1712 (2016).

[151] D. C. Langreth and J. P. Perdew, Phys. Rev. B **15**, 2884 (1977).

[152] X. Ren, P. Rinke, V. Blum, J. Wieferink, A. Tkatchenko, A. Sanfilippo, K. Reuter, and M. Scheffler, New. J. Phys. **14**, 053020 (2012).

[153] Y. X. Zhao and and I. L. Spain, Phys. Rev. B **40**, 993 (1989).

[154] S. Pease, Acta Crystallogr. **5**, 356 (1952).

[155] P. Lazar, E. Otyepková, F. Karlický, K. Čépe, M. Otyepka, Carbon **94**, 804 (2015).

[156] S. Lubeck, Long-Range Dispersion Corrections to Density-Functional-Theory Calculations: Implementation and Applications, thesis, Humboldt-Universität zu Berlin, 2015.

[157] T. Bučko, J. Hafner, S. Lebègue, and J. G. Ángyán, J. Phys. Chem. A, **114**, 11814 (2010).

[158] Hanke. F, J. Comp. Chem. **32**, 1424 (2011).

[159] T. Bučko, S. Lebègue, and J. Hafner, Phys. Rev. B **87**, 064110 (2013).

[160] R. Zacharia, H. Ulbricht, and T. Hertel, Phys. Rev. B **69**, 155406 (2004).

[161] V. L. Solozhenko, G. Will, and F. Elf, Solid State Commun. **96**, 1 (1995)

[162] A. Marini, P. García-González, and A. Rubio, Phys. Rev. Lett. **96**, 136404 (2006).

[163] T. Björkman, A. Gulans, A. V. Krasheninnikov, and R. M. Nieminen, Phys. Rev. Lett. **108**, 235502 (2012).

[164] W. Rüdorff, Adv. Inorg. Chem. Radiochem. **1**, 223 (1959).

[165] H. Fujimoto, Carbon **35**, 1061 (1997).

[166] T. Gould, S. Lebègue, J. G. Ángýan, and T. Bučko, J. Chem. Theory Comput. **12**, 5920 (2016).

[167] K. Knop, R. Hoogenboom, D. Fischer, U. S. Schubert, Angew. Chem. Int. Ed. **49**, 6288 (2010).

[168] G. Liu, Y. Li, L. Yang, Y. Wei, X. Wang, Z. Wang, and L. Tao, RSC Adv. **7**, 18252 (2017).

[169] C. C. Luo, Y. H. Zhang, X. W. Zeng, Y. W. Zeng, and Y. G. Wang, J. Colloid Interface Sci. **288**, 444 (2005).

[170] S. Dhar , F. X. Gu , R. Langer , O. C. Farokhzad and S. J. Lippard , Proc. Natl. Acad. Sci. U. S. A. **105** , 17356 (2008).

[171] J. Manson, D. Kumar, B. J. Meenan and D. Dixon, Gold Bull. **44**, 99 (2011).

[172] J. Vinokur, I. Deckman, T. Sarkar, L. Nuzman, B. Shamieh, and G. L. Frey, Adv. Mater. **30**, 1706803 (2018).

[173] C. J. van Oss, M. K. Chaudhury, and R. J. Good, Adv. Colloid Interface Sci. **28**, 35 (1987).

[174] S. Cataldo, C. Sartorio, F. Giannazzo, A. Scandurra, and B. Pignataro, Nanoscale **6**, 3566 (2014).

[175] D. M. DeLongchamp, R. J. Kline, and A. Herzing, Energy Environ. Sci. **5**, 5980 (2012).

[176] G. Krausch, Mater. Sci. Eng., R **14**, 1 (1995).

[177] C. Vericat, G. Andreasen, M. E. Vela, H. Martin, and R. C. Salvarezza, J. Chem. Phys. **115**, 6672 (2001).

[178] C. Vericat, M. E. Vela, and R. C. Salvarezza, Phys. Chem. Chem. Phys. **7**, 3258 (2005).

[179] W. Azzam, C. Fuxen, A. Birkner, H.-T. Rong, M. Buck, and C. Wöll, Langmuir **19**, 4958 (2003).

[180] J. Nara, S. Higai, Y. Morikawa, and T. Ohno, J. Chem. Phys. **120**, 6705 (2004).

[181] K. Forster-Tonigold, X. Stammer, C. Wöll, and A. Groß, Phys. Rev. Lett. **111**, 086102 (2013).

[182] K. Forster-Tonigold and A. Groß, Surface Science **640**, 18 (2015).

[183] K. Y. Wu, S. Y. Yu, and Y. T. Tao, Lanmuir **25**, 6232 (2009).

[184] Y.T. Tao, K.Y. Wu, K. H. Huang, and T. P. Perng, Organic Electronics **12**, 602 (2011).

[185] L. Bengtsson, Phys. Rev. B **59**, 12301 (1999).

[186] S. Duhm, A. Gerlach, I. Salzmann, B. Bröker, R.L. Johnson, F. Schreiber, and N. Koch, Org. Electron. **9**, 111 (2008).

[187] N. E. Singh-Miller and N. Marzari, Phys. Rev. B **80**, 235407 (2009).

[188] A. Patra, J. E. Bates, J. Sun, and J. P. Perdew, PNAS **114**, E9188 (2017).

[189] D. Cornil, T. Van Regemorter, D. Beljonne, and J. Cornil, Phys. Chem. Chem. Phys. **16**, 20887 (2014).

[190] A. Ulman, Chem. Rev. **96**, 1533 (1996).

[191] L. Romaner, D. Nabok, P. Puschnig, E. Zojer, and C. Ambrosch-Draxl, New J. Phys. **11**, 053010 (2009).

[192] D. Nabok, P. Puschnig and C. Ambrosch-Draxl, Phys. Rev. B **77**, 245316 (2008).

[193] K. Schwaha, N. D. Spencer, R. M. Lambert, Surf. Sci. **81**, 273. (1979).

[194] P. E. Laibinis, G. M. Whitesides, D. L. Allara, Y. T. Tao, A. N. Parikh, and R. G. Nuzzo, J. Am. Chem. Soc. **113**, 7152 (1991).

[195] P. Fenter, P. Eisenberger, J. Li, N. Camillone, S. Bernasek, G. Scoles, T. A. Ramanarayanan, and K. S. Liang, Langmuir **7**, 2013 (1991).

[196] H. Sellers, A. Ulman, Y. Shnidman, and J. E. Eilers, J. Am. Chem. Soc. **115**, 9389 (1993).

[197] M. Yu, S. Driver, and D. P. Woodruff, Langmuir **21**, 7285 (2005).

[198] M. Yu, D. P. Woodruff, N. Bovet, C. J. Satterley, K. Lovelock, R. G. Jones, and V. R. Dhanak, J. Phys. Chem. B **110**, 2164 (2006).

[199] G. S. Parkinson, A. Hentz, P. D. Quinn, A. J. Window, D. P. Woodruff, P. Bailey, and T. C. Q. Noakes, Surf. Sci. **601**, 50 (2007).

[200] D. P. Woodruff, Phys. Chem. Chem. Phys. **10**, 7211 (2008).

[201] M. Shen, D.-J. Liu, C.J. Jenks, P.A. Thiel, J. Phys. Chem. C **112**, 4281 (2008).

[202] P. N. Abufager, L. Alvarez Soria, M. L. Martiarena, K. Reuter, and H. F. Busnengo, Chem. Phys. Lett. **503**, 71 (2011).

[203] P. N. Abufager, J. G. S. Canchaya, Y. Wang, M. Alcamí, F. Martín, L. A. Soria, M. L. Martiarena, K. Reuter, and H. F. Busnengo, Phys. Chem. Chem. Phys. **13**, 9353 (2011).

[204] M. Chelvayohan, C.H.B. Mee, J. Phys. C: Solid State Phys. **15**, 2305 (1982).

[205] J. G. Ángýan, F. Colonna-Cesari, and O. Tapia, Chem. Phys. Lett. **166**, 180 (1990).